Dimensional assessment and process optimization of additively manufactured structured 3D porosity via primitive triply periodic minimal surface lattice structure and laser powder bed fusion technique

by

Ali Mulhi

A thesis submitted in partial fulfillment of the requirements for the degree of

Master of Science

Department of Mechanical Engineering

University of Alberta

Abstract

This thesis reports the challenges that need to be addressed before any heat transfer analysis of a proposed novel cellular-walled pipe heat sink system manufactured by LPBF technique. The proper cellular structure type selection for enhanced heat transfer performance, as well as providing a detailed analysis of its dimensional trends and CAD to manufactured deviations, are investigated. Triply Periodic Minimal Surface (TPMS) lattices have been heavily investigated lately due to their superior thermo-mechanical performance compared with their lattice counterparts. The advancement of additive manufacturing, i.e., laser powder bed fusion (LPBF), has easily enabled the manufacturing of such complex lattices. Recent studies have investigated the heat transfer performance of multiple TPMS lattice types such as Gyroid, Dimond, IWP, and Primitive structures. The Primitive TPMS (PTPMS) showed enhanced heat transfer performance mainly due to its cell shape and thickness (i.e., lattice topology). Hence, it was selected for the proposed cellular-walled pipe heat sink. Micro X-ray computed tomography (μCT) and optical microscopy (OM) were utilized to conduct the lattice dimensional analysis. Increasing the PTPMS lattice cell size from 2.9 to 10 mm showed an increase in the lattice wall thickness and pore size but a decrease in the SA:Vol ratio. However, increasing the lattice porosity from 45 to 90% resulted in a decrease in the lattice wall thickness but an increase in both the SA:Vol ratio and pore size. Comparing CAD to manufactured PTPMS lattices, the resulting lattice samples showed lower wall thicknesses and higher surface area to volume (SA:Vol) ratios than designed, which is attributed to shrinkage during the building process. The printed lattice pore size and porosity values were observed to be higher than the CAD values. Moreover, the minimum PTPMS lattice wall thickness and pore size that can successfully be printed were investigated and found to be 152 μm and 317 μm, respectively.

The type of powder material used in manufacturing the cellular-walled pipe heat sink is another challenge. In the LPBF printing process, the printing parameters for any selected material need to be optimized to manufacture fully dense parts. 2507 super duplex stainless steel (2507 SDSS) is a promising material that was selected for manufacturing the proposed heat sink system. The printing parameters for 2507 SDSS, namely: laser power, scan speed, and hatch distance, were optimized. The response surface methodology was used in generating a detailed design of experiment to investigate the different pore formation types over a wide energy density range (22.22 - 428.87 J/mm3), examine the effects of each process parameter and their interactions on the resulting porosity, and identify an optimized parameter set for producing highly dense parts. Different process parameters showed different pore formation mechanisms, with lack-of-fusion, metallurgical or gas, and keyhole regimes being the most prevalent pore types identified. The lack-of-fusion pores are observed to decrease significantly with increasing the energy density at low values. However, a gradual increase in the keyhole pores was observed at higher energy densities. An optimal energy density process window from 68.24 J/mm3 to 126.67 J/mm3 is identified for manufacturing highly dense (≥99.6%) 2507 SDSS parts. Furthermore, an optimized printing parameter set at a laser power of 217.4 W, a scan speed of 1735.7 mm/s, and a hatch distance of 51.3 μm was identified, which was able to produce samples with 99.961% relative density. Using the optimized parameter set, the as-built 2507 SDSS sample had a ferrite phase fraction of 89.3% with a yield and ultimate tensile strength of 1115.4 ± 120.7 MPa and 1256.7 ± 181.9 MPa, respectively.

Preface

This thesis is an original work by Ali Mulhi. Two journal papers related to this thesis have been submitted and are listed below. As such, the paper-based thesis guideline is followed in presenting the work.

1. Ali Mulhi, Shirin Dehgahi, Prashant Waghmare, Ahmed Qureshi, "Dimensional Assessment of Uniformly Periodic Porosity Primitive TPMS Lattices Using Additive Manufacturing Laser Powder Bed Fusion Technique" The international journal of advanced manufacturing technology (accepted).
2. Ali Mulhi, Shirin Dehgahi, Prashant Waghmare, Ahmed Qureshi, "Process Parameter Optimization of 2507 Super Duplex Stainless Steel Additively Manufactured by Laser Powder Bed Fusion Technique" Additive Manufacturing (submitted).

Acknowledgments

I would like to express my profound gratitude to my supervisors, Dr. Ahmed Qureshi and Dr. Prashant Waghmare. Without their direction, counsel, and oversight, this endeavor would never have achieved such success. Thank you for your support, patience, and opportunity to work on this exciting project.

Additionally, I would like to express my sincere gratitude to my great senior Dr. Shirin Dehgahi. I genuinely value your guidance through my research and conversations that have encouraged me to approach issues from other perspectives.

Having a social network is crucial throughout graduate studies, and I want to thank my friends in office for helping to make my MSc journey one to remember.

Finally, to my parents, brothers, sisters, and wife, thank you for your unselfish love, prayers, and words of support during my journey.

Table of Contents

List of Tables

List of Figures

List of Abbreviations

AM	Additive Manufacturing
CAD	Computer-Aided Design
ALM	Additive Layer Manufacturing
SFF	Solid Freeform Fabrication
MAM	Metal Additive Manufacturing
LPBF	Laser Powder Bed Fusion
SLM	Selective Laser Melting
TPMS	Triply Periodic Minimal Surface
PTMPS	Primitive Triply Periodic Minimal Surface
SA:Vol	Surface Area to Volume Ratio
17-4 PH SS	17-4 PH stainless steel
OS	Outer Surface
μCT	Microcomputed Tomography
p	Laser Power
v	Scan Speed
h	Hatch Distance
t	Layer Thickness

E_D	Volumetric Energy Density
DSS	Duplex Stainless Steel
SDSS	Super Duplex Stainless Steel
RSM	Response Surface Method
ANOVA	Analysis of Variance
OM	Optical Microscope
DoE	Design of Experiment
CCD	Central Composite Design
RMSE	Root Mean Squared Error
MAE	Mean Absolute Error
BCC	Body Center Cubic
FCC	Face Center Cubic

Chapter 1: Introduction

1.1. Background

Additive manufacturing (AM) is an advanced manufacturing method that can simply be defined as the process of building three-dimensional (3D) objects from computer-aided design (CAD) models by joining materials in a layer upon layer approach, as opposed to traditional subtractive manufacturing technologies [1]. It is also known as 3D printing, additive layer manufacturing (ALM), and solid freeform fabrication (SFF). Metal additive manufacturing (MAM) is one type of AM techniques that has been heavily investigated in recent years, as it opens possibilities for printing 3D metallic parts. MAM can be classified into three broad categories: (i) wire feed systems, (ii) powder feed systems, and (iii) powder bed systems. In the powder bed systems, a build plate is covered with thin layers of powder, and a laser or electron beam is then utilized to fuse the powder at specific spots identified by the CAD model. Once one layer of powder is complete, the build plate chamber moves down, and another layer is added. This procedure is successively repeated until the part is fully printed. Laser powder bed fusion (LPBF), a.k.a selective laser melting (SLM), is one technique of powder bed systems in which a laser is used to melt successive metallic powders. Figure 1.1 illustrates the working principle of the LPBF process, which is composed of powder and energy delivery systems. The three components of the powder delivery system are a powder feed chamber that moves upwards and controls the powder feed rate, a rotating coater for spreading the powder layer, and a building plate champer that moves downwards and controls the powder layer thickness. The energy delivery system is composed of a laser source and scanner that allows the delivery of a focused laser spot on all points of the building plate. The energy delivery system controls the laser power, laser path scanning speed (scan speed), and the distance between adjacent scanned paths (i.e., hatch distance). Moreover, a

flow of argon shielding gas over the building plate is utilized to prevent oxidation and clear any metal vapors or spatter produced by the laser path during the burning process.

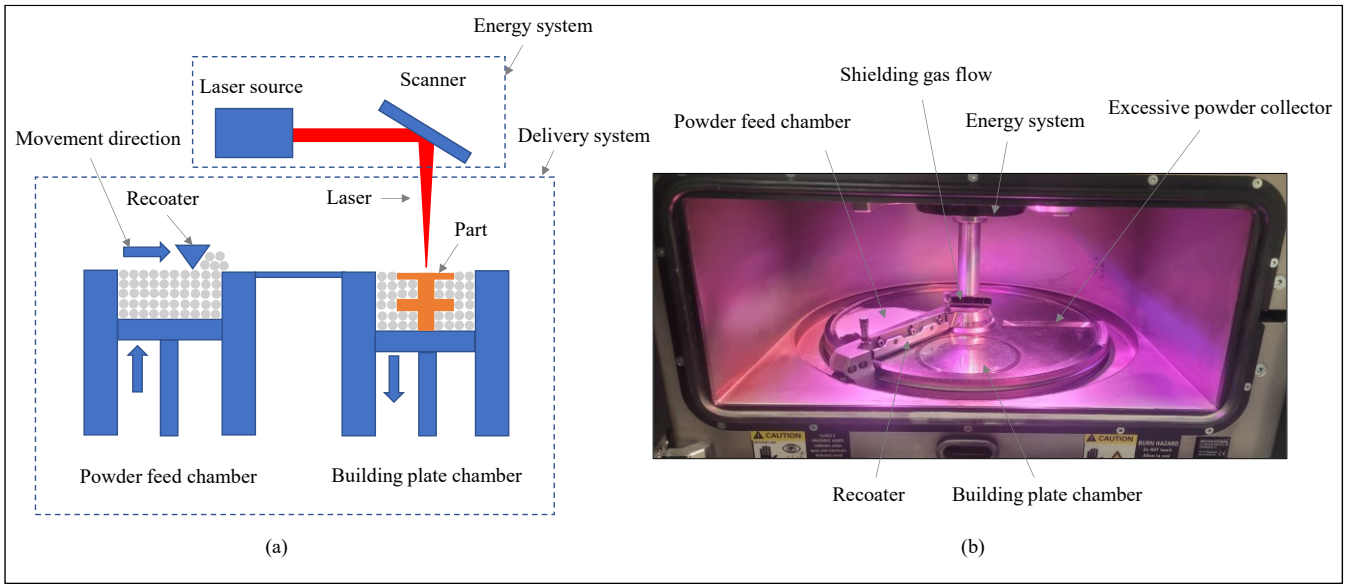

Figure 1.1: LPBF working principle: (a) schematic representation; (b) Real used system.

LPBF has shown unparalleled flexibility in manufacturing complex, lightweight, and high-value products where other traditional methods become largely impractical [2–4]. One of the potential areas that can be explored using LPBF is the manufacturing of complex cellular solids. Cellular solids are defined as structures with cells having edges and faces that are made up of interconnected strut or surface networks. Generally, cellular solids can be classified into two major categories (Figure 1.2) , namely stochastic foams and periodic lattice structures. Stochastic foams are characterized by randomly distributed cell shapes and can be found in nature such as bone and wood structures. Unlike foams, lattices are known for their periodic and well-organized cell distributions, which can be subdivided into strut based and surface based lattice structures. Strut based lattices are a series of rod-like cells connected together in different orientations; some examples are simple cubic, body-centered cubic, and face-centered cubic lattices. However, surface based lattices are composed of a series of surfaces with zero mean curvature and are

generated using mathematical equations; some examples are gyroid, primitive, and diamond lattices. A classification summary of cellular solids is illustrated in Figure 1.2.

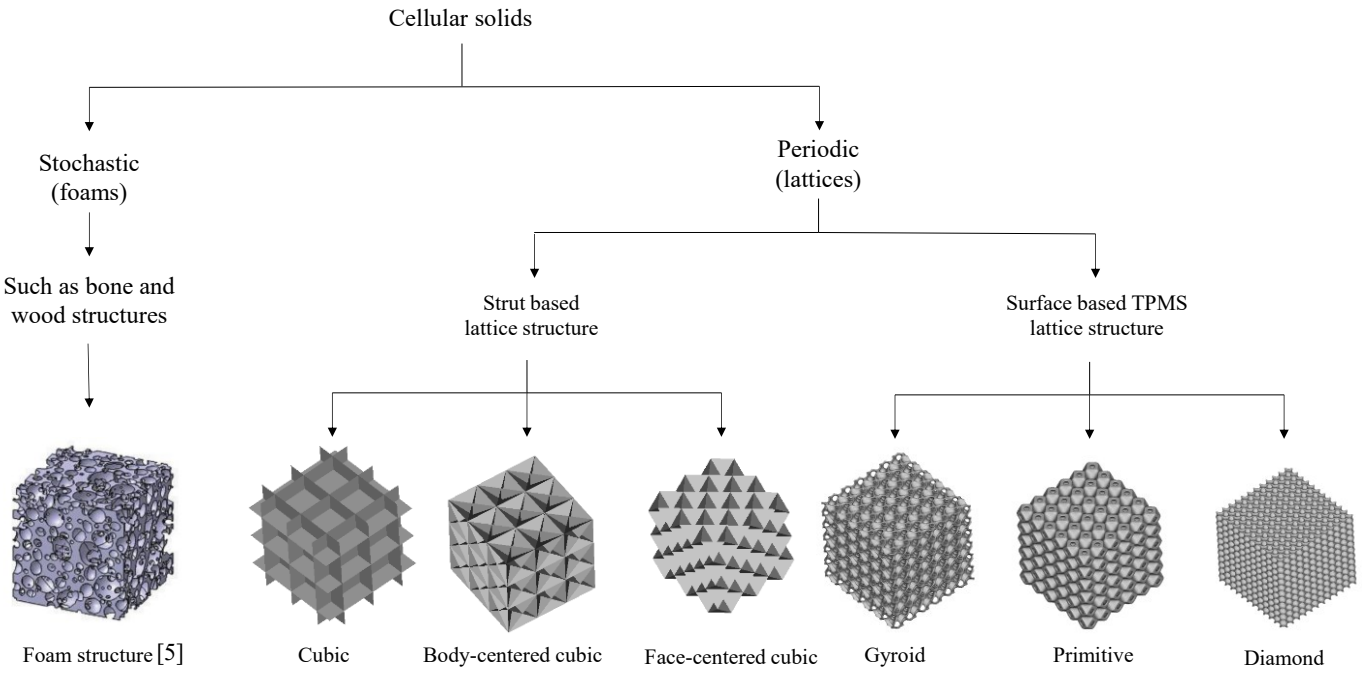

Figure 1.2: General classification of cellular solids.

1.2. Motivation

MAM is considered as one of the key new material processing technologies that will drive the metallic manufacturing sector in the future. Although LPBF, being one type of MAM, has the potential to manufacture complex parts, which opens wider manufacturing design possibilities. It is also used for the production of topologically optimized parts without the need for tooling, jigs, and fixtures leading to a considerable reduction in costs and material usage. Moreover, the remaining non-processed collected powder can be sieved and reused multiple times [6–8], leading to drastic waste reductions. Therefore, this technology is considered as a sustainable method for manufacturing complex and sustainable products, which is the focus of many industries nowadays, given the stringent environmental restrictions.

One approach to complex sustainable manufacturing using LPBF is the adoption of cellular solids. In past decades, cellular solids have gained significant interest due to their promising potential in various engineering applications [9,10]. Cellular solids are known to exhibit a combination of thermal and mechanical properties, such as high stiffness to weight ratio [10–12], enhanced energy absorption [13], and low thermal conductivity [14], which is the reason for their adoption in aerospace, impact cushions, vibration dampers, and thermal insulation applications [10].

Although cellular solids are adopted in applications where a reduced heat transfer performance is required; However, the investigated project in this thesis ultimately aims at enhancing the heat transfer performance (i.e., improve the heat dissipation) through a novel approach using cellular-walled pipes as seen in Figure 1.3. The approach utilizes the LPBF process capabilities to manufacture pipes with cellular-walled structures rather than the traditional solid walls. This will introduce a new medium where a circulating coolant fluid can be utilized to continuously absorb heat from hot fluids flowing inside the pipe. Despite the decrease in the thermal conductivity associated with cellular structures, the proposed system accounts for the increase in the surface area and utilizes that to circulate a coolant, which introduces a combination of conductive and convective heat transfer modes rather than having one conductive heat transfer mode as the case of solid pipes. This approach has the possibility to provide enhanced heat transfer performance that can be applied in various applications; As such, it is worthwhile to explore numerically and experimentally the heat transfer performance of such a system.

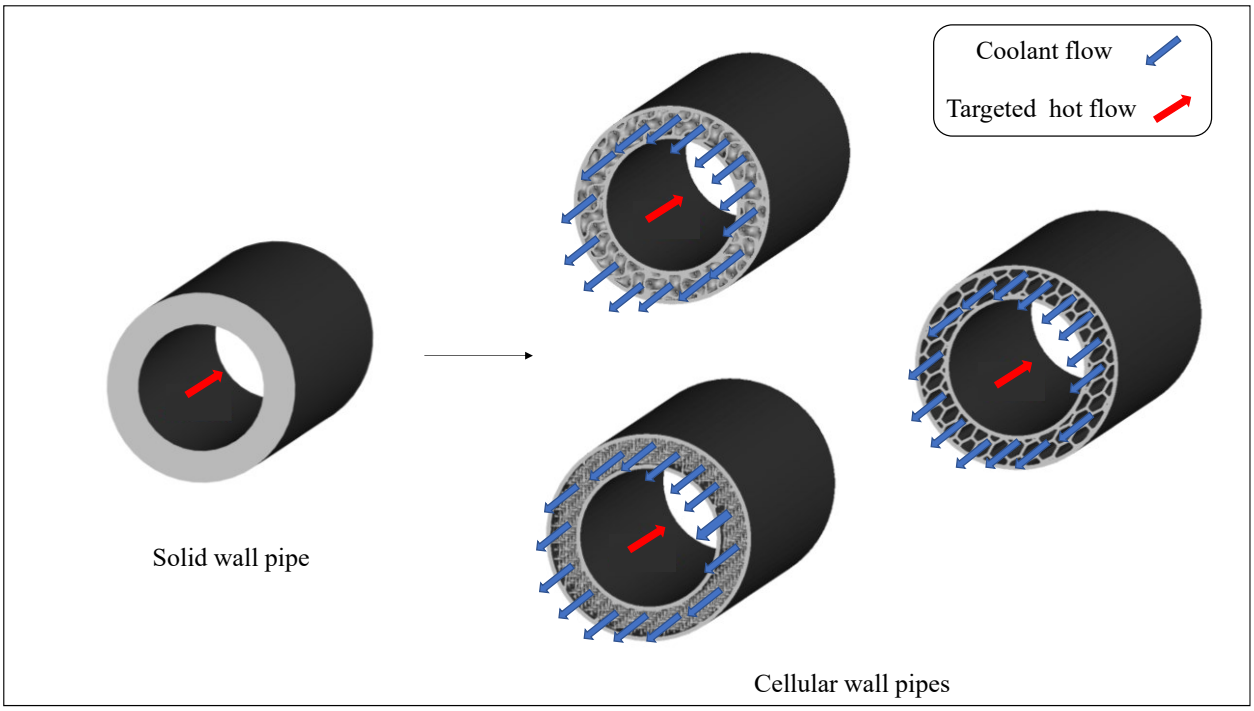

Figure 1.3: Cellular-walled pipe principle for enhanced heat transfer environment.

There are some challenges that need to be addressed before any further heat transfer analysis. One issue is the selection of the cellular structure type. Although there is a wide variety of cellular structures that can be selected for the proposed system. However, a need for a cellular structure with topologically enhanced heat transfer performance than its cellular counterparts is required. Furthermore, a deep understanding of the cellular structure dimensional trends and any CAD to manufactured dimensional deviations are essential for further heat transfer analysis, especially when both numerical modeling and experimental heat transfer analysis are conducted.

The type of powder material used in manufacturing the cellular-walled pipe heat sink is another challenge. The working principle of the proposed system indicates the presence of fluids in the heat transfer process, where critical environments such as chloride and sulfide fluids are possible encounters. Therefore, stainless steel, as a corrosion-resistant material, was selected for manufacturing such pipes. However, in the LPBF printing process, the printing parameters for any

selected material need to be optimized to manufacture fully dense parts and ensure the manufacturability of such cellular pipes. Otherwise, issues such as dimensional inaccuracy and the formation of internal non-designed pores (i.e., porosity) are usually present when poor printing parameters are selected, resulting in compromised mechanical properties or printing failures in worst scenarios. 17-4 PH and super 2507 stainless steels were selected as the manufacturing materials for the cellular pipes due to their higher strength and corrosion resistance among other steel grades. Although the optimized printing parameters for 17-4 PH stainless steel are provided by the manufacturer of our LPBF printer. However, 2507 super duplex stainless steel (SDSS) is a new powder material that has been recently processed by LPBF process, and the optimized printing parameters are not available. Hence, a need to investigate the optimized printing parameters for 2507 SDSS is required.

The heat transfer analysis of the proposed cellular-walled pipe heat sink system can not be achieved without addressing the challenges mentioned above. As such, this thesis aims at investigating a proper cellular structure type for enhanced heat transfer performance as well as providing a detailed investigation of its dimensional trends and CAD to manufactured dimensional deviations. Furthermore, a detailed optimization study of LPBF printing process parameters for 2507 SDSS material is investigated to ensure the production of highly dense parts.

1.3. Thesis Objectives

The main objective of this study is to establish preliminary knowledge essential for the heat transfer analysis of a novel cellular-walled pipe heat sink system. As such, the objectives of this research include the following tasks ($\mathbf{O_x}$):

- $\mathbf{O_1}$: Select a topologically enhanced heat transfer performance cellular structure and investigate its dimensional trends.
- $\mathbf{O_2}$: Investigate the CAD to manufactured dimensional deviations and provide insights into LPBF geometrical limitations.
- $\mathbf{O_3}$: Analyze the LPBF process parameter influence on the resulting porosity using 2507 SDSS as the powder material.
- $\mathbf{O_4}$: Optimize the LPBF printing process parameters to manufacture highly dense 2507 SDSS samples.

1.4. Methodology

The proposed methodology seen in Figure 1.4 aims at addressing the four objectives illustrated in section 1.3. The methodology approach can be divided into four main domains, namely: cell structure, printer dimensional constraints, material, and printing process. The first objective is realized by reviewing previous cellular structure studies to investigate a suitable cellular structure with a topologically enhanced heat transfer performance. Moreover, the selected cellular structure dimensional trends were analyzed by conducting two experimental studies. In both studies, the dimensional trends were assessed by varying the structure cell size and porosity. The methods and tools, such as X-ray microcomputed tomography imaging, optical microscopy imaging, Dragonfly

software, and nTopology software, that were utilized in conducting both studies are shown in color codes in Figure 1.4.

The second objective is realized by conducting a CAD to manufactured dimensional deviation analysis based on the two experimental studies mentioned above. The same methods and tools used to investigate the dimensional trends are used here, except for the GOM inspect software. Furthermore, the LPBF printer limitations were investigated to provide insights into the minimum wall thickness and pore size that can be successfully printed. The minimum wall thickness investigation is based on both the experimental cell size and porosity studies. However, to investigate the printer's capability in manufacturing the minimum cellular structure pore size, a separate minimum porosity study is conducted.

Regarding the third objective, a powder characterization analysis is first conducted using the Morphologi G3 particle analysis system. The powder particle shape and size for the used 2507 SDSS material are characterized and reported. Then, a porosity characterization investigation is carried out to understand the influence of the printing process parameters on the print quality. Finally, the fourth objective is addressed by optimizing the printing process parameters, namely: laser power, scan speed, and hatch distance. The optimized parameters were utilized to print highly dense parts, then mechanical and microstructure analysis was conducted to assess the print quality. Methods such as scanning electron microscopy, energy dispersive X-ray spectroscopy, and tensile testing were utilized in assessing the printed part's microstructure and mechanical properties.

In LPBF-printed cellular structures, the term porosity could either refer to the designed structure porosity (interconnected voids) that is inherent to the cellular structure or a non-designed porosity (microstructure pores) that results from the manufacturing process [15]. In this thesis, to be consistent with the literature terminologies, the term porosity was utilized to refer to both aspects.

However, to clear confusion, the term porosity used in the dimensional analysis study (Chapter 2) refers to the designed interconnected cellular structure voids. In contrast, the porosity terminology used in the printing parameter optimization study (Chapter 3) refers to the non-designed microstructure pores.

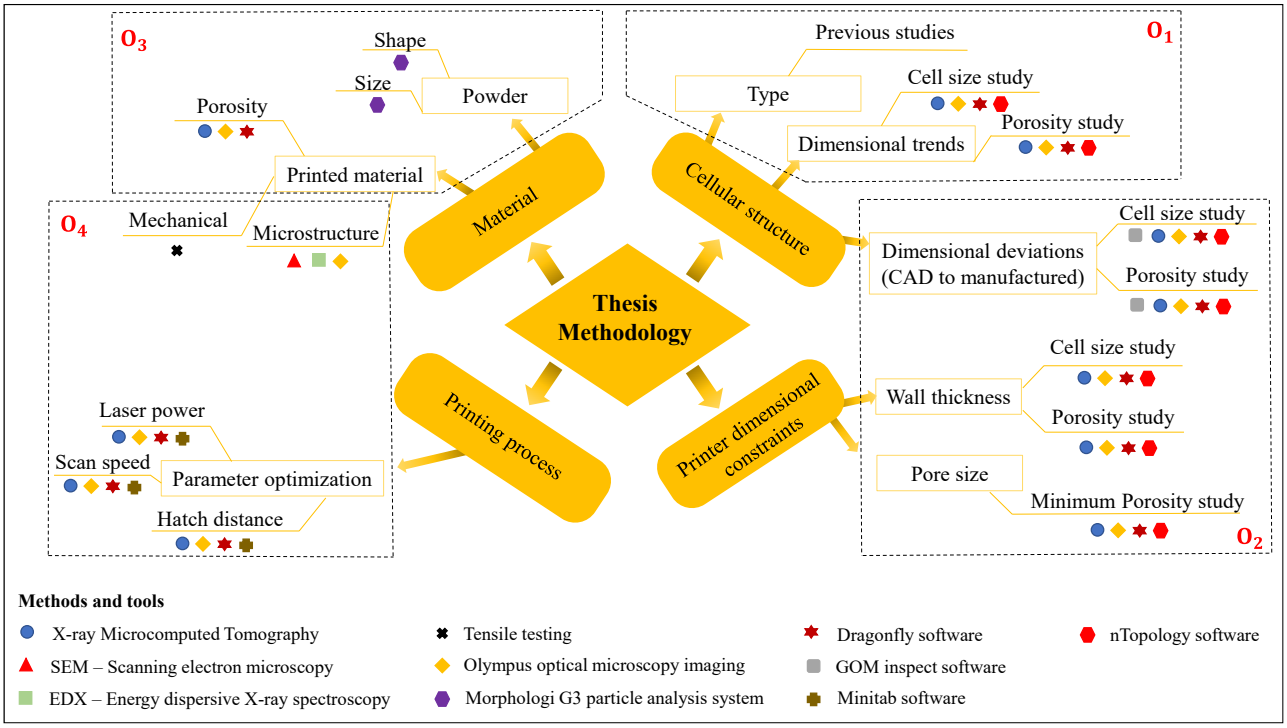

Figure 1.4: Overall thesis methodology

1.5. Thesis Outline

Chapter 1: Presents a concise background on metal additive manufacturing and cellular structures, followed by the motivations for undertaking this research. Additionally, a brief summary of the thesis's objectives and an overall thesis methodology for addressing the stated objectives are also presented.

Chapter 2: Provides a concise review of previous studies to select an optimal cellular structure for enhanced heat transfer performance. Followed by three experimental studies to investigate the

cellular structure dimensional trends, CAD to manufactured dimensional deviations, and printer's capabilities for printing thin wall thicknesses and small pore sizes (O_1 and O_2).

Chapter 3: Investigates the influence of laser power, scan speed, and hatch distance printing parameters on the resulting non-designed porosity of 2507 SDSS printed samples. The porosity characterization approach provides insights into the printing parameters optimal ranges. Therefore, following the porosity characterization analysis, an optimization approach is conducted to find a set of optimized printing parameters capable of manufacturing highly dense 2507 SDSS parts (O_3 and O_4).

Chapter 4: Summarizes the research work included in this thesis and the findings reached. Furthermore, this chapter also includes future research directions that can extend from the presented work. A summary of the thesis outline is illustrated in Figure 1.5.

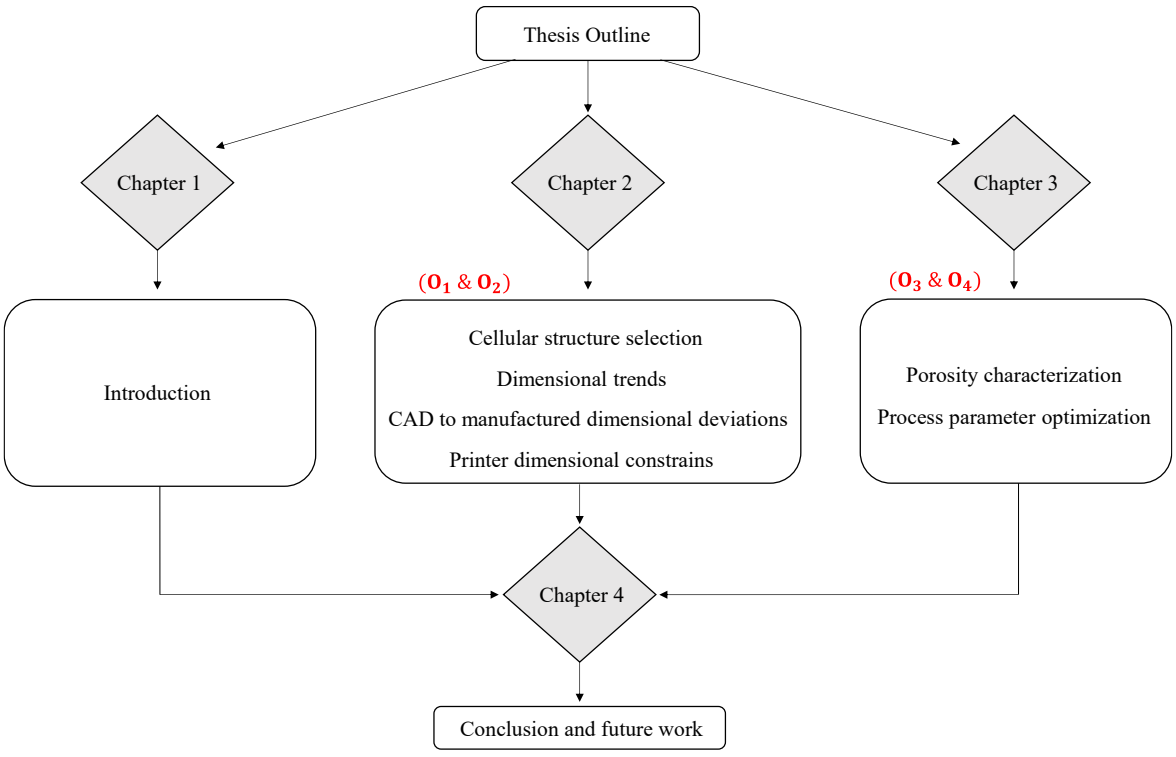

Figure 1.5: Overall thesis outline

Chapter 2: Dimensional Assessment of Uniformly Periodic Porosity Primitive TPMS Lattices Using Additive Manufacturing LPBF Technique

2.1. Introduction

LPBF is an additive manufacturing technique that uses CAD models to selectively melt metal powders layer by layer, generating complex 3D parts without further tooling [16–18]. This technique has enabled new shape [19] and material [20] design perspectives that otherwise be impossible to achieve using conventional methods. As a result, researchers started investigating various complex cellular structures due to their superior mechanical and thermal performance in multiple applications. Cellular structures are classified based on void arrangements into two categories, i.e., stochastic (non-ordered foams) and periodic (ordered lattices), while the latter is subdivided into strut-based and surface-based lattices [21,22]. The thermo-mechanical behavior of cellular structures has been heavily investigated; studies have shown that the geometry, connectivity, and design of cellular structures significantly influence their density, load-bearing, energy absorption, and thermal properties [23]. Furthermore, it was reported that lattice structures exhibited enhanced thermo-mechanical property profiles than stochastic foams at the same volume fraction [24–27], which has shifted the attention towards lattice structures.

Gu et al. [28] studied the thermo-mechanical performance of strut-based lattice structures. It was found that due to the geometry of the strut-type lattice, optimization either favored structural stiffness or thermal performance. However, compared to strut-type lattice structures, the triply periodic minimal surface (TPMS) lattice structure, which belongs to the surface-based lattices, can address this issue by achieving high specific stiffness and improved thermal performance. Wong et al. [29,30] investigated the heat transfer of a strut-based pin-fin heat exchanger. The struts were found to be too thin to offer adequate thermal conductivity. As a result, there was a significant

temperature gradient over the strut length, lowering the effective fin efficiency. Furthermore, due to strut features alignment in the fluid flow direction, the fluid flow had poor contact with the inner lattice geometry, affecting the heat transfer performance. However, TPMS lattice structures address both issues as these lattices are self-supported without strut features [31].

Lately, TPMS lattices have been gaining increasing interest among researchers, especially in heat transfer applications. TPMS lattices are mathematically derived unit cells having topologies with entangled surfaces of zero mean curvature (i.e., at each point, the sum of principal curvatures is zero) [32,33]. The 3D periodic TPMS structure allows for the generation of highly porous lattices, where pores are smoothly interconnected with no geometric discontinuities [34], which is one reason for achieving enhanced heat transfer performance. Smith et al. [31] studied the thermal conductivity of three TPMS types, namely: Gyroid, Diamond, and Primitive. It was found that the Primitive TPMS (PTMPS) structure consistently showed the highest thermal conductivity, which was attributed to the increase in the lattice wall thickness compared with the gyroid and diamond lattices. Qureshi et al. [35,36] have investigated the use of TPMS lattices (i.e., Primitive, Gyroid and IWP) as a matrix to enhance the heat transfer performance in a phase change material used for thermal energy storage systems. Simulations under the buoyancy effect showed that the Primitive TPMS structure exhibited the highest heat transfer improvement compared with the Gyroid and IWP, which was only attributed to the topology of the structure. This shows the heat transfer performance superiority of Primitive TPMS among the TPMS lattice family. As a result, the Primitive TPMS lattice structure was selected for the proposed cellular-walled pipe heat sink system.

It can be established that the heat transfer performance in lattice structures is significantly dependent on the cell topology (i.e., cell shape, porosity, and thickness). This shows the

importance of analyzing the lattice dimensional trends and deviations between the CAD data and the manufactured lattices. Lately, researchers have been focused on investigating the dimensional deviations (i.e., accuracy analysis) in additively manufactured lattice structures. Yan et al. [37] investigated the CAD to manufactured strut size variation of LPBF printed gyroid lattice structures and found an increase in the manufactured strut sizes than CAD. Sing et al. [38] investigated the dimensional accuracy of lattice structures and reported a decrease in the lattice-manufactured strut size than CAD. The contradiction in results is attributed to the followed approach in measuring the strut size, where Yan considered the adhered powders to be part of the strut size. However, Sing did not account for the adhered powder particles as part of the strut size and stated that the adhered powder particles (i.e., not fully melted particles) behave differently than the melted powder. Weidmann et al. [39] analyzed the manufacturing of aluminum honeycomb lattice structures and found that significant deviations are present when many hexagonal segments merge from a single node which is also the case with thin-structured lattices. Großmann et al. [40] investigated the effect of laser power and scan speed on the strut diameter of strut-based lattices. Their findings showed an increase in the strut size of thin-walled lattices with increasing the laser power or decreasing the scanning speed. Grunsven et al. [41] compared the CAD to manufactured dimensional deviations of parts fabricated by electron beam melting (EBM). It was found that variations between the CAD and manufactured strut size were approximately 200 μm. Lopez et al. [42] investigated the dimensional variations of cubic and honeycomb lattices produced by LPBF. Their findings indicate that lattices with fine struts (250 μm) resulted in higher dimensional relative error between 5% to 25%. However, to the author's best knowledge, dimensional accuracy analysis of PTPMS lattices has not been investigated yet.

The dimensional assessment of the Primitive TPMS lattice structure is a crucial step in understanding the thermal performance of such a structure. In lattice structure heat transfer applications, the lattice porosity and cell size are the main variants that define the resulting lattice wall thickness, surface area to volume ratio (SA:Vol), and pore size. As such, the lattice dimensional behavior at varying lattice porosity and cell size must be analyzed to fully understand its thermal performance. This study provides a comprehensive investigation of the PTPMS lattice's various dimensional trends and CAD to manufactured deviations under varying lattice cell size and porosity. Moreover, the minimum allowable wall thickness and pore size that can successfully be printed is investigated as well. The metal powder material selected is 17-4 PH stainless steel (17-4 PH SS). Its unique combination of higher strength and corrosion resistance, among other steel grades, is suited for applications requiring up to 315°C thermal exposures [43]. The data presented here can serve as preliminary work that leads to comprehensive research about the PTPMS heat transfer performance. Further, the dimensional analysis conducted can be used as a stand-alone guide in selecting appropriate PTMPS lattice design parameters for the cellular-walled pipe heat sink system.

2.2. Materials and Methods

2.2.1. Powder Material

The material used in printing the samples is 17-4 PH SS provided by Oerlikon (Alberta, Canada). The chemical composition of 17-4 PH SS is shown in Table 2.1. The powder material morphology has a significant impact on the quality of printed parts; parameters such as particle size distribution and shape influence the quality and dimensional accuracy of the prints [44,45]. The Morphologi G3 particle analysis system provided by Malvern Panalytical (Malvern, UK) was used to qualitatively characterize the powder morphology. The characterization process (Figure 2.1) was

based on 228948 counted particles. It was found that the powder particles are mostly spherical with a circularity average of 90.2 ± 12.4 % and an average particle size of 25.67 ± 13.72 µm. The reported circularity standard deviation of 12.4 % is only applicable to the lower bound; however, the upper bound should be capped at 100%.

Table 2.1: 17-4 PH SS chemical composition

Element	Fe	Cr	Ni	Cu	Mn	Si	Ta	Nb	Nb + Ta	C	P	S
Content (%)	73	15.0 - 17.5	3 - 5	3 - 5	1	1	0.45	0.45	0.15 - 0.45	0.07	0.04	0.03

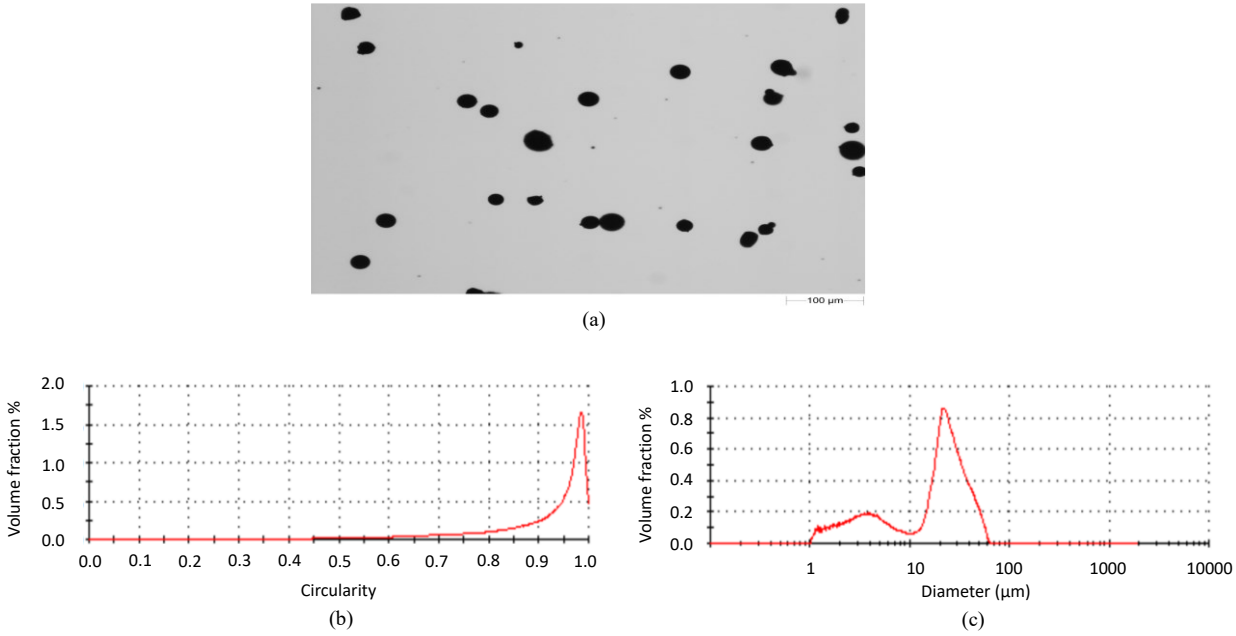

Figure 2.1: 17-4 PH SS particle morphology: (a) Micrograph of 17-4 PH SS particles; (b) particle circularity; (c) particle size distribution.

2.2.2. LPBF process parameters

The printing process parameters significantly influence the dimensional accuracy of the built parts [46]. Thus, ensuring optimized 17-4 PH SS printing parameters is crucial. The ORLAS Coherent 250W LPBF printer is used, and its optimized 17-4 PH SS parameters identified by Coherent were applied, as seen in Table 2.2. Moreover, the process parameters were kept constant for all printed parts conducted in this study.

Table 2.2: Printing process parameters

Process parameter	Laser spot size (µm)	Laser power (W)	Mark speed (mm/s)	Layer thickness (µm)	Hatch spacing (µm)	Track energy (J/mm)	Laser Energy Density (J/mm3)
Hatching Settings	55.118	123.2	1000	25	55	0.12	89.6
Contour Settings	55.118	107.3	800	25	55	0.13	97.5

2.2.3. Primitive TPMS lattice structure

The PTPMS lattice type is selected in this study; compared to other TPMS lattices, PTPMS showed an improved heat transfer performance among the TPMS lattice family. The PTPMS lattice structure is generated using nTopology 3.18.4 software (NYC, United States) which generates the lattice surface by a set of points based on the mathematical equation:

$$\cos(x) + \cos(y) + \cos(z) = c \qquad (2.1)$$

where $x = \frac{2\pi x}{L}$, $y = \frac{2\pi y}{L}$, $z = \frac{2\pi z}{L}$. The lattice cell size can be controlled by L, and the cell relative density can be varied by the parameter c.

The PTPMS lattice topology is illustrated in Figure 2.2. It can be observed that the lattice wall thickness and pore size vary along the Z direction (Figure 2.2 (b)). As a result, to conduct our dimensional analysis, terminologies such as "outer surface wall thickness" and "minimum pore size" were established, as seen in Figure 2.2 (a). Furthermore, the "cell size" is referred to the length of one PTPMS cell along the lattice structure and the "number of cells" indicates the number of cells along the X, Y, and Z directions. For example, a 4 number of cells indicates equally four cells in all X, Y, and Z directions, as seen in Figure 2.2 (a). In PTPMS lattices, there is a designed porosity (interconnected porosity) that is inherent to the lattice, as well as a non-designed porosity (closed porosity) that results from the manufacturing process [15]. Although the term "porosity" in this study refers to the designed porosity of the lattice; However, in the porosity quantification analysis, both aspects are considered.

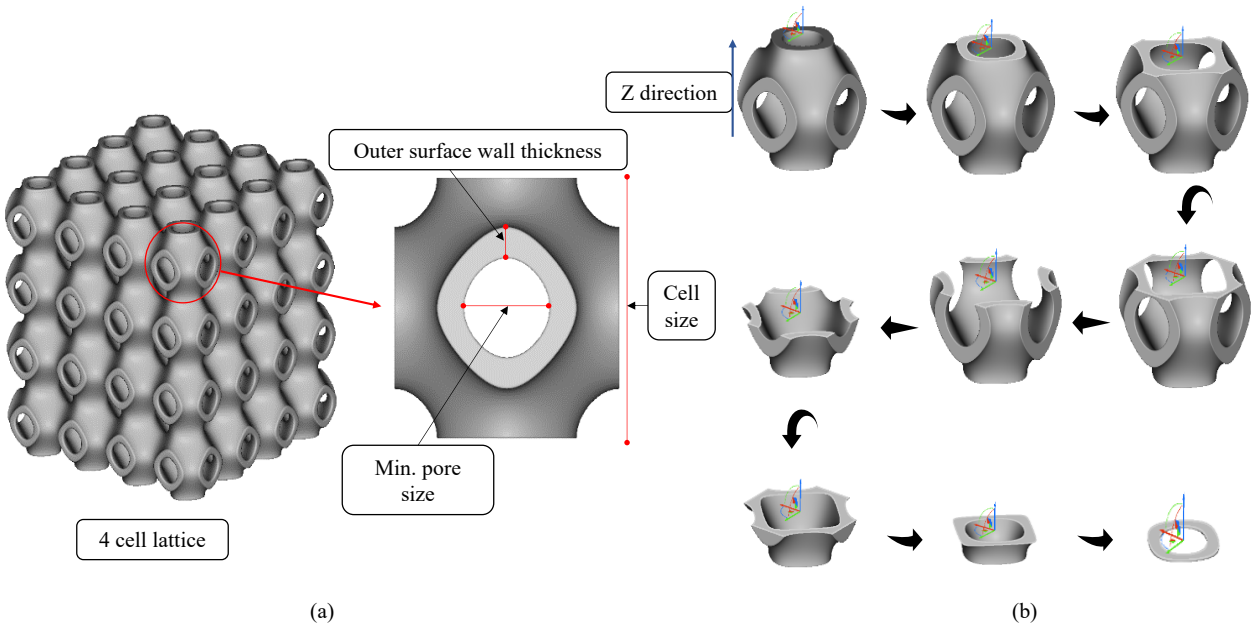

Figure 2.2: PTPMS cell topology: (a) PTPMS lattice cell shape and terminologies; (b) PTPMS cell top to bottom cross-section.

2.2.4. Design of experiments

The lattice heat transfer performance is usually analyzed through conduction and convection modes which are dependent on the lattice wall thickness and lattice surface area to volume ratio (SA:Vol), respectively [31]. Moreover, regarding the PTPMS lattice structure, the cell size and porosity (i.e., lattice voids) significantly influence the resulting lattice wall thickness and SA:Vol ratio. Hence, the designed experiments in this study were focused on varying the lattice cell size and porosity. Furthermore, the minimum lattice wall thickness and the reliable minimum pore size that can successfully be printed were also investigated to explore the printer's capabilities. Figure 2.3 illustrates the overall conducted experiments and their objectives. A total of 19 samples were generated using nTopology. Parameters such as cell size, number of cells, min. pore size, porosity, surface area to volume ratio, lattice average wall thickness, and outer surface wall thickness (**OS** wall thickness) are investigated.

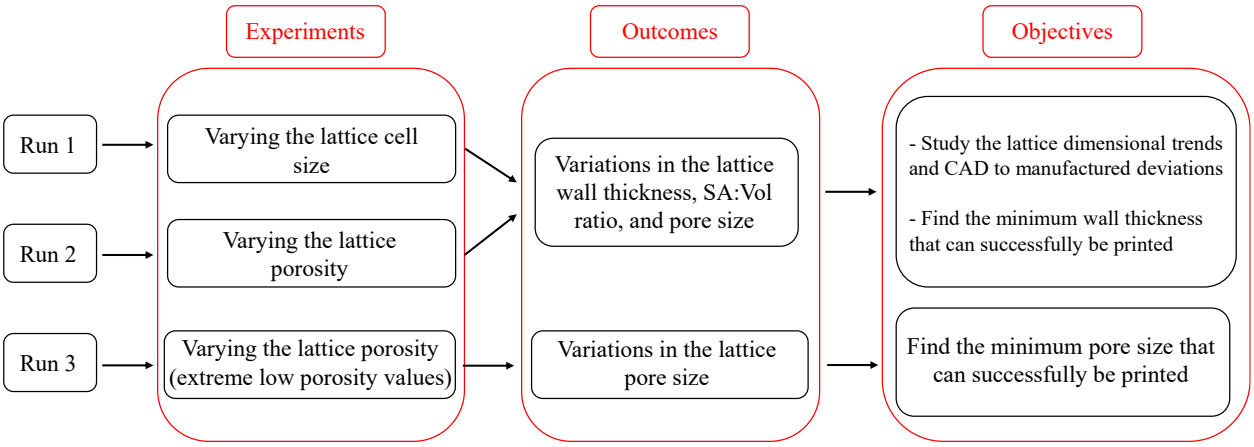

Figure 2.3: Design of experiment methodology

2.2.4.1. PTPMS lattices at a varying cell size (Run 1)

Varying the lattice cell size at a given porosity significantly influences the lattice's various parameters (i.e., lattice wall thickness, SA:Vol ratio, and lattice pore size). These parameters play a profound role in determining the lattice thermal performance profile. As a result, investigating the cell size effect on the lattice dimensional parameters is of significant importance. Table 2.3 shows PTPMS lattices with varying cell sizes from 2.9 to 10 mm at a constant 85% porosity. Further, the overall sample size was kept constant at (20×20×20) mm. The cell size range was identified as generating cell sizes larger than 10 mm increases the pore size, which leads to an upper overhang structure causing cell deformation, and generating cell sizes smaller than 2 mm requires large computational memory and time [47]. Due to the fixed sample dimensions of (20 x 20 x 20) mm, a cell size range from 2.9 to 10 mm was selected to achieve a whole number of cells from 7 to 2, respectively. The selected constant porosity of 85% presents the typical porosity value at which lattice structures are usually manufactured.

Table 2.3: Varying PTPMS lattice cell size at constant porosity (CAD results).

Run 1	Sample Dimensions (mm)	Cell size (mm)	Number of cells	Porosity %	Min. Pore size (mm)	SA:Vol (mm-1)	OS wall thickness (mm)	Overall average wall thickness (mm)
1	20 x 20 x 20	2.9	7	85	1.207	11.06	0.222	0.126
2		3.3	6	85	1.384	9.50	0.266	0.146
3		4.0	5	85	1.661	7.97	0.283	0.175
4		5.0	4	85	2.076	6.41	0.387	0.219
5		6.7	3	85	2.786	4.84	0.533	0.293
6		10.0	2	85	4.152	3.30	0.811	0.439
Refer to Figure 2.2 for terminology definitions								

2.2.4.2. PTPMS lattices at a varying porosity (Run 2)

The lattice porosity is the amount of generated interconnected voids within the lattice. Varying the lattice porosity at a given cell and sample size significantly influences the lattice dimensional parameters, which defines the overall lattice heat performance. Thus, investigating the porosity influence on the resulting lattice parameters is of significant importance. Table 2.4 shows PTPMS lattices with a varying porosity of 45 to 90 % at a constant 4 mm cell size and a fixed sample size of (20×20×20) mm. The selected porosity range is the typical range used for lattice structures, as with porosities above 90 %, the lattice features become too thin to be printed via LPBF [31]. On the other hand, a lattice with less than 45% porosity loses its value in heat transfer applications as it becomes more of a solid rather than a lattice structure. The constant cell size of 4 mm was selected based on the results of Run 1 which will be discussed later.

Table 2.4: Varying PTPMS lattice porosity at constant cell size (CAD results).

Run 2	Sample Dimensions (mm)	Cell size (mm)	Number of cells	Porosity %	Min. Pore size (mm)	SA:Vol (mm-1)	OS wall thickness (mm)	Overall Average wall thickness (mm)
1	20 x 20 x 20	4	5	45	0.361	1.97	1.570	0.638
2		4	5	55	0.847	2.54	1.127	0.523
3		4	5	65	1.160	3.35	0.770	0.408
4		4	5	75	1.421	4.75	0.539	0.292
5		4	5	85	1.661	7.97	0.283	0.175
6		4	5	87	1.707	9.18	0.271	0.152
7		4	5	90	1.775	11.93	0.190	0.117

2.2.4.3. Smallest PTPMS pore size study (Run 3)

This experiment is aimed at studying the printer's limitation in printing the smallest pore size. A sample size of (6 x 6 x 6) mm was selected with a cell size of 3 mm and a porosity range from 45 to 50%. Table 2.5 shows a varying min. pore size range from 0.257 to 0.482 mm. The selected pore size range in this study is based on the required range of 0.1-0.7 mm to prevent pore occlusion [48].

Table 2.5: Varying PTPMS min. pore size.

Run 3	Sample Dimensions (mm)	Cell size (mm)	Number of cells	Porosity %	Min. Pore size (mm)
1	6 x 6 x 6	3	2	45	0.257
2		3	2	46	0.317
3		3	2	47	0.359
4		3	2	48	0.400
5		3	2	49	0.441
6		3	2	50	0.482

2.2.5. Characterization Methods

There are multiple metrology techniques used to study manufactured parts via the LPBF process. In recent years, X-ray microcomputed tomography (μCT) has been used as a reliable non-destructive method in evaluating and assessing additively built parts, particularly for dimensional measurement and porosity characterization [49]. In this study, ZEISS Xradia 620 Versa X-ray μCT with a current of 150.07 μA, a voltage of 140 kV, a power of 21.01 W, and an exposure time of 1 s was utilized in generating the CT reconstructed PTPMS lattices. Next, Dragonfly (Version 2021.1 Build 977) software was used to characterize the porosity and SA:Vol ratio of the scanned PTPMS lattice structures. The characterization process was based on three repeated measurements, and an average was calculated and reported. Dragonfly quantification analysis is based on the image color segmentation method where each 3D CT reconstructed sample is composed of multiple slices and each slice is color segmented to distinguish between the matrix (i.e., material) and porosity (i.e., voids). A model was trained to accurately segment the PTPMS lattice samples,

where the trained model was used to segment all the PTPMS lattices analyzed in this study and hence ensuring the same segmentation process approach for all samples. Figure 2.4 shows the trained model segmentation results of a 3-cell PTMPS lattice slice image where colors "purple and green" depict the PTPMS lattice matrix and voids, respectively.

The Olympus Optical microscope with a 5X magnification was utilized to measure both the "OS wall thickness" and "min. pore size" of the PTPMS lattices. For each sample, measurements were based on three readings and an average was calculated and reported. Moreover, Sing's approach [38] is followed in this study, where the adhered powder particles are neglected and not considered in the measurements, as seen in Figure 2.5. Finally, GOM inspect 2021 was utilized to generate a lattice CAD to manufactured volume deviation color maps, where the µCT 3D reconstructed stl. model is merged with the nominal stl. CAD model to compare volume deviations.

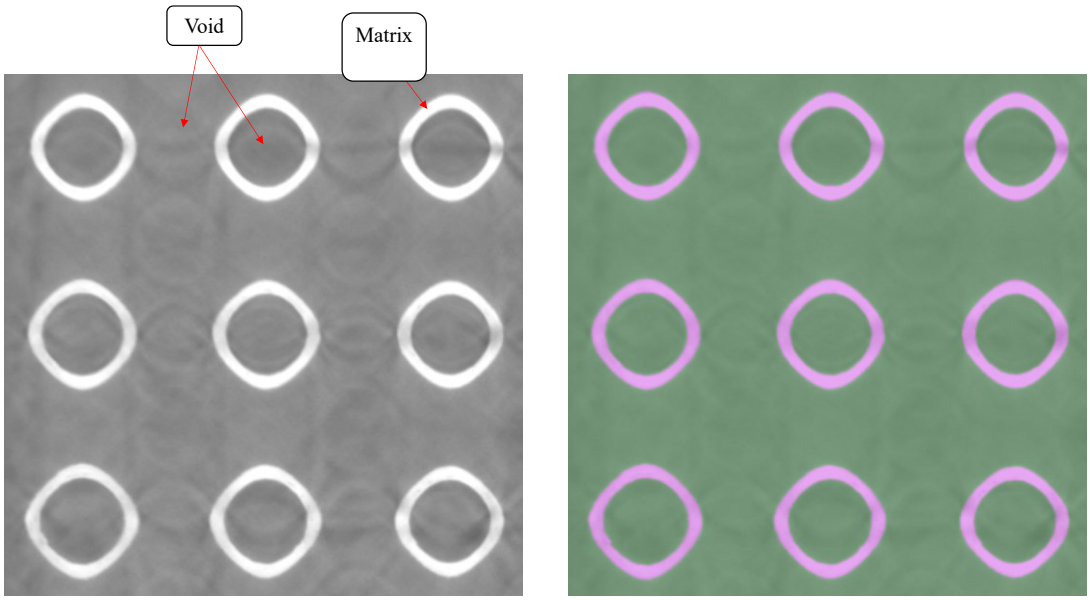

Figure 2.4: : Dragonfly trained model segmentation process of 3 cells PTPMS lattice: (a) a CT scanned slice image; (b) Color segmentation process.

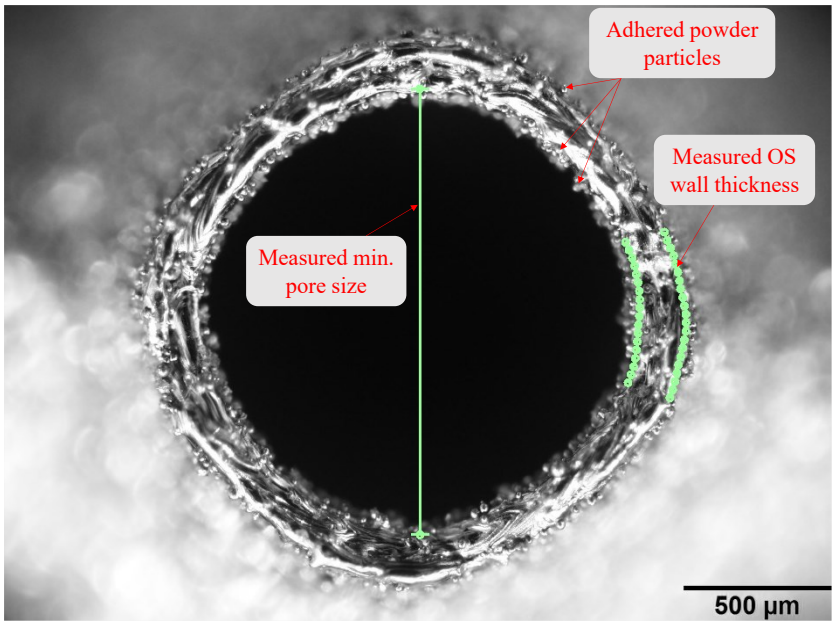

Figure 2.5: Wall thickness and pore size measurement approach.

2.3. Results and discussion

2.3.1. PTPMS lattice cell size study (Run 1)

Figure 2.6 shows the 17-4 PH SS successfully printed samples with a cell size range from 2.9 to 10 mm, which corresponds to PTPMS lattices with cell numbers from 7 to 2, respectively. The various dimensional parameters were measured and reported, as seen in Table 2.6. Figure 2.7 illustrates the various CAD and manufactured parameter trends as a result of increasing the cell size at a constant porosity. Regarding the lattice wall thickness, it can be seen that the outer surface wall thickness increases with increasing the lattice cell size Figure 2.7 (a & d), where at a cell size of 2.9 mm, a corresponding manufactured OS wall thickness of 0.160 mm is calculated; however, as the cell size increases to 10 mm, a corresponding average OS wall thickness increase of 0.525 mm is observed. This observation is consistent with the CAD values seen in Table 2.3 & Figure 2.7 (a), where increasing the cell size from 2.9 to 10 mm showed an overall increase of 0.589 mm in the OS wall thickness. As such, it can be established that the overall average wall thickness increases with increasing the lattice cell size. Moreover, this lattice behavior is predicted as

increasing the cell size decreases the number of cells within the lattice; thus, to maintain a constant porosity (i.e., constant volume fraction), the lattice wall thickness is increased to compensate for the reduction in the number of cells.

On the other hand, the lattice SA:Vol ratio is inversely proportional to increasing the cell size Figure 2.7 (b & e), where increasing the cell size from 2.9 to 10 mm showed a decrease in the manufactured SA:Vol ratio from 11.54 to 3.68 mm^{-1} with a total reduction of 7.86 mm^{-1}. This reduction value is consistent with the CAD value seen in Table 2.3 & Figure 2.7 (b) with a calculated total reduction of 7.76 mm^{-1}. Furthermore, since the porosity is designed to be constant for all samples (i.e., the volume fraction is constant), the reduction in the SA:Vol ratio with increasing the cell size is mainly due to the decrease in the lattice surface area, where it reduced from 2793.84 to 865.59 mm^2 with increasing the cell size from 2.9 to 10 mm, respectively. The reduction in the surface area is once again attributed to the reduction in the number of cells, which ultimately reduces the amount of available surface area.

Figure 2.7 (c & f) shows the linear relationship between the min. pore size and lattice cell size. It can be observed that an increase in the cell size is followed by an increase in the min. pore size, where increasing the cell size from 2.9 to 10 mm showed an increase in the manufactured min. pore size from 1.302 to 4.364 mm, respectively. The increase in pore size of the manufactured samples is consistent with the increase in the CAD values seen in Table 2.3 & Figure 2.7 (c), with a total pore size increase from 1.207 to 4.152 mm. As such, it can be established that increasing the lattice cell size results in an increase in the lattice's overall pore size.

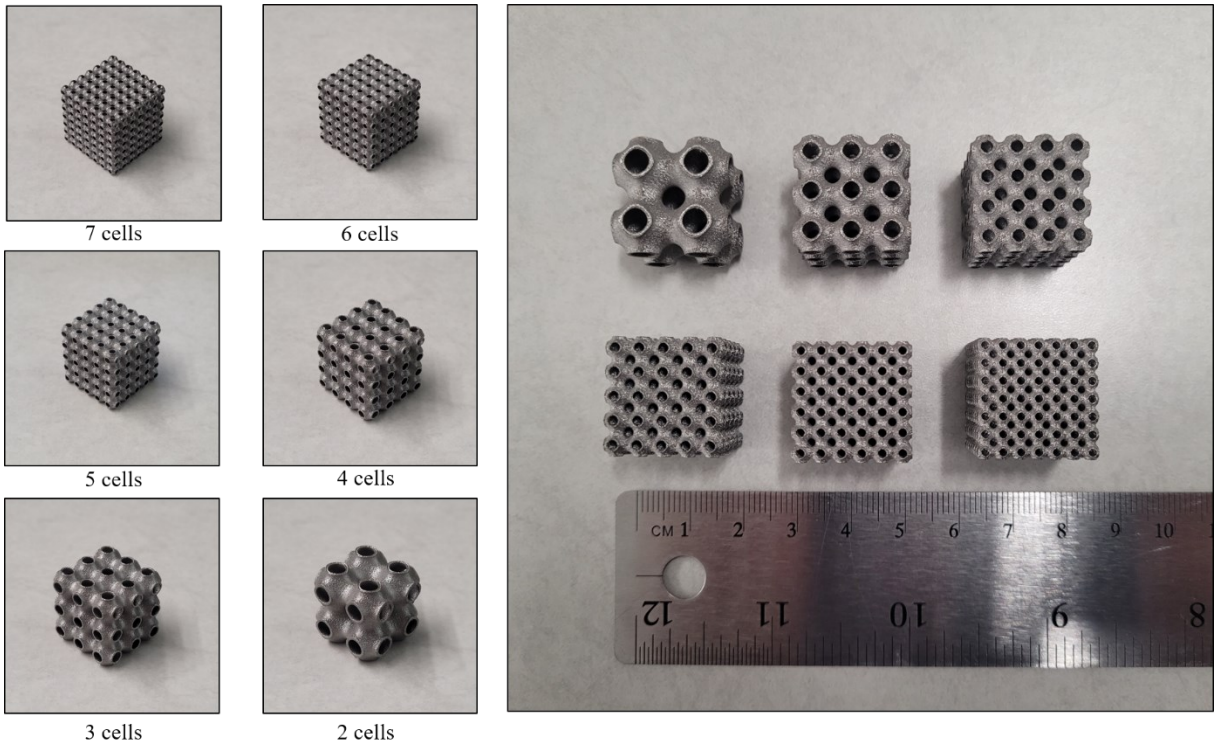

Figure 2.6: Varying cell size printed PTPMS lattices at a constant porosity.

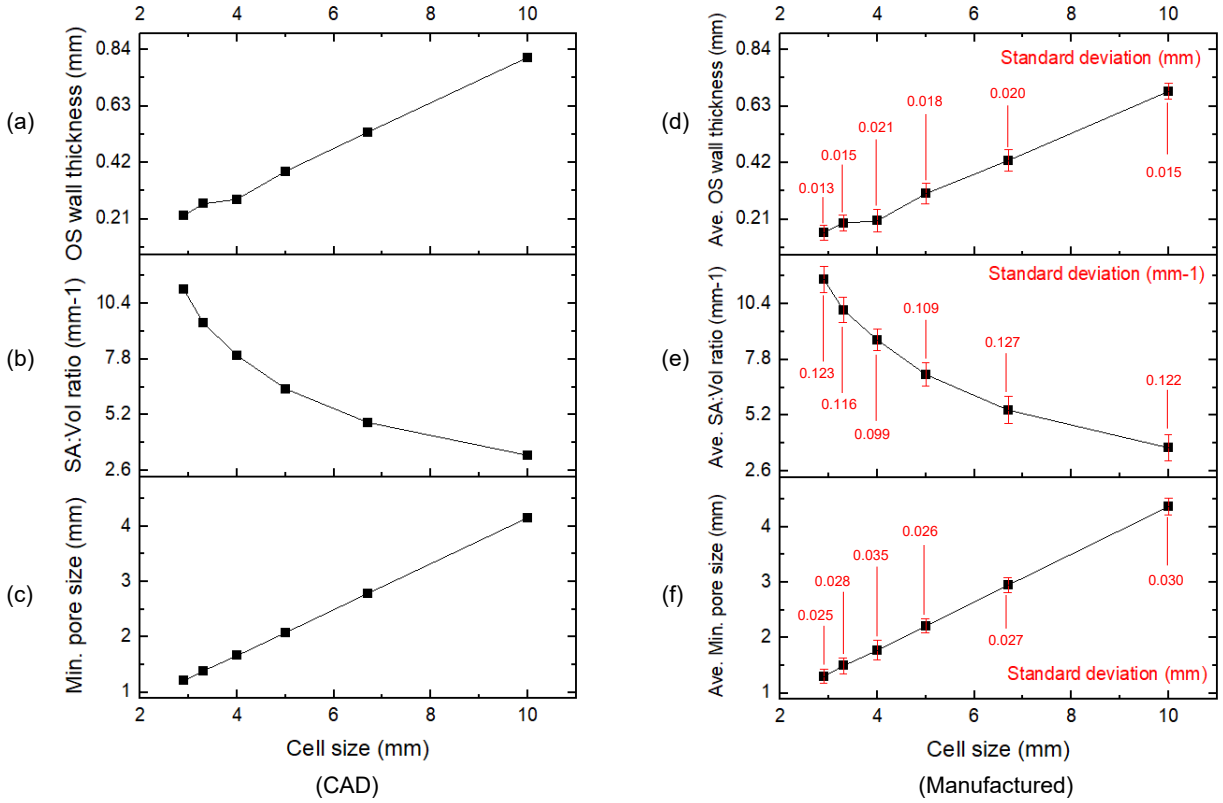

Figure 2.7: Cell size effect on PTPMS dimensional parameters: (a-c) CAD values; (d-f) manufactured values.

- **CAD to manufactured dimensional deviation**

Table 2.7 illustrates the various CAD to manufactured parameter deviations based on the equation:

$$\text{Parameter deviation} = \text{manufactured measurement} - \text{CAD measurement} \quad (2.3)$$

Regarding the OS wall thickness, it is evident from Figure 2.8 (a) that irrespective of the lattice cell size, the manufactured OS wall thickness constantly showed lower values than CAD, which indicates an overall shrinkage in all printed samples, hence the negative OS wall thickness deviation values in Table 2.7. Similar findings were reported in Sing's study [38], where a reduction in the printed strut thickness was observed. The shrinkage of printed metal parts is a well-known phenomenon in LPBF, where the rapid cooling and change in material phase from powder to liquid, then solid, is followed by an induced shrinkage [50–52]. Liu et al. [53] investigated the printing process parameter influence on the overall shrinkage of selective laser melting (SLM) printed samples; their study showed that the laser power, scan speed, and layer thickness significantly affect the resulted sample shrinkage; however, in this study, the printing process parameters were fixed in all samples. Hence, shrinkage variation is only attributed to sample geometry differences. Figure 2.8 (b) shows the CAD to manufactured OS wall thickness deviation with increasing the lattice cell size, it can be observed that increasing the cell size shows higher wall thickness deviations (i.e., lower thickness accuracy), where the 2.9 mm and 10 mm cell size lattices showed the smallest and highest deviations of -61.564 μm and -126.158 μm, respectively. Moreover, this observation indicates that increasing the lattice cell size (at a constant porosity) results in an increase in the overall shrinkage during the building process, which leads to higher CAD to manufactured wall thickness deviations. Thus, to further support this claim, GOM inspect 2021 software (ZEISS Group, Germany) was utilized to conduct a lattice CAD to manufactured volume deviation color map study on 2.9, 4, and 10 mm cell size samples, as seen

in Figure 2.9. Results showed that the 2.9 mm cell size lattice Figure 2.9 (a) exhibited the least overall shrinkage with an average shrinkage value of 0.19 mm, followed by the 4 mm cell size lattice Figure 2.9 (b) with 0.25 mm, then the 10 mm cell size lattice Figure 2.9 (c) with the highest average shrinkage of 0.63 mm. Therefore, it can be established that increasing the cell size at a constant porosity (i.e., at a constant volume fraction) shows higher shrinkage rates which ultimately influence the lattice dimensional accuracy (in this case, the lattice wall thickness). This can be attributed to the increase in heat conduction with increasing the lattice cell size (i.e., increasing the lattice wall thickness), which leads to higher cooling rates in added layers, and hence higher shrinkage rates are observed. Chahal et al. [54] reported a similar shrinkage dependency, where they correlated the induced layer shrinkage to the base plate's high heat conduction and considerably lower temperatures. Further, they stated that the printed layer's effective heat conductivity is influenced by the underlying geometric features. Moreover, Gan et al. [55] studied the effect of various support structure designs on the final plate print. It was concluded that differential shrinkage was observed due to varying thermal gradients along the plate's length. As such, it can be established that at fixed printing process parameters, layer shrinkage has a direct correlation to the thermal gradient which is geometry dependent.

The SA:Vol ratio is another parameter investigated in this study. It is defined as the overall lattice surface area divided by the manufactured lattice volume. It can be seen from Figure 2.8 (c) that at all cell sizes, the resulting manufactured SA:Vol ratio is consistently higher than the CAD ratio. This can be attributed to the shrinkage influence on the volume, where the manufactured volume is less than the designed volume, leading to the increase in the manufactured SA:Vol ratio. Figure 2.8 (d) illustrates the CAD to manufactured SA:Vol ratio deviation values with respect to increasing the cell size. It was previously shown that decreasing the cell size at a constant volume

fraction increases the lattice surface area, which results in an increased number of cells that adds to the complexity of the lattice structure. Moreover, it is evident from Figure 2.8 (d) that decreasing the lattice cell size (i.e., increasing the lattice surface area) increases the CAD to manufactured SA:Vol ratio deviation, where both the 10 mm and 4 mm cell size samples exhibited the lowest and highest deviations of 0.37 and 0.74 mm^{-1}, respectively. However, a deviation decrease is noticed as the cell size is decreased from 4 to 2.9 mm with a CAD to manufactured SA:Vol ratio deviation decrease from 0.74 to 0.48, respectively. This decrease in deviation can be linked to the fact that at lower cell sizes, very thin lattice wall thicknesses are present, as indicated by the average wall thickness of less than 150 μm (Table 2.3), resulting in high thermal gradients. Chahal et al. [54] investigated the geometry influence on the non-designed porosity, where it was found that severe changes in thermal gradients could develop non-designed porosities. As such, the inner morphology of the 3.3 mm cell size lattice sample was investigated using the CT reconstructed model. It can be observed from Figure 2.10 that inner gaps are present within the 3.3 mm lattice structure, causing surface area reductions which results in a SA:Vol ratio deviation reduction. As a result, it can be established that a minimum overall average wall thickness of 0.175 mm seen in Table 2.3, is required to avoid the formation of non-designed porosity within the lattice structure.

Table 2.6: Varying the PTPMS lattice cell size at a constant porosity.

Cell size (mm)	Number of cells	CAD				Manufactured							
		Porosity %	Min. pore size (mm)	SA:Vol (mm-1)	OS wall thickness (mm)	Average Porosity %	Porosity standard deviation %	Average Min. pore size (mm)	Min. pore size standard deviation (mm)	Average SA:Vol (mm-1)	SA:Vol standard deviation (mm-1)	Average OS wall thickness (mm)	OS wall thickness standard deviation (mm)
2.9	7	85	1.207	11.06	0.222	85.98	0.097	1.302	0.025	11.54	0.112	0.160	0.013
3.3	6	85	1.384	9.50	0.266	85.50	0.103	1.493	0.028	10.11	0.116	0.195	0.015
4.0	5	85	1.661	7.97	0.283	85.23	0.096	1.772	0.035	8.71	0.099	0.204	0.021
5.0	4	85	2.076	6.41	0.387	85.47	0.089	2.214	0.026	7.10	0.109	0.305	0.018
6.7	3	85	2.786	4.84	0.533	85.61	0.081	2.950	0.027	5.44	0.127	0.428	0.020
10.0	2	85	4.152	3.30	0.811	86.36	0.090	4.364	0.030	3.68	0.122	0.685	0.015

Table 2.7: CAD to manufactured parameter deviations.

Cell size (mm)	Number of cells	CAD				Manufactured				CAD to manufactured deviation			
		OS wall thickness (mm)	SA:Vol (mm-1)	Min. pore size (mm)	Porosity %	Average OS wall thickness (mm)	Average SA:Vol (mm-1)	Average Min. pore size (mm)	Average Porosity %	OS wall thickness deviation (µm)	SA:Vol ratio deviation (mm-1)	Min. pore size deviation (µm)	Porosity deviation %
2.9	7	0.222	11.06	1.207	85	0.160	11.54	1.302	85.98	-61.564	0.48	94.620	0.98
3.3	6	0.266	9.50	1.384	85	0.195	10.11	1.493	85.50	-70.766	0.60	109.165	0.50
4.0	5	0.283	7.97	1.661	85	0.204	8.71	1.772	85.23	-78.483	0.74	111.430	0.23
5.0	4	0.387	6.41	2.076	85	0.305	7.10	2.214	85.47	-82.260	0.68	138.538	0.47
6.7	3	0.533	4.84	2.786	85	0.428	5.44	2.950	85.61	-105.344	0.59	164.400	0.61
10.0	2	0.811	3.30	4.152	85	0.685	3.68	4.364	86.36	-126.158	0.37	212.080	1.36

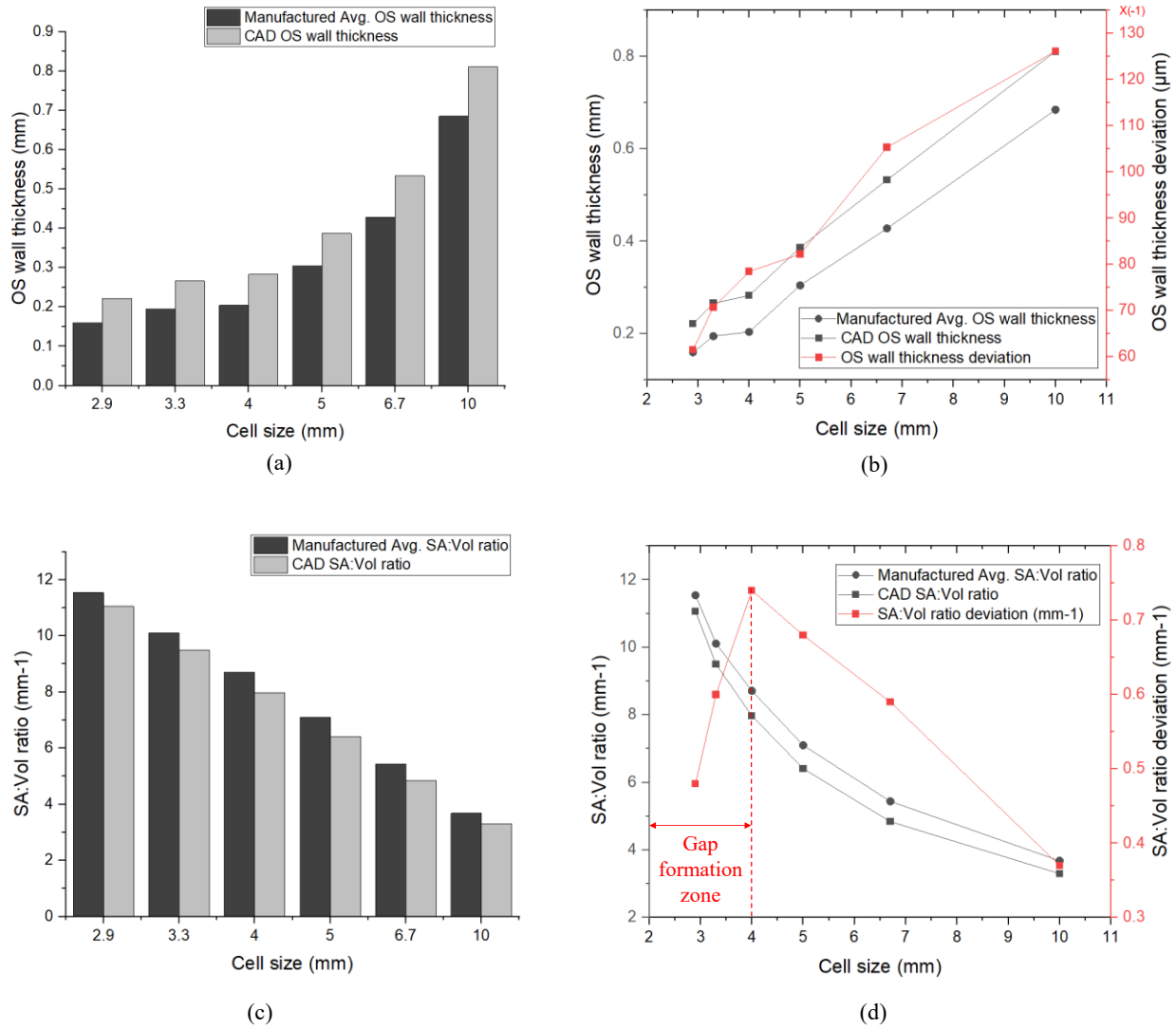

Figure 2.8: CAD to manufactured comparison of OS wall thickness and SA:Vol ratio parameters: (a&c) CAD to manufactured results; (b&d) CAD to manufactured deviations.

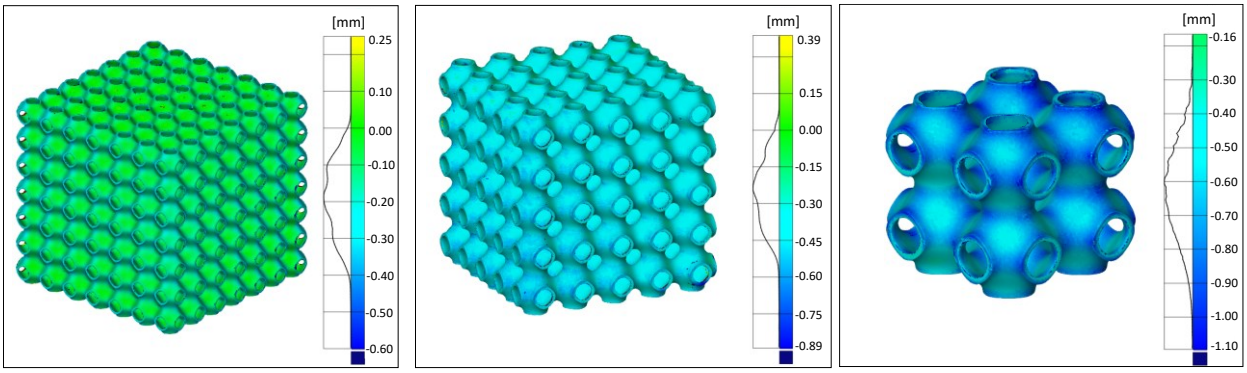

Figure 2.9: CAD to manufactured Volume deviation color map of PTPMS lattices: (a) 2.9 mm cell size; (b) 4 mm cell size; (c) 10 mm cell size.

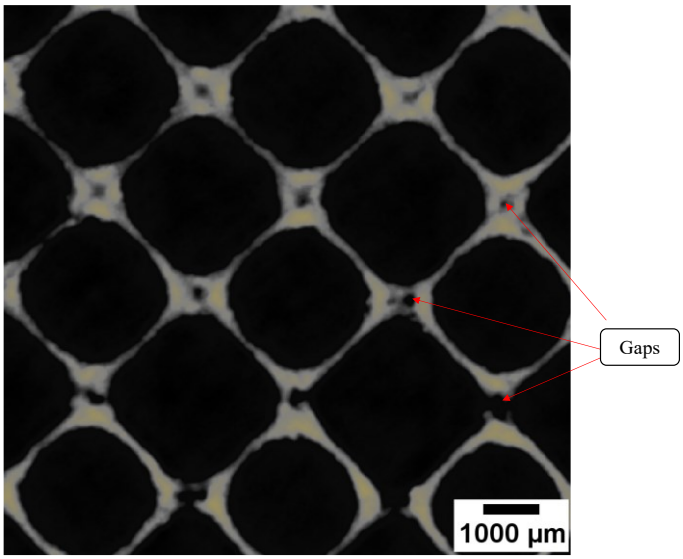

Figure 2.10: Inner morphology CT cross-section image of a 3.3mm cell size PTPMS lattice structure.

The lattice cell size influence on the min. pore size and porosity is investigated, as seen in Figure 2.11. Regarding the min. pore size, it can be observed that irrespective of the lattice cell size, the manufactured min. pore size is consistently higher than the CAD values (Figure 2.11 (a)). This can once again be attributed to shrinkage, where the surface shrinkage of a hole structure will eventually result in an increase in the hole size. The increase in the cell size (i.e., increase in shrinkage) showed higher CAD to manufactured min. pore size deviations, as seen in Figure 2.11 (b), where increasing the cell size from 2.9 to 10 mm resulted in a deviation increase from 94.620 to 212.080 µm. Furthermore, Figure 2.11 (c) shows the resulting overall porosities at various cell sizes. It can be seen that the manufactured porosity is observed to be higher than the designed porosity for all samples which can be attributed to shrinkage as well, where achieving less volume fractions than designed will eventually result in higher manufactured porosities based on the equation [56]:

$$\text{Porosity\%} = 1 - \text{Volume fraction} \qquad (2.4)$$

Smith et al. [31] noticed a similar behavior with the Hastelloy-X TPMS samples, where the manufactured PTPMS samples showed a volume fraction reduction than the designed samples.

A porosity CAD to manufactured deviation analysis is seen in Figure 2.11 (d), it can be observed that the 4 mm cell size showed the lowest porosity deviation of 0.23 %, whereas increasing the cell size above 4 mm showed a deviation increase due to the increased shrinkage and decreasing the cell size below 4 mm resulted in a deviation increase due to the production of gaps as previously discussed. Hence, the 4 mm cell size was selected for Run 2.

Depending on the heat transfer application of the cellular-walled pipe heat sink system, certain considerations should be regarded with increasing the PTPMS lattice cell size. If it is desirable to improve the thermal conductivity of the PTPMS lattice structure, increasing the lattice cell size to provide higher wall thicknesses (i.e., wider conduction pathways) should be considered. However, increasing the lattice cell size will result in higher shrinkage rates leading to higher CAD to manufactured dimensional variations, which will significantly affect the heat transfer analysis results between the numerical modeling (based on CAD models) and experiments (based on manufactured models). On the other hand, if it is desired to improve the thermal convection of the PTPMS lattice structure, decreasing the cell size (i.e., increasing SA:Vol ratio) is preferred to enhance the interaction between the flow and lattice structure. However, it is important to ensure a cell size that is not too small (i.e., achieving an average wall thickness less than 0.175 mm) to cause inner gaps, which will poorly affect the heat transfer performance.

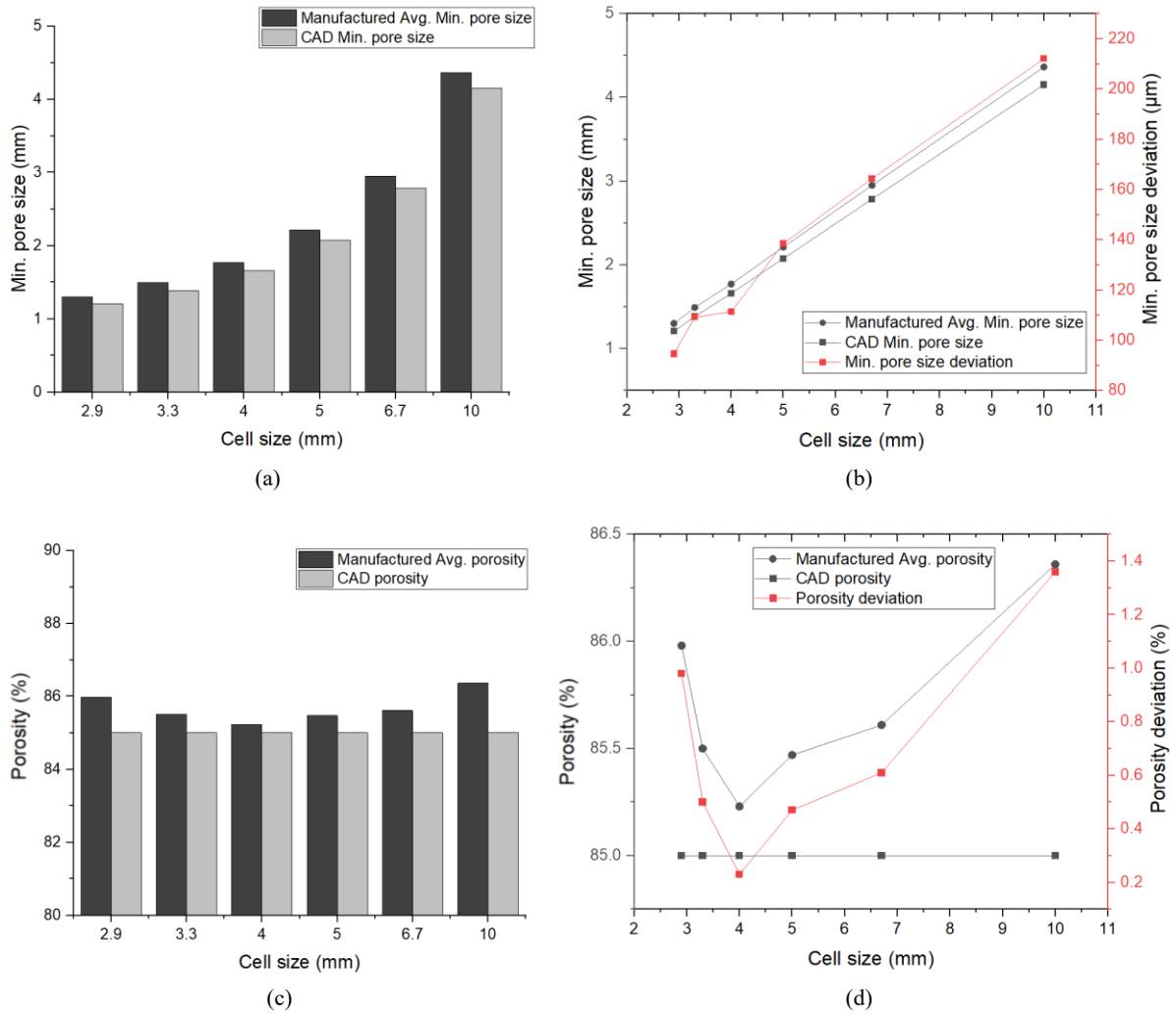

Figure 2.11: CAD to manufactured comparison of Min. pore size and porosity parameters: (a&c) CAD and manufactured results; (b&d) CAD to manufactured deviations.

2.3.2. PTPMS lattice porosity study (Run 2)

Figure 2.12 illustrates the printed PTPMS lattices with porosities from 45% to 90% at a constant cell size of 4 mm. The various lattice geometrical parameters were measured and reported, as seen in Table 2.8. Figure 2.13 shows the influence of increasing the PTPMS lattice porosity (at a constant cell size) on the OS wall thickness, SA:Vol ratio, and Min. pore size. Starting with the OS wall thickness, it can be observed that increasing the lattice porosity shows a decrease in the manufactured OS wall thickness Figure 2.13 (d), where a porosity increase from 45 to 90% is followed by a reduction in the OS wall thickness from 1.427 to 0.133 mm with a calculated total

thickness reduction of 1.294 mm. Moreover, the total thickness reduction is consistent with the CAD values seen in Table 2.4 & Figure 2.13 (a), where a total CAD thickness reduction of 1.38 mm is calculated. As such, it can be established that the average wall thickness decreases with increasing the lattice porosity. This lattice thickness behavior is expected as increasing the porosity at a constant cell size results in a decrease in the lattice volume fraction (i.e., a decrease in the lattice thickness).

On the other hand, the SA:Vol ratio showed an opposite trend to the wall thickness, where increasing the lattice porosity from 45 to 90% resulted in an increase in the manufactured SA:Vol ratio from 2.31 to 11.65 mm^{-1} with a total increase of 9.32 mm^{-1} as seen in Figure 2.13 (e). Furthermore, this increase is found to be consistent with the CAD values, where increasing the lattice porosity from 45 to 90% showed a corresponding increase in the CAD SA:Vol ratio of 9.96 mm^{-1}. The increase in the SA:Vol ratio is attributed mainly to the decrease in volume as the porosity is increased, where increasing the porosity from 45 to 90% resulted in a volume decrease from 935.97 to 180.72 mm^3. Although the surface area is observed to be increasing with higher porosities; however, the increase is minor and is not as significant as the volume (i.e., the surface area influence on the SA:Vol ratio is negligible).

Figure 2.13 (c & f) shows the porosity increase influence on the min. pore size. It can be observed that increasing the porosity in the specified range (i.e., 45 to 90%) resulted in an increase in the min. pore size, where at 45% and 90% porosity levels, the resulting manufactured min. pore size is found to be 0.480 mm and 1.873 mm, respectively. The same trend is observed with the CAD values seen in Table 2.4 & Figure 2.13 (c) with a min. pore size increase from 0.361 to 1.775 mm. As a result, it can be established that the overall lattice pore size is directly proportional to increasing the porosity.

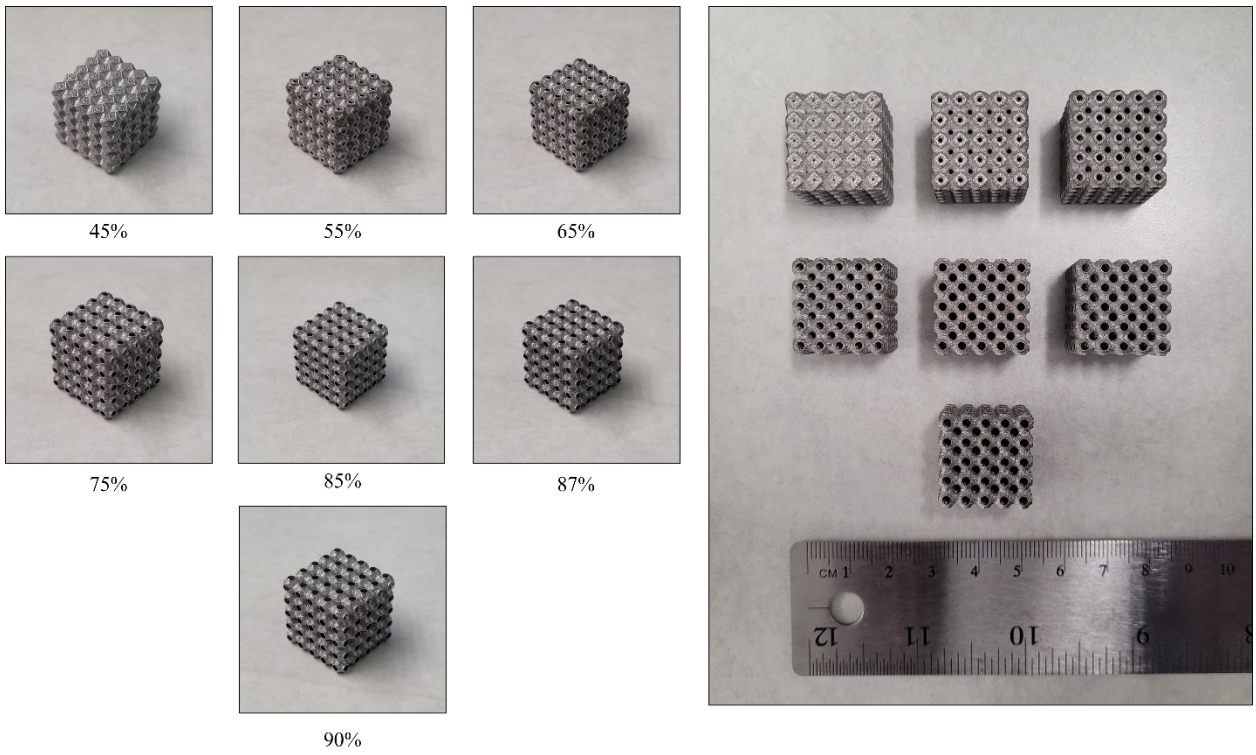

Figure 2.12: Varying porosity printed PTMPS lattices at a constant cell size.

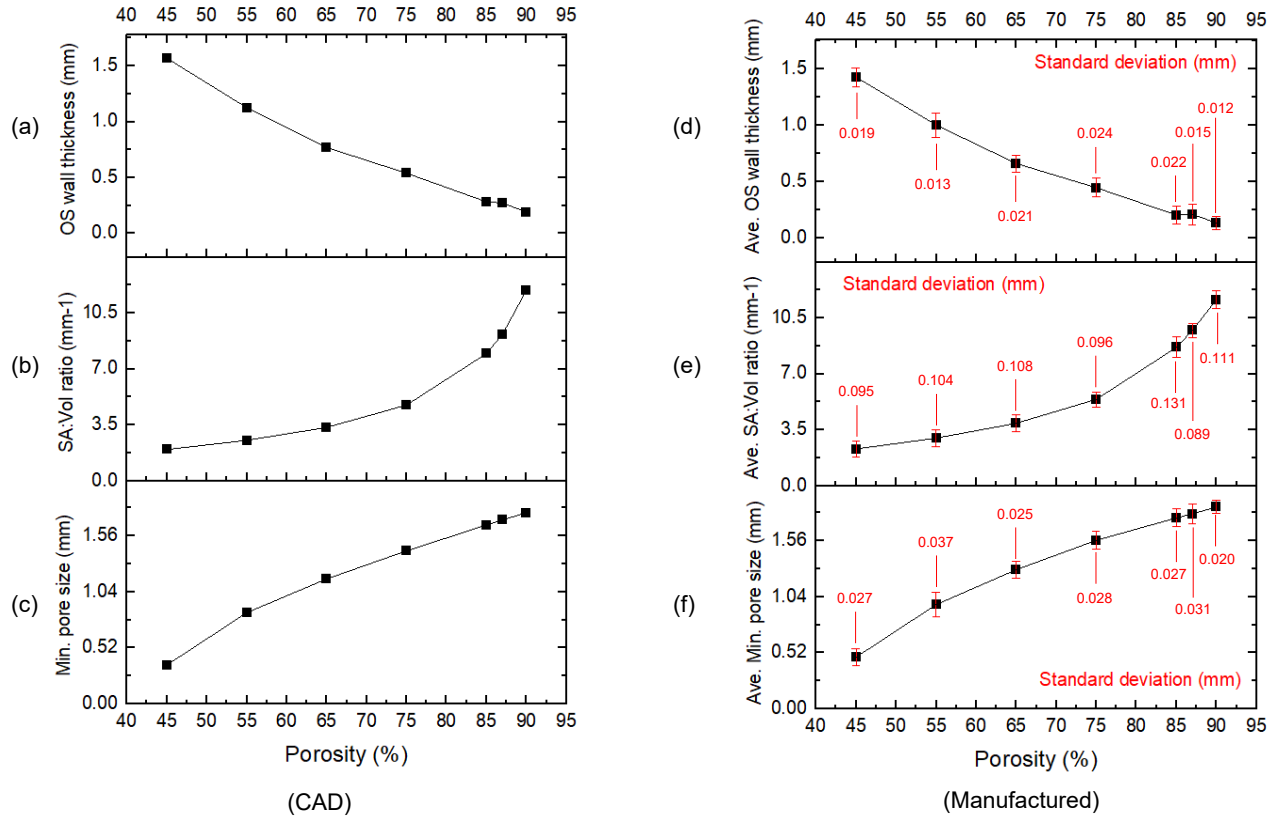

Figure 2.13: Porosity effect on PTPMS parameters: (a-c) CAD values; (d-f) manufactured values.

- **CAD to manufactured parameter deviation**

Table 2.9 shows the CAD to manufactured parameter deviations with increasing the porosity in the selected range (45-90%). The same equation (2.3) used previously is applied to calculate the different deviation values. Figure 2.14 (a) illustrates the CAD and manufactured OS wall thickness results. The same behavior with increasing the lattice cell size (Run 1) is observed here as well, where irrespective of the lattice porosity, the manufactured OS wall thickness consistently showed lower values than CAD, which indicates an occurring shrinkage in all printed samples, as previously discussed. Figure 2.14 (b) illustrates the CAD to manufactured OS wall thickness deviations with increasing the lattice porosity. It can be observed that increasing the lattice porosity shows lower wall thickness deviations (i.e., better thickness accuracy), where both 90% and 45% porosities showed minor and highest deviations of -57.078 μm and -143.480 μm, respectively. Moreover, this observation indicates that increasing the lattice porosity (at a fixed cell and sample sizes) results in a decrease in sample shrinkage during the printing process. Hence, further shrinkage investigation is required. Using GOM inspect 2021 software (ZEISS Group, Germany), the same lattice CAD to manufactured volume deviation color map study seen in Run 1 is conducted here as well, where samples with 45, 75, and 90% porosities are selected as seen in Figure 2.15 It can be evident that the 45% porosity sample Figure 2.15 (a) exhibited the largest shrinkage with an average shrinkage value of 0.82 mm, followed by the 75% sample Figure 2.15 (b) with 0.43 mm, then the 90% sample Figure 2.15 (c) with the smallest average shrinkage of 0.18 mm. Therefore, it can be stated that increasing the PTPMS lattice porosity results in a decrease in the overall shrinkage, which can be attributed to the decrease in the lattice material. Hence, fewer conduction paths are present, resulting in less shrinkage rates as previously discussed.

Figure 2.14 (c) shows the CAD and manufactured SA:Vol ratio results, a similar behavior observed in Run 1 is seen here, where samples with porosities in the range of 45 to 87% showed higher manufactured SA:Vol ratio values than CAD which is attributed to the increase in the surface area as illustrated previously. However, the 90% porosity sample showed a higher CAD SA:Vol ratio than manufactured. Thus, its inner morphology was investigated, and severe gaps were observed (Figure 2.16), where at higher porosities such as 90%, very thin lattice wall thicknesses are present, as indicated by the average wall thickness of 117 μm (Table 2.4) resulting in various gaps within the lattice structure which ultimately lead to surface area reductions. Hence, the resulting less manufactured SA:Vol ratio value than CAD. Figure 2.14 (d) illustrates the CAD to manufactured SA:Vol ratio deviation values with respect to increasing the lattice porosity. It can be observed that increasing the lattice porosity from 45% to 85% shows higher SA:Vol ratio deviations from 0.34 mm^{-1} to 0.70 mm^{-1}, respectively. However, a deviation decrease is noticed as the porosity is increased from 85% to 90%, which is attributed to the formation of gaps within the lattice. Hence, a minimum overall average wall thickness of 0.175 mm seen in Table 2.4, is necessary to prevent the formation of gaps within the lattice structure.

Table 2.8: Varying the PTPMS lattice porosity at constant cell size.

Cell size (mm)	Number of cells	CAD				Manufactured							
		Porosity %	Min. pore size (mm)	SA:Vol (mm-1)	OS wall thickness (mm)	Average Porosity %	Porosity standard deviation %	Average Min. pore size (mm)	Min. pore size standard deviation (mm)	Average SA:Vol (mm-1)	SA:Vol standard deviation (mm-1)	Average OS wall thickness (mm)	OS wall thickness standard deviation (mm)
4	5	45	0.361	1.97	1.570	45.79	0.107	0.48	0.027	2.31	0.095	1.427	0.019
4	5	55	0.847	2.54	1.127	55.8	0.096	0.969	0.037	2.99	0.104	1.002	0.013
4	5	65	1.160	3.35	0.770	66.12	0.129	1.292	0.025	3.92	0.108	0.661	0.021
4	5	75	1.421	4.75	0.539	76.45	0.109	1.565	0.028	5.41	0.096	0.447	0.024
4	5	85	1.661	7.97	0.283	85.23	0.097	1.772	0.027	8.67	0.131	0.204	0.022
4	5	87	1.707	9.18	0.271	87.18	0.088	1.811	0.031	9.73	0.089	0.21	0.015
4	5	90	1.775	11.93	0.190	89.53	0.110	1.873	0.020	11.65	0.111	0.133	0.012

Table 2.9: CAD to manufactured parameter deviations.

Cell size (mm)	Number of cells	CAD				Manufactured				CAD to manufactured deviation			
		OS wall thickness (mm)	SA:Vol (mm-1)	Min. pore size (mm)	Porosity %	Average OS wall thickness (mm)	Average SA:Vol (mm-1)	Average Min. pore size (mm)	Average Porosity %	OS wall thickness deviation (µm)	SA:Vol ratio deviation (mm-1)	Min. pore size deviation (µm)	Porosity deviation %
4	5	1.570	1.97	0.361	45	1.427	2.31	0.48	45.79	-143.480	0.34	118.588	0.79
4	5	1.127	2.54	0.847	55	1.002	2.99	0.969	55.8	-125.191	0.45	122.120	0.90
4	5	0.770	3.35	1.160	65	0.661	3.92	1.292	66.12	-108.960	0.57	132.258	1.12
4	5	0.539	4.75	1.421	75	0.447	5.41	1.565	76.45	-92.451	0.66	143.530	1.45
4	5	0.283	7.97	1.661	85	0.204	8.67	1.772	85.23	-78.593	0.70	111.430	0.23
4	5	0.271	9.18	1.707	87	0.21	9.73	1.811	87.18	-67.876	0.54	103.961	0.18
4	5	0.190	11.93	1.775	90	0.133	11.65	1.873	89.53	-57.078	-0.29	98.232	-0.47

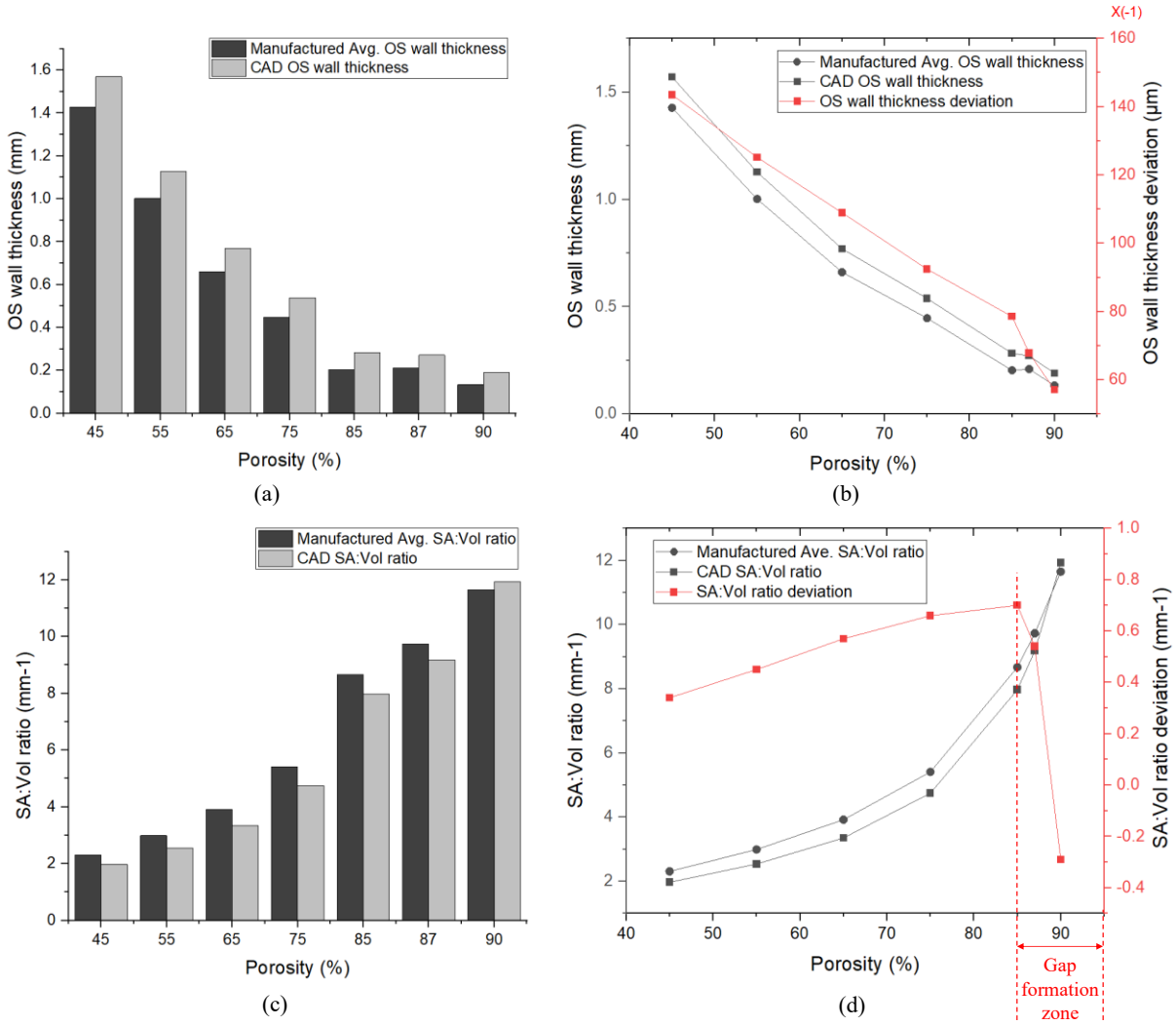

Figure 2.14: CAD to manufactured comparison of OS wall thickness and SA:Vol ratio parameters: (a&c) CAD and manufactured results; (b&d) CAD to manufactured deviations.

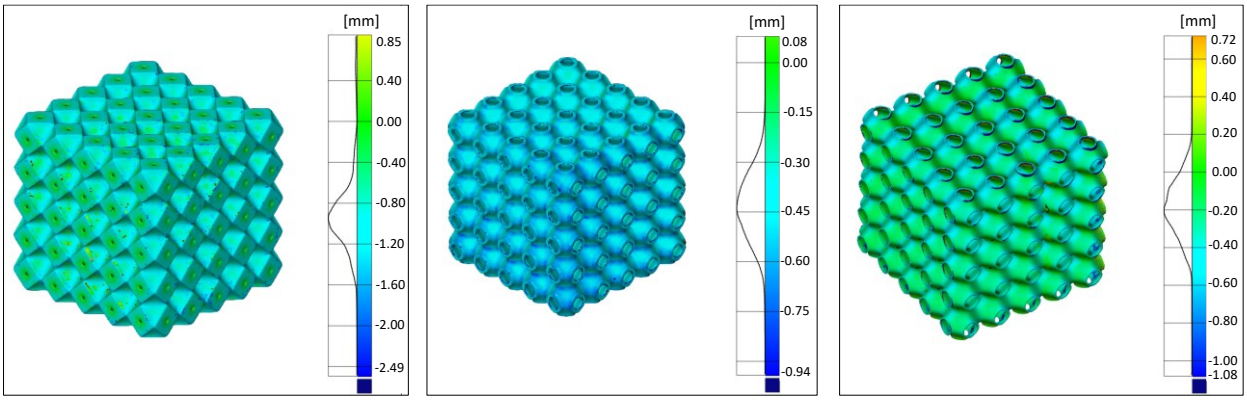

Figure 2.15: CAD to manufactured Volume deviation color map of PTPMS lattices: (a) 45% porosity; (b) 75% porosity; (c) 90% porosity.

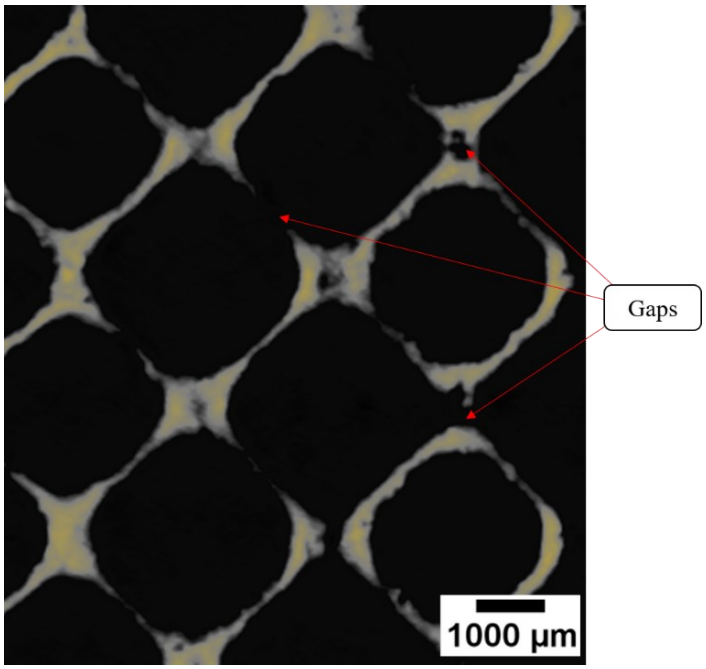

Figure 2.16: Inner morphology CT cross-section image of a 90% porosity PTPMS lattice structure.

Figure 2.17 shows the influence of increasing the lattice porosity on the min. pore size and overall manufactured porosity. Regarding the min. pore size, it is evident that irrespective of the lattice porosity, the manufactured min. pore size is consistently higher than the CAD values Figure 2.17 (a). Moreover, a similar pore size trend was seen in (Run 1) with increasing the lattice cell size, which was attributed to shrinkage. Figure 2.17 (b) illustrates the CAD to manufactured min. pore size deviations with increasing the lattice porosity. One significant distinction between increasing the lattice cell size (Run 1) and increasing the lattice porosity (Run 2) is that increasing the lattice cell size showed a decrease in the lattice surface area but an increase in the wall thickness; however, increasing the lattice porosity is observed to increase the lattice surface area but decrease the overall wall thickness. Although shrinkage is observed to be reduced with increasing the lattice porosity; however, higher CAD to manufactured pore size deviations from 118.588 um to 143.530 um were observed with increasing the porosity from 45% to 75%. This indicates that at lower porosities (i.e., lower than 75%), the pore size CAD to manufactured deviation is more sensitive

to the increase in the lattice surface area and increases with increasing the porosity. However, it is observed that as the porosity increases from 75% to 90%, the CAD to manufactured pore size deviation decreases from 143.530 um to 98.232 um. This can be attributed to the significant decrease in shrinkage (i.e., a significant decrease in the overall wall thickness), which results in lower CAD to manufactured pore size deviations. Figure 2.17 (c) & (d) show the manufactured porosities and their deviations from the CAD values, respectively. It can be observed that the porosity behavior follows the trends seen with the pore size, where the manufactured porosity is consistently higher than CAD (except for the 90% lattice sample), and an increase in the porosity CAD to manufactured deviation is seen with lower porosities (45% to 75%) followed by a deviation decrease as the porosity increases from 75% to 90%. Moreover, it was observed that the 90% porosity sample showed a manufactured porosity reduction with a value of 89.53%. Although it was established before that gaps are present within the 90% lattice structure and hence an increase in the porosity is expected; however, this lower porosity value is attributed to having very thin lattice wall thicknesses as indicated by the average wall thickness of 117 μm which challenges the printer's capabilities and leads to larger printed wall thicknesses. Hence, the average wall thickness of 0.152 mm can be identified as the average wall thickness limit that can be printed having the specified process parameters seen in Table 2.2. This is consistent with the typical feature size limit of 0.100-0.200 mm in LPBF systems having laser spot sizes of 50-100 μm [57]. Moreover, Similar observations were found by Yan [47], who studied the manufacturability of high porosity gyroid TPMS lattices with 94%, 92%, 90%, and 88% porosities. He found a slight decrease in the experimental porosities compared to the CAD values and attributed this behavior to the nonuniform increase in the lattice strut size within the lattice structure.

Depending on the heat transfer application of the cellular-walled pipe heat sink system, the findings in (Run 2) study indicate that at a selected fixed cell size, certain considerations should be regarded. If it is desirable to enhance the lattice heat conduction performance, a decrease in the lattice porosity to ensure wider conduction pathways should be considered; however, lowering the lattice porosity showed an increase in the lattice shrinkage rates which resulted in higher CAD to manufactured thickness deviations (i.e., lower volume fractions in the printed samples than CAD). Thus, a shrinkage compensation approach should be considered. Alternatively, if it is desirable to enhance the lattice heat convective performance, increasing the lattice porosity (i.e., increasing the SA:Vol ratio to ensure a higher surface area for enhanced lattice-flow interaction) should be considered; however, ensuring a porosity level that is not too high (i.e., having an average wall thickness less than 0.175 mm) to cause severe gaps is of significant importance.

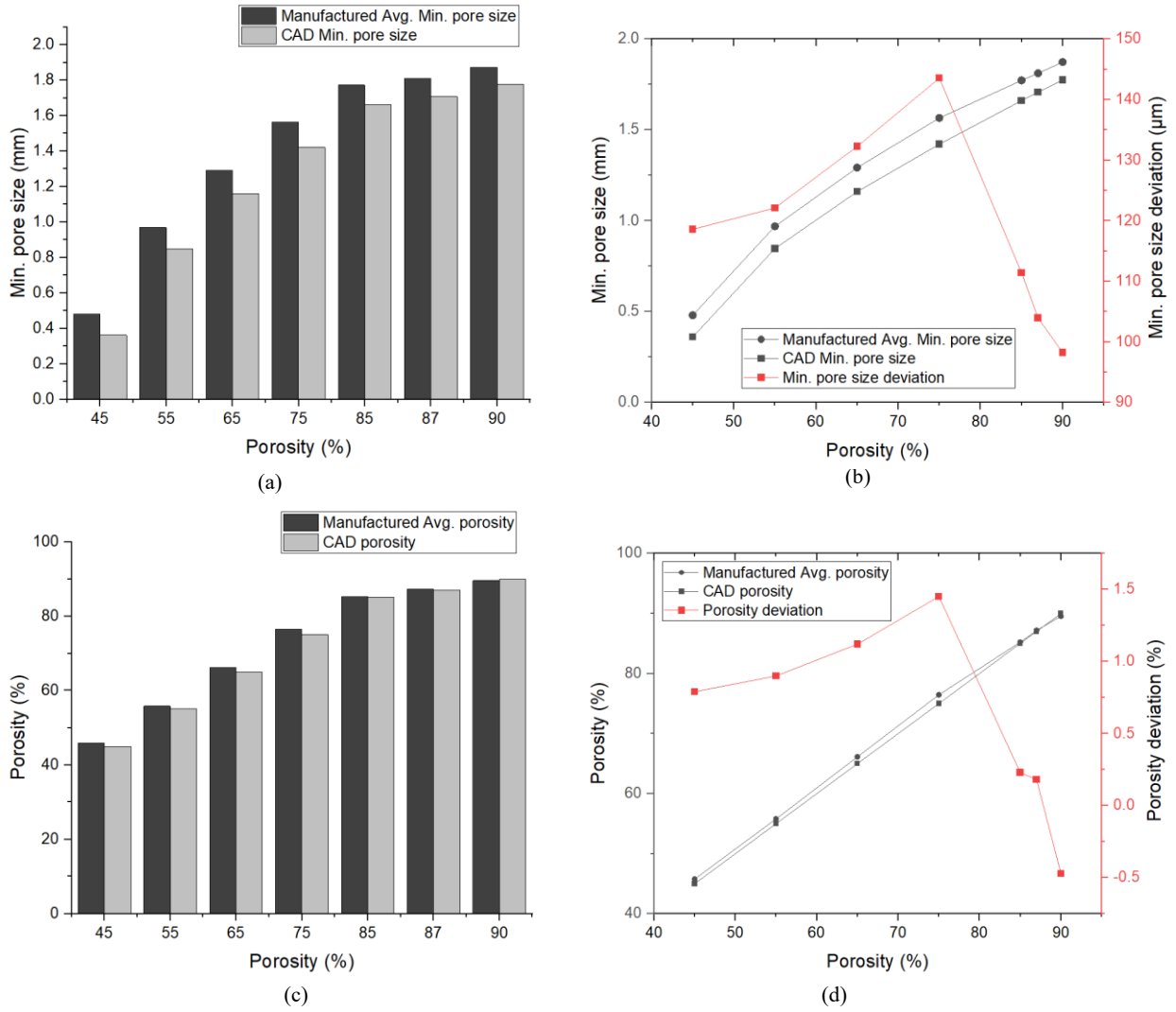

Figure 2.17: CAD to manufactured comparison of Min. pore size and porosity parameters: (a&c) CAD and manufactured results; (b&d) CAD to manufactured deviations.

2.3.3. Smallest PTPMS pore size study (Run 3)

Figure 2.18 shows the resulting PTPMS samples at varying min. pore sizes (0.257 – 0.482 mm). The printed samples were examined, and results were reported (Table 2.10). It is observed that samples with CAD min. pore sizes from 0.317 to 0.482 mm were successfully printed, indicating the printer's ability to print pore sizes down to 317 microns. However, the 45% lattice with a min. pore size of 0.257 mm is observed to be severely deformed and the pore is almost closed. Further investigation is carried out for the 45% and 46% lattices, as seen in Figure 2.19. It is evident from

the inner morphologies of both samples that the 45% sample with a min. pore size of 0.257 mm was not successfully printed. Thus, it can be established that the smallest pore size that can be printed using the ORLAS Coherent 250W with the optimized parameters seen in Table 2.2 is 0.317 mm.

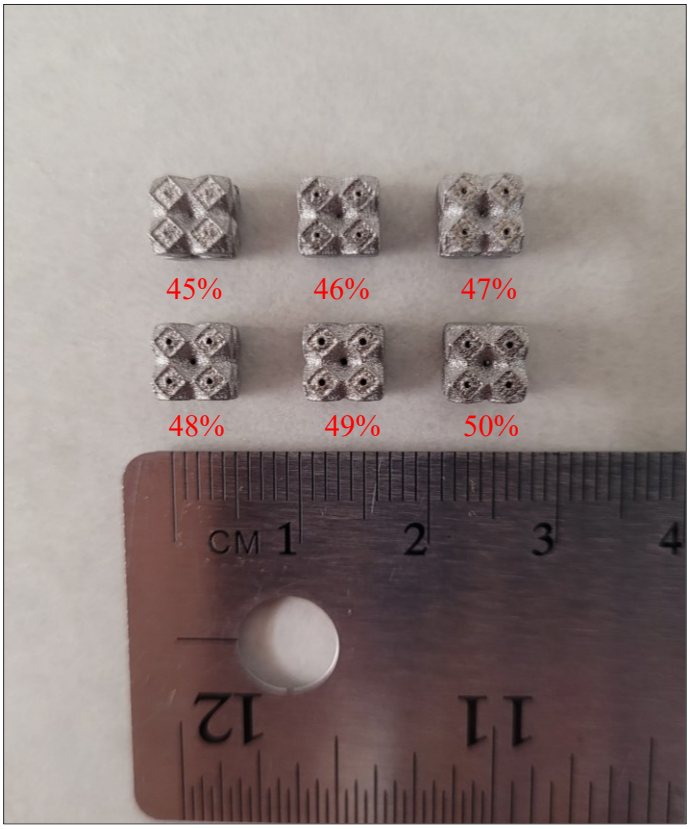

Figure 2.18: PTPMS printed lattices at varying pore sizes.

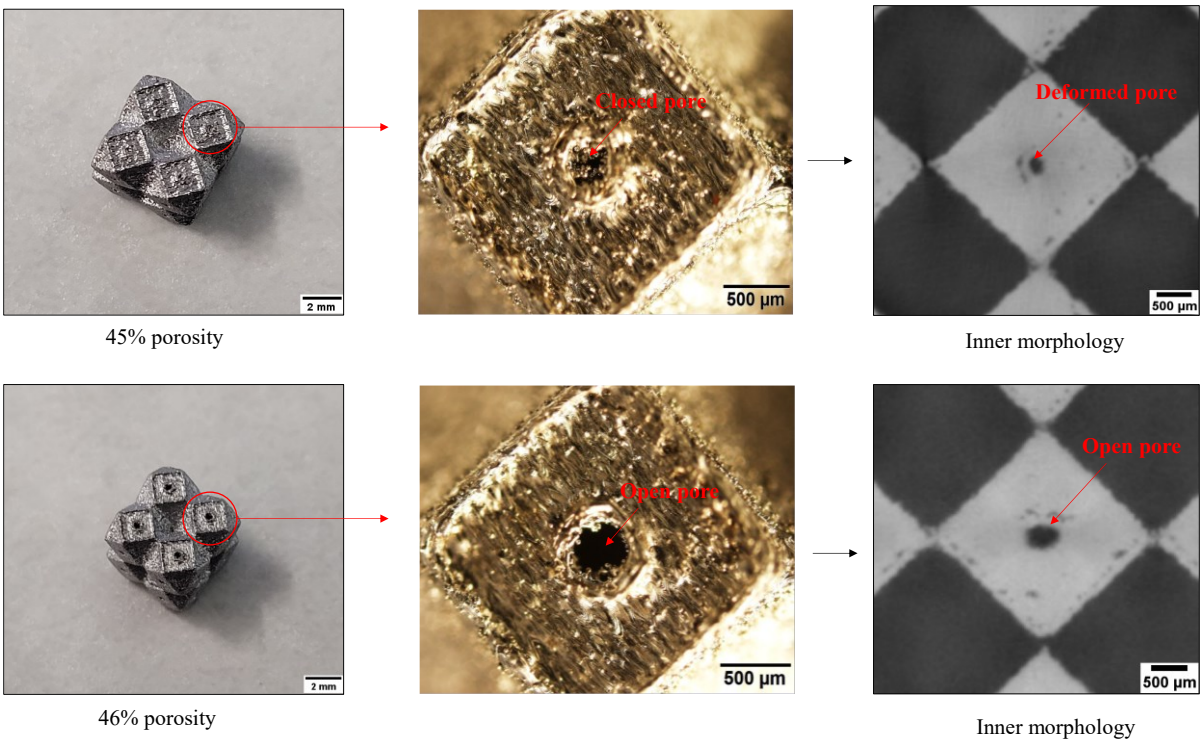

Figure 2.19: Pore examination of 45% and 46% lattices.

Table 2.10: PTPMS lattice results at varying min. pore sizes.

Run 3	Sample Dimensions (mm)	Cell size (mm)	Number of cells	Porosity %	CAD Min. Pore size (mm)	Manufactured Min. Pore size	
						Average (mm)	Standard deviation (mm)
1	6 x 6 x 6	3	2	45	0.257	Closed	-
2		3	2	46	0.317	0.464	0.026
3		3	2	47	0.359	0.509	0.021
4		3	2	48	0.400	0.553	0.030
5		3	2	49	0.441	0.564	0.022
6		3	2	50	0.482	0.582	0.019

Chapter 3: -Process Parameter Optimization of 2507 Super Duplex Stainless Steel Additively Manufactured by Laser Powder Bed Fusion Technique

3.1. Introduction

Laser powder bed fusion (LPBF) is an additive manufacturing technique in which a laser energy source is used to melt successive powder layers generating three-dimensional parts based on computer-aided design (CAD) models [45] – a review of the technology has been reported in [58]. The advances in the technology end-use parts with enhanced material quality, density, and consequently improved mechanical properties have grown significantly in recent years. Moreover, due to field applications such as medical, oil, and aerospace, which require manufactured parts with high quality and reliability, the LPBF process optimization has been significantly investigated with success [59–62].

It has been reported that more than 100 parameters play role in the LPBF manufactured part quality [63–65]. However, it was found that the laser power (p), scan speed (v), hatch distance (h), and layer thickness (t) had the most prominent effect on the microstructure and mechanical properties of the printed parts [66]. The term volumetric energy density (E_D) is a factor that is commonly used to guide the LPBF printing process optimization [67], and can be calculated using Equation (3.1). This factor relates the different printing parameters together and indicates the amount of energy input to the powder material during the printing process.

$$E_D = \frac{p}{v \,.\, h \,.\, t} \tag{3.1}$$

LPBF technology has some advantages over conventional manufacturing methods, including design freedom, manufacturing of complex part designs, reduced part weight, production of nearly net-shaped parts, and decreasing waste material [68]. However, one major drawback of LPBF is

the formation of pores (i.e., porosity) in the final printed parts, which can lead to compromised mechanical properties [69]. Several pore formation mechanisms have been reported in LPBF, with keyhole mode pores, metallurgical or gas pores, and lack-of-fusion pores being the three most prevalent types associated with the printing process parameters [70]. Keyhole mode pores form when the energy density (E_D) is too high (i.e., due to high laser power, slow scan speed, or low hatch distance), causing rapid metal vaporization at the meltpool surface resulting in a metal vapor recoil pressure that pushes the meltpool surface downwards and closes in on itself creating a cavity filled with metal vapor and shielding gas, referred to as keyhole or vapor depression [71]. The resulting keyhole pores are usually rounded but not completely spherical. Lack-of-fusion pores form when the energy density is too low, causing an insufficient melting of the powder, which results in large pores with irregular shapes and sizes, and often containing unmelted trapped powder particles [72]. Metallurgical or gas pores are mostly spherical and relatively small in size and are observed in the intermediate regime of energy density. These pores form due to the shielding gas entrapment, porosity of feedstock powder particles, or alloy vapors within the molten pool [58].

There are some studies that have used high-resolution microcomputed X-ray tomography (μCT) imaging to investigate the keyhole and lack-of-fusion pores under a range of identified printing process parameters [73,74]. As such, μCT imaging is adopted in this study for the porosity characterization and quantification analysis. The use of laboratory X-ray tomography for an in-depth examination of additively manufactured parts, along with several efforts to image various porosity types is reviewed in [49]. Moreover, the use of real-time fast microcomputed X-ray imaging has successfully been used in porosity formation analysis. This includes studies on the keyhole pore formation and particle spatter in meltpool dynamics [75], the dynamics of defects

and meltpool showing the mechanisms of pore formation [76], and the keyhole vapor depression formation threshold [77], amongst others. Furthermore, a distinct reported observation is that the vapor depression threshold is lower than expected and is present across the entire range of typical LPBF energy densities; however, the formation of keyhole porosity is only present in cases where the vapor depression is deep and unstable [77,78].

There is a wide range of materials that have an optimized process parameter set (i.e., can be successfully printed) in commercial LPBF systems, including titanium (Ti) alloys [79], aluminum (Al) alloys [80–82], cobalt (Co) alloys [83], nickel (Ni) alloys [84,85], and stainless steels [86,87]. Among the stainless steels, duplex stainless steels (DSSs) are known for their excellent combination of corrosion resistance and mechanical properties in different environmental conditions and are widely used in petrochemical, marine, nuclear, and chemical applications [88]. DSSs microstructure has two phases, namely ferrite (α) and austenite (γ) phases. Furthermore, it is important to maintain a roughly equal amount of ferrite and austenite phases (i.e., 1:1 ratio) to ensure high strength and enhanced corrosion resistance.

Recently, 2507 super duplex stainless steel (2507 SDSS) has gained considerable attention due to its high tensile and fatigue strength, good toughness, excellent pitting corrosion resistance, high weldability and formability, and high stress corrosion cracking resistance in chloride and sulfide environments, which is the reason for its wide adaption in heat exchangers, desalination plants, and pressure vessels and boilers industry systems [89]. In recent years, the adoption of LPBF in processing 2507 SDSS powder to manufacture highly dense parts with enhanced qualities has been investigated with success. Davidson et al. [90] studied the laser power influence on the resulting part quality and microstructure of 2507 SDSS. The scan speed, hatch distance, and layer thickness were kept constant at 590 mm/s, 120 μm, and 50 μm, respectively, while the laser power varied

from 50 to 400 W resulting in an energy density range from 14.1 to 113 J/mm^3. The resulting samples showed randomly distributed pores which were attributed to both insufficient melting at lower laser powers (i.e., lack of fusion pores) and entrapped gases at higher energy densities (i.e., keyhole pores). The highest reported sample density was 90.8% at an energy density of 70.62 J/mm^3 and the as-built sample microstructures were mainly ferritic with small amounts of austenite precipitates along the grain boundaries. Saeidi et al. [91] succeeded in manufacturing 2507 DSS samples with a relative density of 99.5% using a laser power of 190 W, scan speed of 750 mm/s, hatch distance of 100 µm, and a layer thickness of 20 µm with a reported energy density of 126.67 J/mm^3. Kunz et al. [92] investigated the properties of 2507 SDSS manufactured by LPBF and reported a relative density of 99.6% using a laser power, scan speed, hatch distance, and layer thickness of 160 W, 1333.33 mm/s, 100 µm, and 50 µm, respectively with a calculated energy density of 24 J/mm^3.

Considering the literature studies on 2507 SDSS, a full analysis of the laser power, scan speed, and hatch distance influence and their interactions during the manufacturing process on the resulting part quality and microstructure is not yet reported, which signifies clear research gaps. Furthermore, the current research studies on 2507 SDSS show a wide optimized energy density range from 24 to 126.67 J/mm^3 with fluctuating laser power, scan speed, and hatch distance parameter sets ranging from (160 to 250) W, (590 to 1333.33) mm/s, and (100 to 120) µm, respectively [90–92]. As a result, it is challenging to decide which parameter set is the most reliable, and a need for a thorough 2507 SDSS parameter investigation is highlighted. In this study, the authors adopted the response surface method (RSM) to investigate the influence of laser power, scan speed, and hatch distance on the resulting sample quality and find an optimized parameter set capable of producing almost fully dense parts.

Statistical techniques, such as the RSM and analysis of variance (ANOVA), have been previously adopted and proven to be useful in the process parameter optimization of LPBF technology [93–95]. Wang et al. [93] investigated the LPBF process parameter effect on the sample microstructure and mechanical properties of a nickel-based superalloy using the RSM approach. They succeeded in increasing the resulting sample tensile strength by applying the RSM approach to optimize the process parameters. Terner et al. [94] successfully optimized the laser power and scan speed process parameters to manufacture high-density CoCr-Mo alloy samples using RSM. Deng et al. [95] succeeded in manufacturing 316L samples with high density and low surface roughness by applying the RSM approach.

In summary, this paper investigates the influence of laser power, scan speed, and hatch distance on the resulting 2507 SDSS sample porosity (i.e., sample quality) fabricated by LPBF. High-resolution microcomputed X-ray tomography (μCT) and optical microscope (OM) images were utilized to assess the resulting sample porosity and investigate the various pore formation types along the entire energy density range. The RSM approach is adopted to investigate the influence of each parameter and find a set of optimized printing parameters capable of manufacturing 2507 SDSS samples with minimum porosity (i.e., high density). Moreover, the microstructure and tensile properties of 2507 SDSS printed samples using the optimized process parameters are investigated as well. The findings of this study can be used as a stand-alone guide in selecting optimum printing process parameters to manufacture low porosity, high mechanical properties, and reliable 2507 SDSS samples using LPBF technique.

3.2. Materials and Methods

3.2.1. Material and equipment

The SDSS 2507 powder produced by gas atomization is supplied by Sandvik Osprey (Neath, UK). The powder's chemical composition is shown in Table 3.1. The morphology of the powder particles significantly affects the fluidity and melting behavior of the powder in LPBF process; parameters such as powder particle shape and size distribution influence the manufactured sample quality [96]. The Morphologi G3 shape image analyzer provided by Malvern Panalytical (Malvern, UK) is used in the characterization process of 2507 SDSS powder particles Figure 3.1. Based on 113626 counted particles, results showed that the particles are mostly spherical with a circularity mean of 0.954 ± 0.059 Figure 3.1 (b), where a circularity value of 1 depicts a complete spherical particle shape. The reported circularity standard deviation of 0.059 % is only applicable to the lower bound; however, the upper bound should be capped at 1. The particle size distribution is shown in Figure 3.1 (c), with a mean particle diameter of 28.63 ± 9.04 μm.

All samples were manufactured using the ORLAS Coherent 250W LPBF printer (California, USA). The ORLAS 250W printer uses an FLS 150 fiber laser with a wavelength of 1070 nm, a beam diameter of 40 μm, a laser power of up to 250 W, and a scanning speed of up to 3000 mm/s. The printing process of all samples was conducted in an argon environment with a constant oxygen level of 0.01%, and the scanning direction change between successive layers was kept at 45°.

Table 3.1: 2507 SDSS chemical composition.

Element	Fe	Cr	Ni	Mo	Mn	N	Si	Cu	C	P	S
Content (wt%)	Balance	24.6-25.4	6.8-7.2	3.76-4.24	0.7-1.1	0.26-0.31	0.2-0.6	0.20	0.02	0.025	0.008

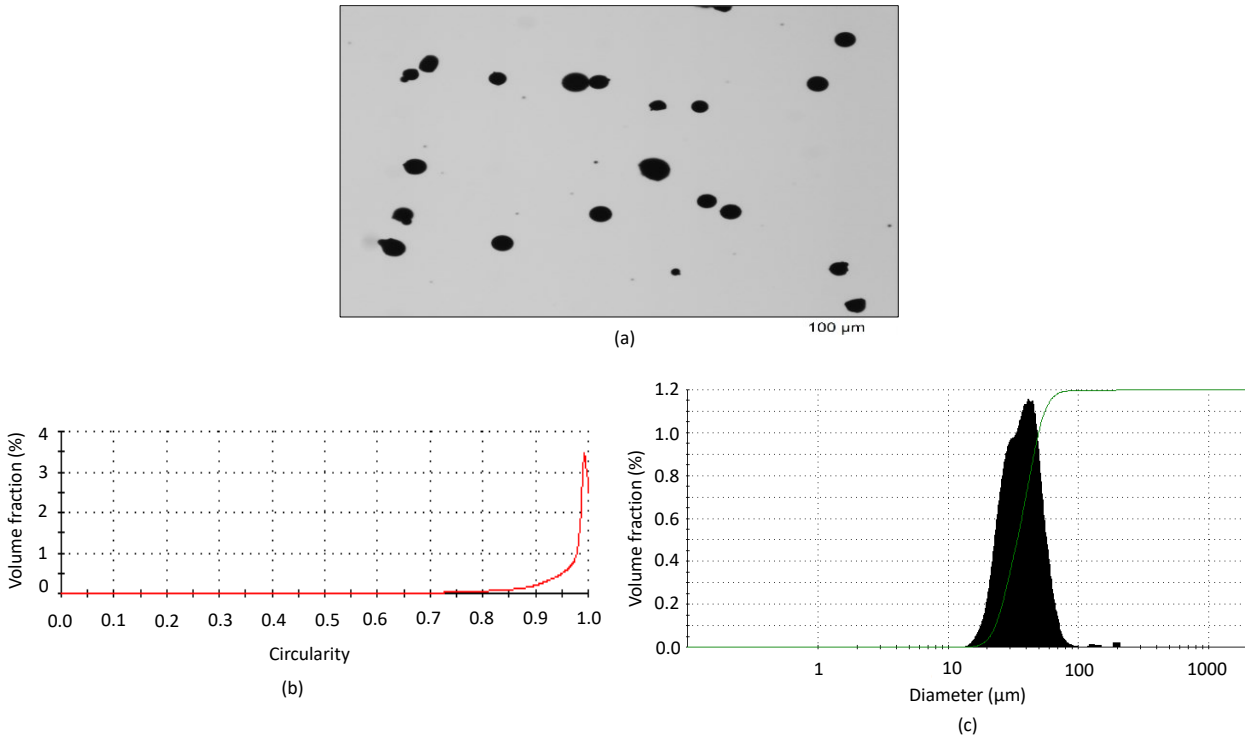

Figure 3.1: 2507 SDSS powder morphology: (a) Microscopic image of 2507 SDSS powder particles; (b) Powder particle circularity; (c) particle size distribution.

3.2.2. Response surface methodology

RSM is a statistical approach that uses a design of experiment (DoE) for developing metrology, fitting a regression model between input and output parameters, and optimizing the process outcomes [97]. The term "DoE" refers to a group of methods (full factorial, central composite, box-Behnken, etc.) for generating a set of trials whose outcomes are dependent on the input factors. In this study, three factors are optimized, namely; laser power (p), scan speed (v), and hatch distance (h), while the layer thickness (t) is kept constant at 25 µm. The layer thickness (t) is usually overlooked in the optimization process and kept constant; However, enhanced qualities are observed with thin layer thicknesses [98], hence a layer thickness of 25 µm was selected.

The selected DoE type determines the number of trials, combinations, replication, and randomization of the factors to investigate the cause-and-effect relationships between inputs and outputs with a certain level of confidence. Considering a full factorial DoE for three factors with

five levels, the number of trials is 5^3 = 125. However, manufacturing and measuring 125 trials (i.e., cubes) is not practical in terms of cost and time. The number of trials can be reduced to 20 using the central composite design (CCD) seen in Fig. (2). The CCD is a sufficient five-level fractional factorial DoE with center and star points used to fit quadratic models. In a three-factor CCD, the model is composed of 8 factorial points (blue circles), a center point (red circle), and 6 star points which are at a distance (α) from the center point and are set to a default value of 1.6818 to ensure design rotatability as shown in Figure 3.2 (top view). The range of the factorial points (1,-1) for all three factors is identified based on the previous 2507 SDSS studies [91–93] then the center and star points are calculated and reported, as seen in Table 3.2. The star points establish new low and high extreme values for all three factors. In this study, the center point was replicated six times to investigate the location effect on print quality. Minitab 19 software (Pennsylvania, USA) was utilized to generate the various run sets seen in Table 3.3 based on the CCD template shown in Figure 3.2. A total of 20 cubes with dimensions of (5×5×5) mm were designed, and each cube was assigned different printing parameters following the order seen in Table 3.3.

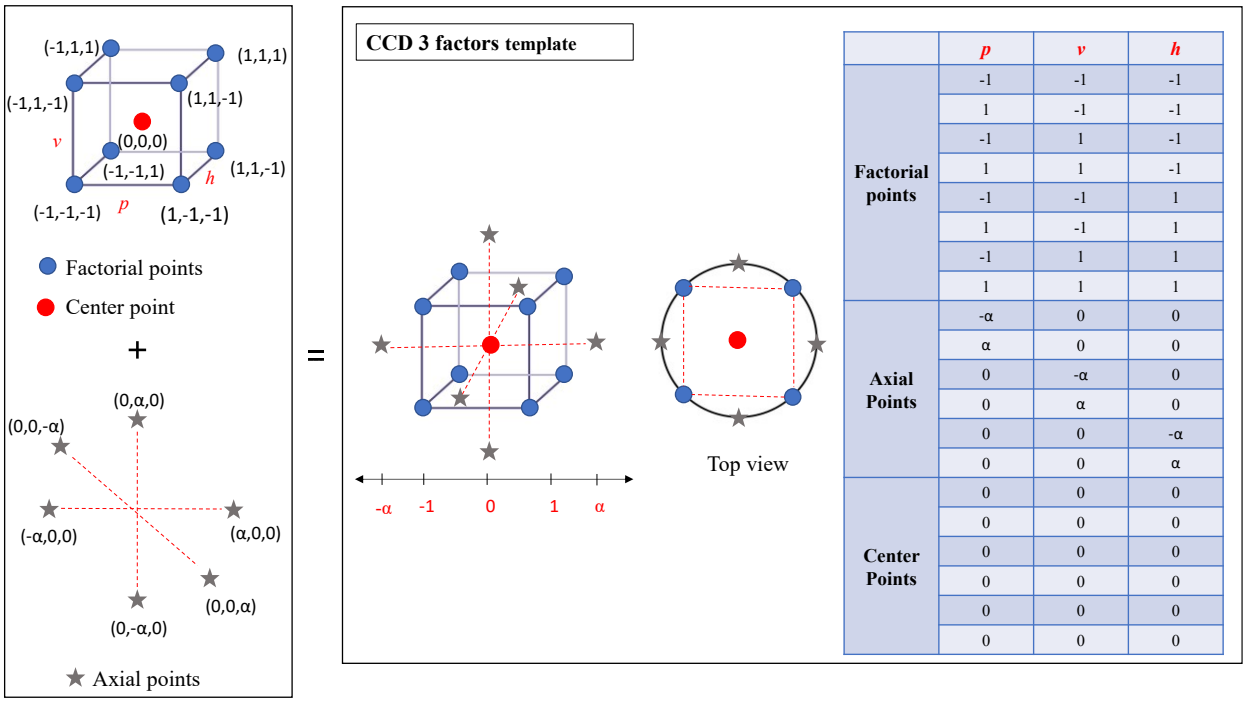

	p	v	h
Factorial points	-1	-1	-1
	1	-1	-1
	-1	1	-1
	1	1	-1
	-1	-1	1
	1	-1	1
	-1	1	1
	1	1	1
Axial Points	-α	0	0
	α	0	0
	0	-α	0
	0	α	0
	0	0	-α
	0	0	α
Center Points	0	0	0
	0	0	0
	0	0	0
	0	0	0
	0	0	0
	0	0	0

Figure 3.2: Schematic representation of a three-factor CCD.

Table 3.2: CCD factor levels and values.

Levels	Laser power (W)	Scan speed (mm/s)	Hatch distance (µm)
Lowest (- α)	69.3	159.1	26.1
Lower (-1)	100	500	50
Center point (0)	145	1000	85
Higher (1)	190	1500	120
Highest (α)	220.7	1840.9	143.9
Range	69.3 – 220.7	159.1 – 1840.9	26.1 – 143.9

Table 3.3: CCD design set up for all factors.

Run	Laser Power (W)	Scan speed (mm/s)	Hatch distance (µm)
1	100	500	50
2	220.7	1000	85
3	145	1000	85
4	145	1000	85
5	190	1500	50
6	145	1000	85
7	145	1000	143.9
8	100	1500	50
9	69.3	1000	85
10	145	1000	85
11	190	500	120
12	190	1500	120
13	145	1000	85
14	190	500	50
15	145	1840.9	85
16	100	1500	120
17	100	500	120
18	145	1000	26.1
19	145	159.1	85
20	145	1000	85

Following the manufacturing process, the output (i.e., porosity) of all 20 manufactured samples is measured and analyzed; then, a polynomial quadratic regression model is fitted for each output using Minitab 19. The generalized quadratic regression model is defined as follows [97]:

$$Y = b_0 + \sum_{i=1}^{n} b_i x_i + \sum_{i=1}^{n} b_{ii} {x_i}^2 + \sum_{i<j}^{n} b_{ij} x_i x_j + e \qquad (3.2)$$

where Y is the predicted response, x_i and x_j are the input factors; b_0 is the intercept term, b_i is the linear term coefficient, b_{ii} is the squared term coefficient, b_{ij} is the interaction term coefficient, and e is the observed experimental error. The polynomial quadratic regression model is widely adopted as it considers non-linear effects and investigates the factor interaction influence on the predicted response. Following the acquisition of the polynomial regression model, adequacy and accuracy checking analysis is carried out to ensure that the fitted model is satisficing the regression assumptions and provides tolerable approximations of the response; then, analysis of variance

(ANOVA) is utilized along with surface and contour plots to study the influence of input factors on the resulted porosity. Finally, the input factors are optimized using the regression model to produce minimum Y values (i.e., minimum porosity); a flow diagram summary of the RSM is seen in Figure 3.3.

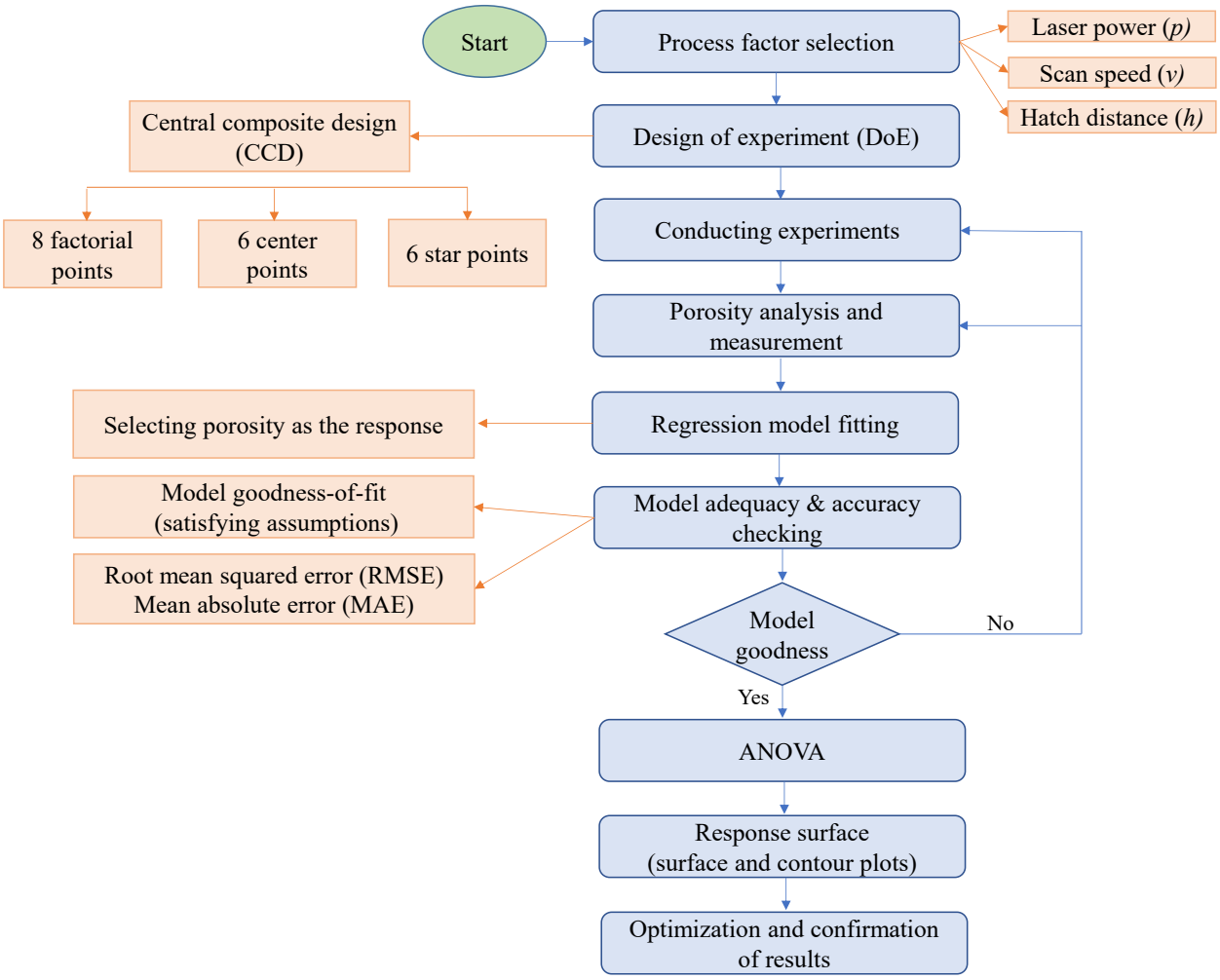

Figure 3.3: RSM flow diagram.

3.2.3. Mechanical testing

Tensile strength analysis was conducted on manufactured tensile samples using the optimized parameter set that resulted from the RSM. A total of three cylindrical tensile samples were manufactured by the ORLAS Coherent 250W LPBF printer. The tensile specimens were designed according to the ASTM A370 / ASME SA-370 standard with a total length of 80 mm and a testing diameter of 6.36 mm, as shown in Figure 3.4. The tensile testing was performed in a universal testing machine at room temperature (25 °C), with a strain rate of 10^{-3} s^{-1}.

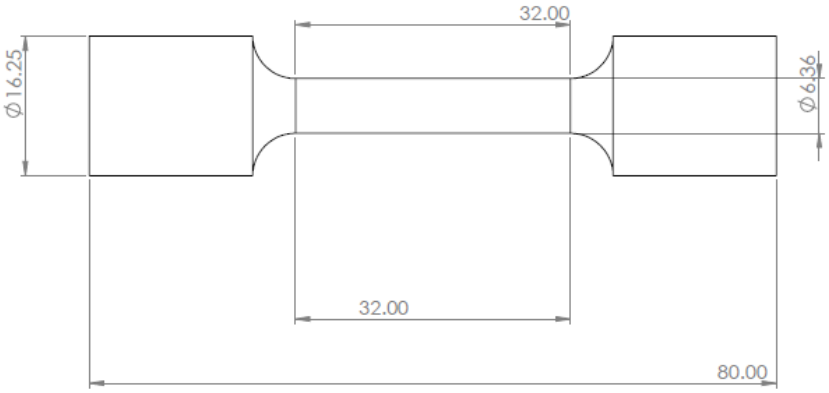

Figure 3.4: Tensile sample geometry dimensions.

3.2.4. Characterization Methods

High-resolution microcomputed X-ray tomography was utilized in the porosity characterization process. Using the ZEISS Xradia 620 Versa X-ray μCT (Oberkochen, Germany) with a voltage of 140 kV, a power of 21.01 W, and an exposure time of 3 s, micro CT reconstructed images were generated which revealed the inner porosity profile of the LPBF manufactured samples. Then, porosity characterization and quantification analysis were conducted using Dragonfly 21 software (Montreal, Canada). Dragonfly porosity analysis is based on color-segmenting each layer of the 3D CT reconstructed images to distinguish between the solid material (purple) and pores (green), as shown in Figure 3.5. The Olympus optical microscope (Tokyo, Japan) was utilized to capture

OM images for different pore types. The microscopy sample preparation included mounting, polishing, and chemical etching.

To observe the cross-section microstructure, samples were mounted and ground successively to 2000 grit, and then polished with diamond paste. After that, the polished specimens were etched in a 3 wt% Nital solution. Field Emission - Scanning Electron Microscope (FE-SEM), Zeiss Sigma (Gemie) was utilized for microstructural analysis. Furthermore, the XRD patterns were measured using a Rigaku UItima IV diffractometer (Co Ka radiation with a wavelength λ =1.78886 Å).

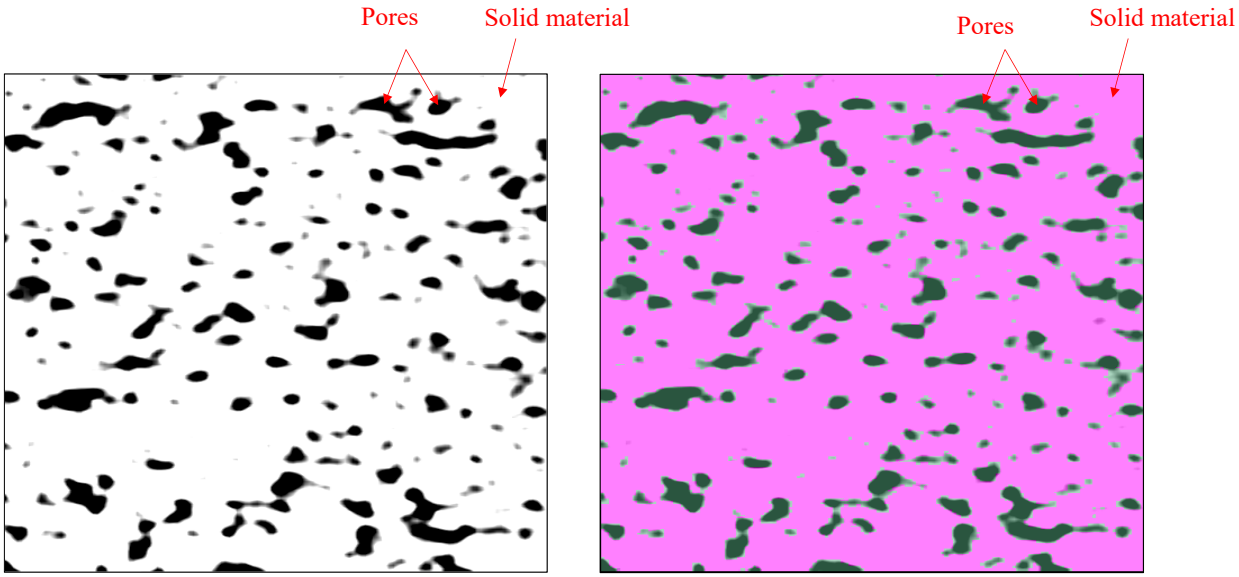

Figure 3.5: Dragonfly color segmentation process: (a) CT scanned image layer; (b) Color segmentation.

3.3. Results and discussions

3.3.1. Porosity characterization analysis

All 20 samples were successfully printed, as seen in Figure 3.6. The resulting porosities for all samples were measured and reported in Table 3.4. Figure 3.7 and Figure 3.8 show the various

porosity formation regimes with increasing energy density. At lower energy densities, the meltpool and scan track become shallow and thin, causing a lack of fusion between adjacent tracks and successive layers, which results in the formation of large and irregular pores (i.e., lack-of-fusion pores) seen in Figure 3.8 (a-c). It can be observed that increasing the energy density resulted in a sharp decrease in the lack-of-fusion pores, where increasing the energy density from 22.22 J/mm^3 to 68.24 J/mm^3 showed a porosity reduction from 45.60 % to 4.61 % (Figure 3.7 "Red dots"). Following the lack-of-fusion regime, a narrow optimal energy density range from 68.24 J/mm^3 to 126.67 J/mm^3 (Figure 3.7 "green diamonds") is observed in terms of porosity reduction with a porosity range from 0.33% to 0.04%. This intermediate regime is observed to have pores that are relatively small Figure 3.8 (d&e), which are presumably attributed to trapped gas between powder particles (i.e., metallurgical pores). A gradual increase in the porosity is observed following the intermediate regime, with a porosity increase from 0.15% to 1.56% (Figure 3.7 "blue triangles"). The gradual increase in porosity is attributed to keyhole mode porosity seen in Figure 3.8 (f-h), which are present due to high energy densities that cause deep meltpools with strong dynamics resulting in entrapped pore vapors as the meltpool propagates.

Examining the replicated center point samples (i.e., samples 3, 4, 6, 10, 13, and 20 based on Table 3.3) having a constant laser energy density of 68.24 J/mm^3, it is evident from porosity readings that the sample location influences the resulting porosity. Although samples 3, 4, 6, and 10 showed relatively close porosity readings within the 0.33 % to 0.85 % range; However, samples 13 and 20 are observed to experience significant irregularity in porosity readings with 2.26 % and 3.01%, respectively. This can be attributed to positioning these samples farthest from the shielding gas and recoater sweep directions as seen in Figure 3.6, resulting in insufficient shielding gas and powder spread which can adversely affect the resulting sample density. Davidson and Ferrar et al.

[90,99] reported similar observations and attributed the behavior to the sample location from the sweep and shielding gas directions. One distinct note they reported is that the argon flow rate is higher at the plate's front and decreases along the back, which leads to insufficient condensate vapor removal, causing incident laser radiation absorption or laser beam scattering that results in surface semi-sintered particles. As such, it is always favorable to position the samples in the middle of the build plate whenever possible.

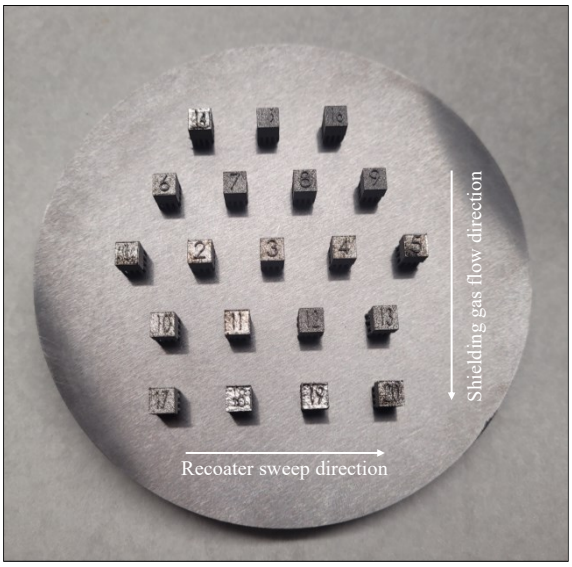

Figure 3.6: Successfully printed samples based on CCD and their positions on the substrate.

Table 3.4: Porosity results.

Run	Laser power (W)	Scan speed (mm/s)	Hatch distance (µm)	Layer thickness (µm)	Laser energy density (J/mm^3)	Experimental porosity (%)
1	100	500	50	25	160.00	0.36
2	220.7	1000	85	25	103.85	0.04
3	145	1000	85	25	68.24	0.69
4	145	1000	85	25	68.24	0.85
5	190	1500	50	25	101.33	0.13
6	145	1000	85	25	68.24	0.33
7	145	1000	143.9	25	40.32	14.92
8	100	1500	50	25	53.33	15.28
9	69.3	1000	85	25	32.62	41.74
10	145	1000	85	25	68.24	0.40
11	190	500	120	25	126.67	0.15
12	190	1500	120	25	42.22	29.60
13	145	1000	85	25	68.24	2.26
14	190	500	50	25	304.00	0.73
15	145	1840.9	85	25	37.07	17.80
16	100	1500	120	25	22.22	45.60
17	100	500	120	25	66.67	4.61
18	145	1000	26.1	25	221.91	0.66
19	145	159.1	85	25	428.87	1.56
20	145	1000	85	25	68.24	3.01

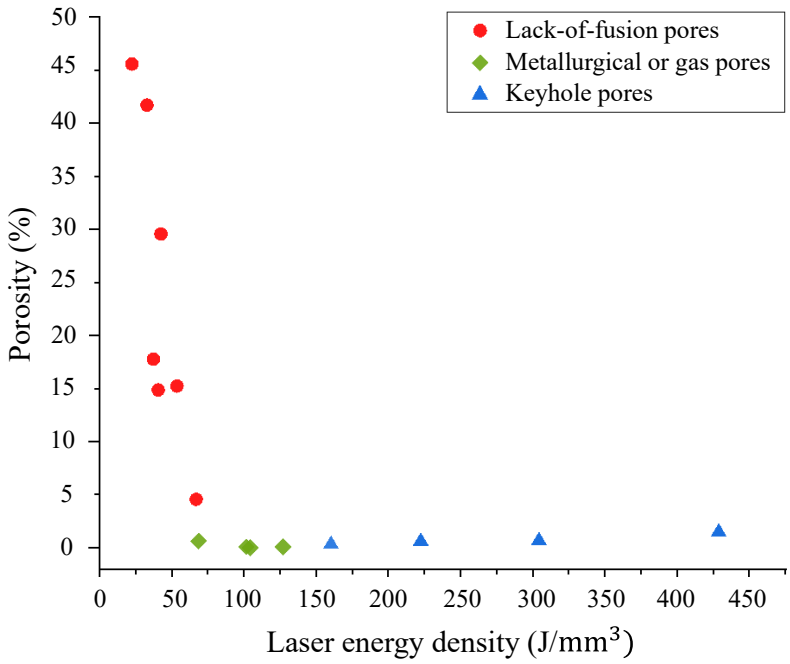

Figure 3.7: Porosity distribution with increasing energy density.

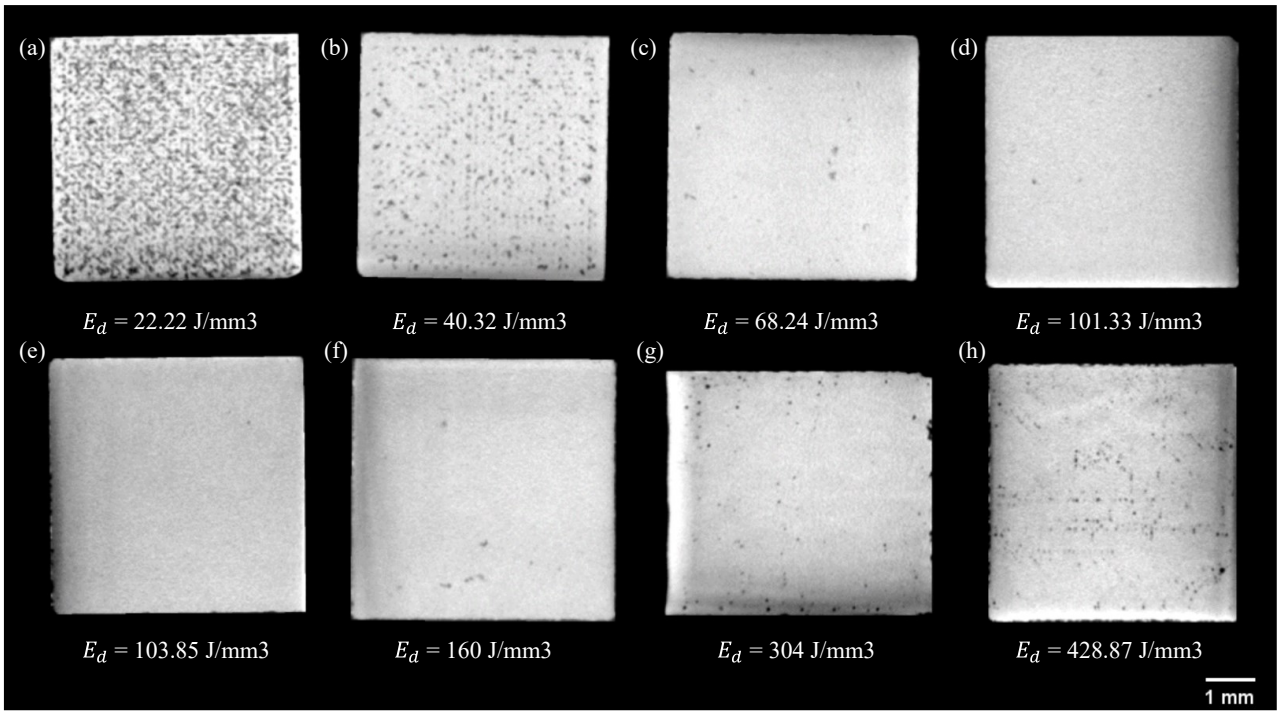

Figure 3.8: Cross-section CT images of sample series for increasing energy density.

Further quantitative porosity analysis is conducted for the lack-of-fusion, metallurgical or gas, and keyhole pore regimes based on samples 16, 2, and 19 with energy densities of 22.22 J/mm^3, 103.85 J/mm^3, and 428.87 J/mm^3, respectively. The pore size and shape for each regime are summarized in Table 3.5 in terms of feret diameter and aspect ratio, respectively. The aspect ratio is a value between (0 to 1) and provides insights into the pore shape where a low aspect ratio (less than 0.5) indicates a flat-like shape (i.e., irregular), and a high aspect ratio (higher than 0.5) is an indication of spherical pores. The lack-of-fusion pores are observed to be relatively large and have irregular shapes with a mean feret diameter and mean aspect ratio of 0.26 mm and 0.33, respectively. This is clearly seen in Figure 3.9 (a&d), with large irregular-shaped pores having trapped unmelted powder particles, hence the resulting high porosity of 45.6%. As the energy density increases from 22.22 to 103.85 J/mm^3, an optimal intermediate regime is observed having relatively small and spherical pores shown in Figure 3.9 (b&e) with a mean feret diameter and mean aspect ratio of 0.05 mm and 0.65, respectively. Following the intermediate regime and as the energy density

increases from 103.85 J/mm^3 to 428.84 J/mm^3, a gradual increase in pores is observed which is attributed to keyhole pores at higher energy densities. The pores are observed to be roundish and slightly larger than the metallurgical or gas pores (i.e., intermediate regime) shown in Figure 3.9 (c&f) with a mean feret diameter and aspect ratio of 0.09 mm and 0.57, respectively.

Table 3.5: Pore shape and size in terms of aspect ratio and feret diameter.

Sample	16			2			19		
Power (w)	100			220.7			145		
Scan speed (mm/s)	1500			1000			159.1		
Hatch distance (µm)	120			85			85		
Layer thickness (µm)	25								
Laser energy density (J/mm^3)	22.22			103.85			428.87		
Pore type	Lack of fusion			Metallurgical or gas			Keyhole		
Feret diameter (mm)	Min.	Max.	Mean	Min.	Max.	Mean	Min.	Max.	Mean
	0.12	0.77	0.26 ± 0.12	0.04	0.06	0.05 ± 0.01	0.04	0.13	0.09 ±0.02
Aspect ratio	Min.	Max.	Mean	Min.	Max.	Mean	Min.	Max.	Mean
	0.05	0.76	0.33 ± 0.14	0.59	1	0.65 ± 0.08	0.20	0.81	0.57±0.17
Porosity %	45.60			0.06			1.56		

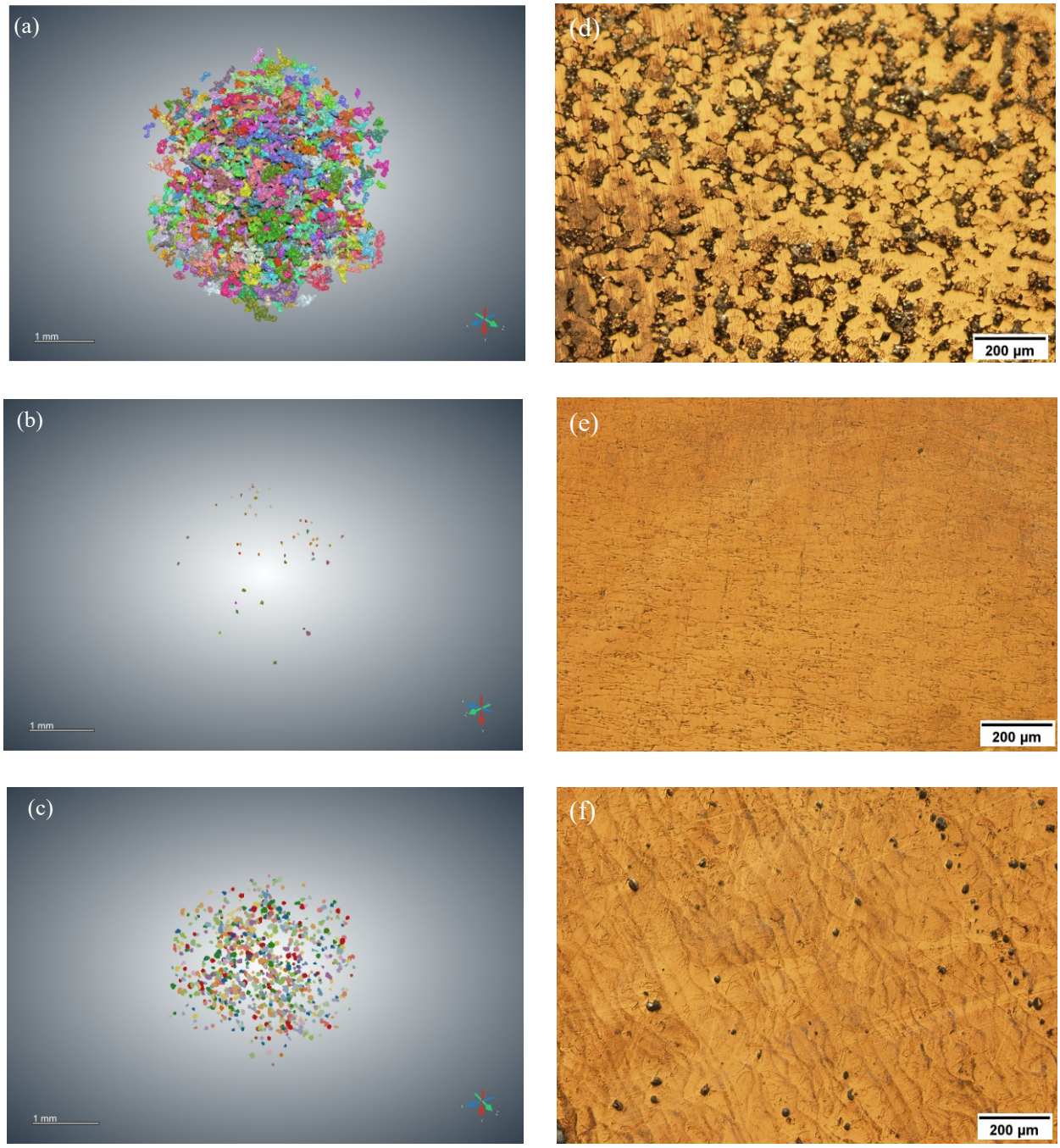

Figure 3.9: Lack-of-fusion (sample 16), metallurgical or gas (sample 2), and keyhole (sample 19) pores: (a-c) 3D representation; (d-f) OM images.

3.3.2. Response surface methodology analysis

3.3.2.1. Regression model equation

A quadratic regression model is developed which correlates the laser power (p), scan speed (v), and hatch distance (h) with the response (i.e., porosity) based on Equation (3.2). Using Minitab 19 software, the input factors (p, v, h) and experimental porosity results seen in Table 3.4 were used as the base for the fitted regression model. The multiple regression analysis techniques found in RSM are used to estimate the model's coefficients, and the response can be expressed by the following quadratic Equation:

$$\text{Porosity (\%)} = 88.5 - 0.901\,(p) - 0.0155\,(v) - 0.399\,(h) + 0.003166\,(p^2) + 0.00001\,(v^2) + 0.00145\,(h^2) - 0.00015\,(p.v) - 0.00046\,(p.h) + 0.000401\,(v.h) \quad (3.3)$$

3.3.2.2. Model adequacy & accuracy checking

Model adequacy and accuracy checking is essential to check the fitted model and ensure that it provides a fair approximation of the porosity response. Unless the regression model shows an adequate fit, the analysis or optimization of the fitted response may result in poor or inaccurate outcomes. The model adequacy is checked using the residuals, which result from the difference between the observed values and fitted values predicted by the regression model. The normal probability plot of the residuals seen in Figure 3.10 (a) is one way to check if the model satisfies the normality assumption. It can be observed that the normality assumption is valid and satisfied as the residuals are approximately distributed along a straight line. Figure 3.10 (b) shows the predicted values distribution versus the residuals. It is evident that the residuals are randomly distributed with no obvious trends, suggesting a constant variance between the residuals. Therefore, the model satisfies the constant variance assumption.

The regression model accuracy is evaluated using metrics such as the root mean squared error (RMSE) and mean absolute error (MAE), which are calculated according to Equations (3.4) and (3.5):

$$\text{RSME} = \left(\frac{1}{\text{n}}\sum_{i=1}^{n}(Y_{i\ actual} - Y_{i\ predicted})^2\right)^{0.5} \quad (3.4)$$

$$\text{MAE} = \frac{1}{\text{n}}\sum_{i=1}^{n}\left|Y_{i\ actual} - Y_{i\ predicted})\right| \quad (3.5)$$

Where n is the number of samples, $Y_{i\ actual}$ is the resulting experimental porosity, and $Y_{i\ predicted}$ is the predicted porosity using the regression model. The RSME and MAE results for the developed regression model are within the acceptable range with values of 4.735% and 3.917%, respectively. The model adequacy and accuracy results are satisfactory; therefore, it can be concluded that the regression model's fitting is sufficient to describe the porosity response.

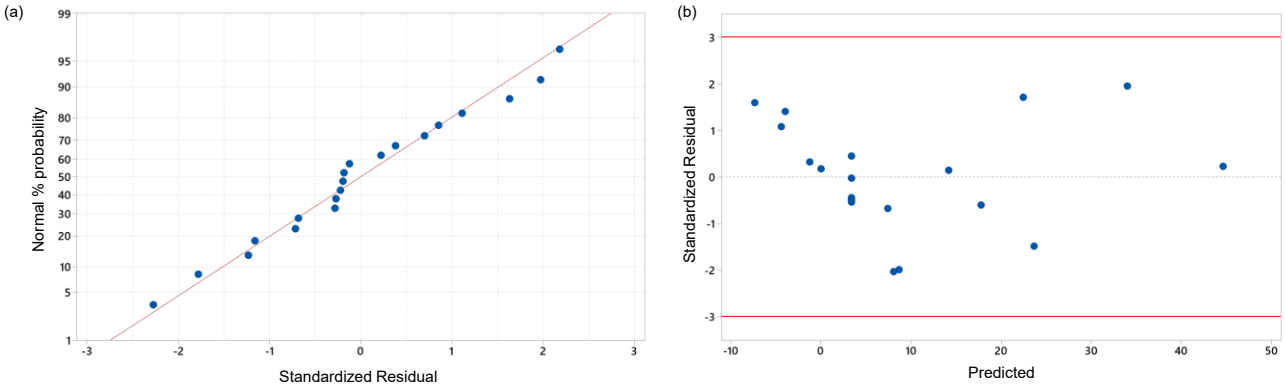

Figure 3.10: (a) Normal probability plot of the residuals; (b) Predicted values vs. residuals.

3.3.2.3. ANOVA and response surface analysis

The ANOVA analysis results seen in Table 3.6 indicate the statistical data of the regression model. The significance of each calculated regression coefficient is tested and evaluated. These tests indicate whether the terms significantly influence the response values. The P-value test results seen in Figure 3.11 show how significant the effect of each term is on the resulting porosity, where a calculated P-value of less than 0.05 is an indication that the term has a statistical significance of 95% confidence level. It is evident that the linear terms of laser power, scan speed, and hatch distance have a significant effect on the resulting porosity with P-values of 0.001, 0.001, and 0.004, respectively. The non-linear effect (i.e., squared term) is only observed to be significant for the laser power with a P-value of 0.003, whereas higher p-values of 0.173 and 0.311 are seen for the scan speed and hatch distance, respectively, indicating that the non-linear effect of these factors is not significant. This can be observed from the factor vs. porosity main effect plots seen in Figure 3.12 (a), where a strong parabolic trend is seen with the laser power than speed and hatch factors. Furthermore, the power vs. porosity plot additionally shows the sharp porosity decrease when increasing the power from 69.3 W to around 150 W, followed by a gradual increase in porosity for higher power values. Anton [78] reported a similar observation with increasing the laser power, where he stated a very sharp lack of fusion porosity drop at low laser power values followed by a gradual increase in keyhole porosity at higher power values. Moreover, the speed vs. porosity and hatch vs. porosity plots (Figure 3.12 (a)) indicate that increasing the scan speed and hatch distance results in higher porosity profiles.

Regarding the interaction term and as shown in Figure 3.11, the factor interaction between speed and hatch (BC) is observed to be significant with a P-value of 0.011, whereas interactions between power and speed (AB) and power and hatch (AC) are observed to be insignificant with P-values

of 0.163 and 0.755, respectively. This can be observed from the factor vs. porosity interaction plots shown in Figure 3.12 (b), where increasing the laser power seems to not influence the speed and hatch curves seen in the (power*speed) and (power*hatch) plots. However, as seen from the (speed*hatch) plot, increasing the speed is observed to influence the various hatch curves, which indicates a strong interaction effect between the speed and hatch factors.

Table 3.6: Model ANOVA results.

Source	DF	Adj SS	ADJ MS	F-Value	P-Value
Model	9	3438.74	382.082	9.53	0.001
Linear	3	2294.29	764.762	19.07	0.000
A-Power (W)	1	814.20	814.198	20.30	0.001
B-Speed (mm/s)	1	920.97	920.971	22.97	0.001
C-Hatch (µm)	1	559.12	559.118	13.94	0.004
Square	3	654.37	218.123	5.44	0.018
AA	1	592.51	592.508	14.78	0.003
BB	1	86.42	86.424	2.16	0.173
CC	1	45.62	45.622	1.14	0.311
2-Way interaction	3	490.08	163.360	4.07	0.039
AB	1	91.09	91.091	2.27	0.163
AC	1	4.14	4.143	0.10	0.755
BC	1	394.85	394.847	9.85	0.011
Error	10	401.02	40.102		
Lack-of-fit	5	375.03	75.006		
Pure Error	5	25.99	5.198		
Total	19	3839.76			

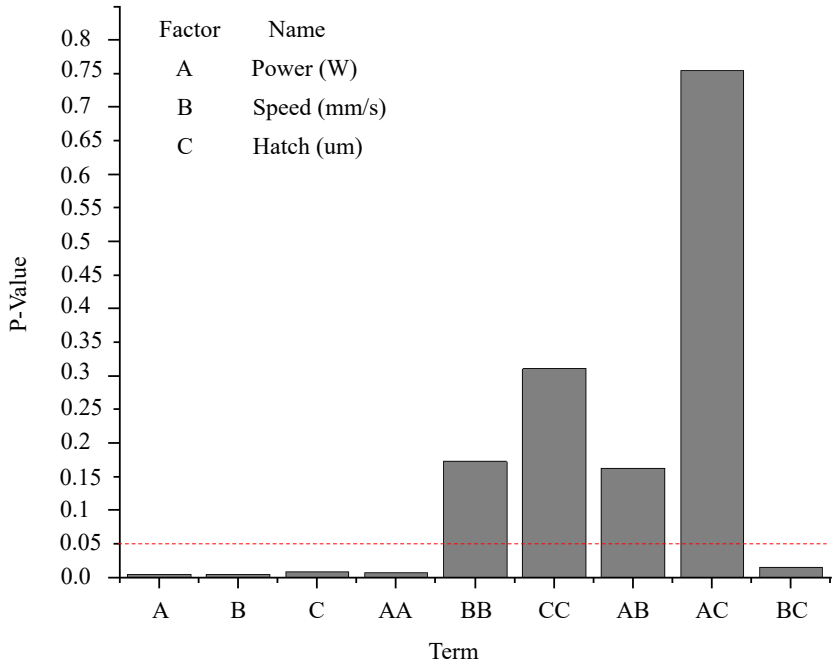

Figure 3.11: P-values of regression model terms.

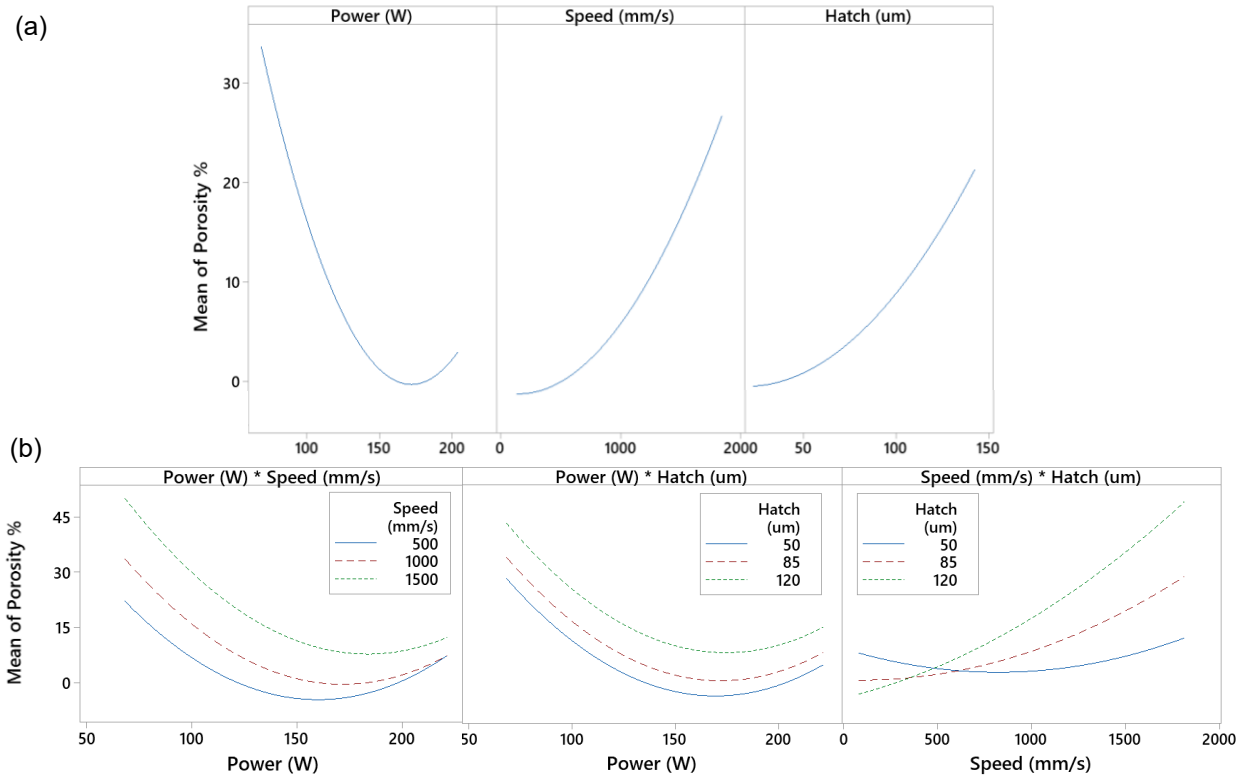

Figure 3.12: Factor vs. porosity plots: a) Main effects; b) Interaction.

Based on the regression model, three-dimensional (3D) surface graphs and equivalent contour plots seen in Figure 3.13 were generated to illustrate the influence of each process parameter (i.e., factors) on the resulting sample porosity. The influence of laser power and scan speed on the porosity is shown in Figure 3.13 (a&b) at a fixed hatch distance of 50 μm. It can be observed that higher porosities are seen with decreasing the laser power and increasing the scan speed. When the laser power goes to less than 80 W and the scan speed higher than 1400 mm/s, the porosity is observed to be higher than 35%. This can be attributed to the resulting low energy density with respectively lower and higher laser power and scan speed values leading to lack-of-fusion pores. Although increasing the laser power while decreasing the scan speed shows a reducing trend in the porosity; However, having extremely higher laser power and lower scan speed settings is observed to adversely influence the sample density with a porosity range from (1 to 10)%. This can be attributed to the resulting higher energy densities and the associated keyhole pores. This indicates that extremely low laser powers coupled with high scan speeds or extremely high laser powers coupled with low scan speeds should be avoided during the LPBF process to reduce the resulting print porosity (i.e., improve the sample density).

Figure 3.13 (c&d) shows the effect of laser power and hatch distance on the porosity at a fixed scan speed of 1000 mm/s. It is evident that a combination of low laser power and high hatch distance results in a significant increase in the resulting porosity. This can be observed when setting the laser power to less than 80 W and the hatch distance higher than 120 μm, which resulted in a porosity profile higher than 40%. This is attributed to having significantly low energy densities (less than 22.86 J/mm^3) leading to the prominent presence of lack-of-fusion pores, which indicates that lower laser power and higher hatch distance settings should be avoided. Generally, a high hatch distance must be avoided as it can cause insufficient laser overlap leading to poor melting of

the powder. This can be observed at the higher ends of the laser power and hatch distance porosity profiles in Figure 3.13 (c&d). Although the energy density is sufficient (E_D= 73.33 J/mm^3) having a laser power and hatch distance of 220 W and 120 µm, respectively; However, a high porosity profile (10 – 15%) is observed, which can be attributed to the formation of lack-of-fusion pores due to the poor melting resulting from insufficient laser overlap at high hatch distances.

Figure 3.13 (e&f) shows the effect of the scan speed and hatch distance on the resulting porosity at a fixed laser power of 170 W. It can be observed that higher scan speeds coupled with high hatch distances result in high porosity profiles. This is seen when setting the scan speed and hatch distance to 1800 mm/s and 140 µm, respectively, which resulted in a porosity profile higher than 40%. Although decreasing the scan speed and hatch distance results in a reduction in the porosity; However, setting extremely low scan speeds and hatching distances is observed to increase the porosity, which is attributed to the resulting high energy densities causing instabilities in the meltpool and the formation of keyhole pores. This indicates that extremely high scan speeds coupled with high hatch distances or extremely low scan speeds coupled with low hatch distances should be avoided to maintain low porosity profiles during the LPBF printing process.

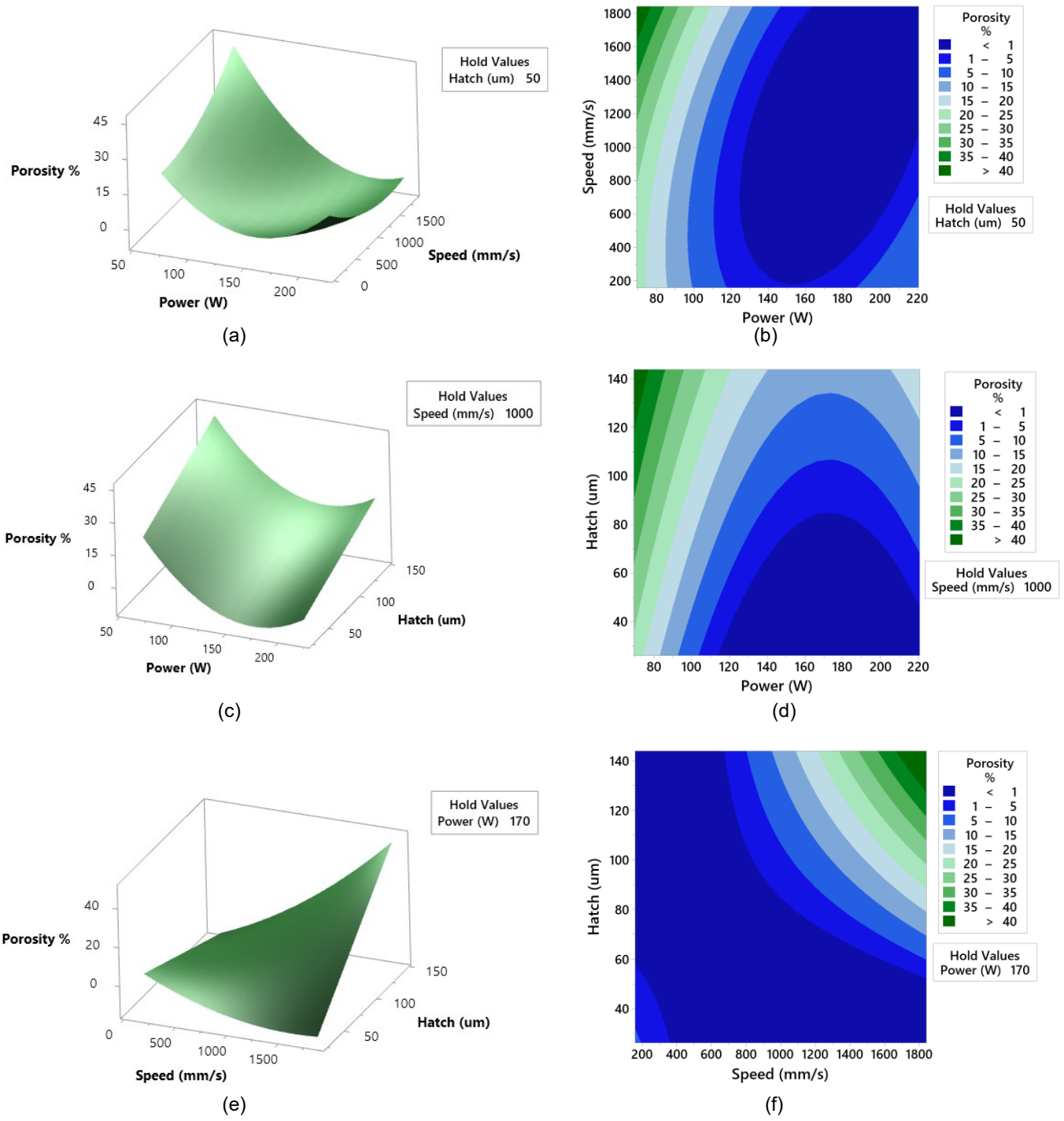

Figure 3.13: Laser power, scan speed, and hatch distance influence on the porosity: (a, c, e) surface plots; (b, d, f) counter plots.

3.3.2.4. Parameter optimization for porosity

The laser power, scan speed, and hatch distance parameters were optimized to achieve minimum porosity outcomes. In order to increase the model's prediction accuracy, the highest non-significant terms (AC and CC) were eliminated from the regression model, as seen in Eq (3.6):

$$\text{Porosity (\%)} = 82.5 - 0.915\,(p) - 0.0141\,(v) - 0.219\,(h) + 0.003079\,(p^2) + 0.000009\,(v^2) - 0.00015\,(p.v) + 0.000401\,(v.h) \quad (3.6)$$

Minitab 19 was utilized to generate three optimized parameter sets capable of producing samples with minimum porosities at an identified porosity range from 0 % to 1%, as seen in Table 3.7. All three optimized sets (1, 2, and 3) have a fixed layer thickness of 25 µm with a calculated energy density of 142.72 J/mm^3, 97.69 J/mm^3, and 87.16 J/mm^3, respectively. Three replicated samples were manufactured for each set at different locations (Figure 3.14) to validate each optimized parameter set. The samples were organized into columns (left, middle, and right) where each column has different position patterns (closest, middle, and farthest) from the shielding gas direction, as seen in Figure 3.14.

Table 3.8 shows the experimental porosity results based on the optimized combination of printing parameters. It can be observed that the three sets produced almost fully dense samples with relative densities higher than 99.837% (i.e., porosities less than 0.163%). Furthermore, the experimental porosity results agree well with the predicted values, with a maximum reported residual of 0.032, indicating the possibility of successfully predicting the porosity using the regression model. One distinct observation is that the first sample row closest to the shielding gas showed superior porosity results than the other replicates (Table 3.8, green highlighted), which indicates that the shielding gas direction effect is more significant than the sweep direction. Figure 3.15 shows cross-section CT images of the optimized first row samples. Sample 1 showed higher porosity results

than samples 2 and 3, which can be attributed to the relatively higher energy density of 142.72 J/mm^3 that resulted in the formation of keyhole pores seen in Figure 3.14 (a). Sample 2 (Figure 3.15 (b) & Figure 3.16) with a laser power, scan speed, and hatch distance of 217.4 W, 1735.7 mm/s, and 51.3 µm, respectively, showed optimal reduced porosity results of 0.011% (i.e., a relative density of 99.989%). As a result, set 2 was selected as the optimized printing parameters for 2507 SDSS and was adopted in printing the tensile samples for tensile strength property characterization.

Table 3.7: Optimized parameter sets for minimal porosity.

Set/Sample	Power (W)	Speed (mm/s)	Hatch (µm)	Predicted porosity (%)	Composite desirability
1	209.6	1022.9	57.4	0.141	1.000
2	217.4	1735.7	51.3	0.039	1.000
3	145	1000.0	87.16	0.047	0.999

Table 3.8: Optimized parameters experimental vs. predicted porosity results.

Set/Sample	Power (W)	Speed (mm/s)	Hatch (µm)	Experimental porosity				Predicted porosity	Residual
				Left	Mid	Right	Avg.		
1	209.6	1022.9	57.4	0.167	0.055	0.266	0.163	0.141	0.022
2	217.4	1735.7	51.3	0.029	0.030	0.011	0.023	0.039	-0.016
3	145	1000.0	87.16	0.040	0.139	0.058	0.079	0.047	0.032

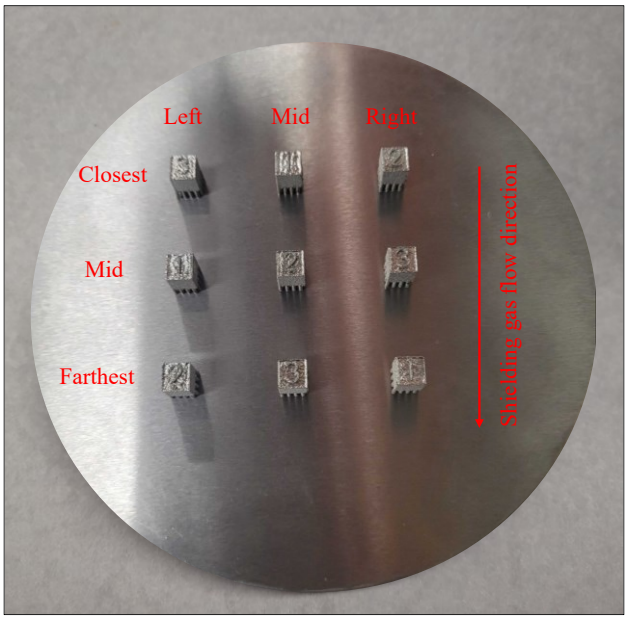

Figure 3.14: Manufactured optimized samples.

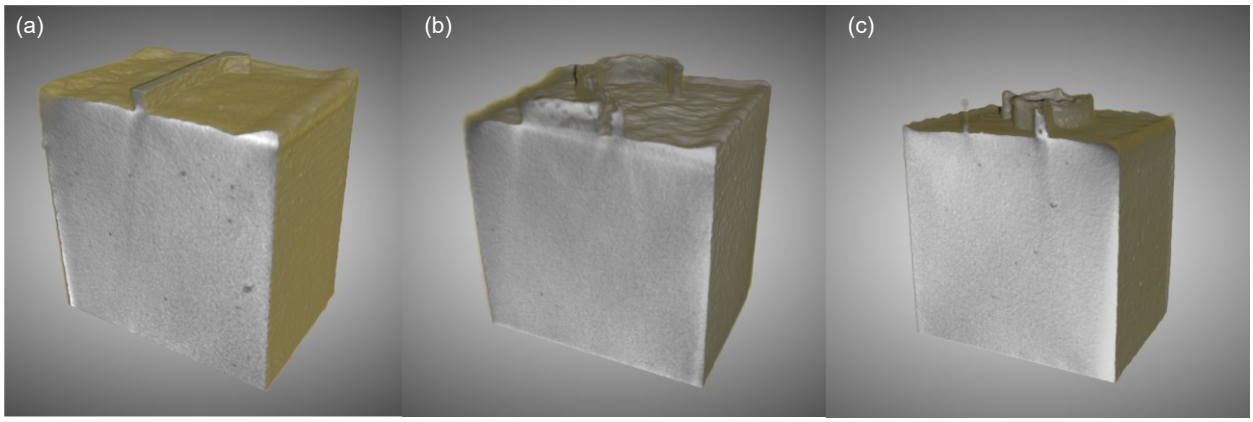

Figure 3.15: Cross-section CT images of optimized first row samples: (a) Sample 1; (b) Sample 2; (c) Sample (3).

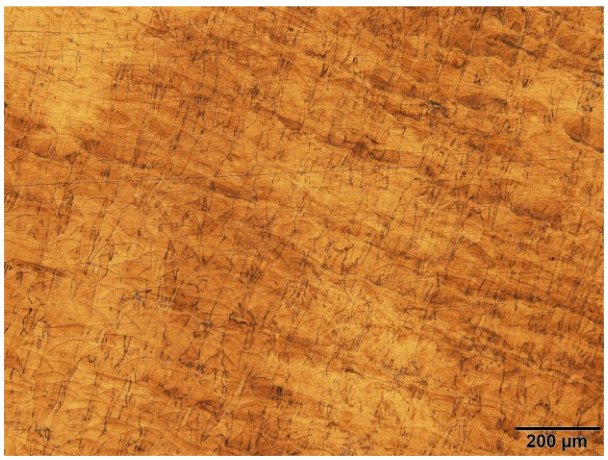

Figure 3.16: OM image of Set 2 optimized parameters.

3.3.3. Microstructure analysis

The XRD patterns of 2507 SDSS in different process parameters employed in the LPBF process are depicted in Figure 3.17. Duplex stainless steels consist of ferrite (bcc) and austenite (fcc) phases. The formation of the ferritic microstructure is followed by nucleation of the austenite phase at grain boundaries of the ferrite grains during the cooling cycle [88]. However, due to insufficient time as a result of the high cooling rate in the LPBF process, the phase transformation from ferrite to austenite is not favorable and this rapid cooling cycle in the LPBF process causes excessive ferritization. As can be seen, with the increase of energy density during the LPBF process, the diffraction intensities of the ferrite phase increase. Ferrite phase fraction increased from 73 % to 89.3 % and then 94.7 % with the increase of energy density from 22.22 J/mm3 to 97.69 J/mm3 (optimized set) and then 428.87 J/mm3, respectively. The reason for this change of ferrite fraction with the increase of energy density could be related to chemical composition change due to extremely high melt pool temperatures. It can be assumed that with increase of energy density, austenite stabilizer elements such as N during LPBF processing will be vaporized and lower the austenite content [100]. However, in order to get an optimal phase balance and restore the equilibrium duplex microstructure and mechanical properties of DSSs, post-processing heat treatment is recommended.

Kunz et al. [92] investigated the microstructure of LPBF produced 2507 SDSS parts and they found out that ferrite is the dominant phase and there is a limited amount of austenite in grain boundaries after the LPBF process. In order to increase the austenite fraction in duplex stainless steel, further solution annealing and heat treatment are recommended as Kunz et al achieved 43.3% after solution annealing. In another study on 2205 SDSS with chemical composition close to 2507

, Haghdadi et al. [101], reported austenite fraction of 2% mostly distributed in grain boundaries after LPBF process. Furthermore, they observed austenite promotion of 45% after heat treatment.

Figure 3.18 shows the microstructure evolution of the 2507 SDSS specimens at optimum energy density along the building direction. As Kunz et al [92] observed in their study, the square-like microstructure can be seen along the building direction which is due to the scanning strategy during the LPBF process. In another study, Nigon et al. [102] observed the same kind of square-like microstructure along the building direction of 2205 SDSS parts produced by LPBF.

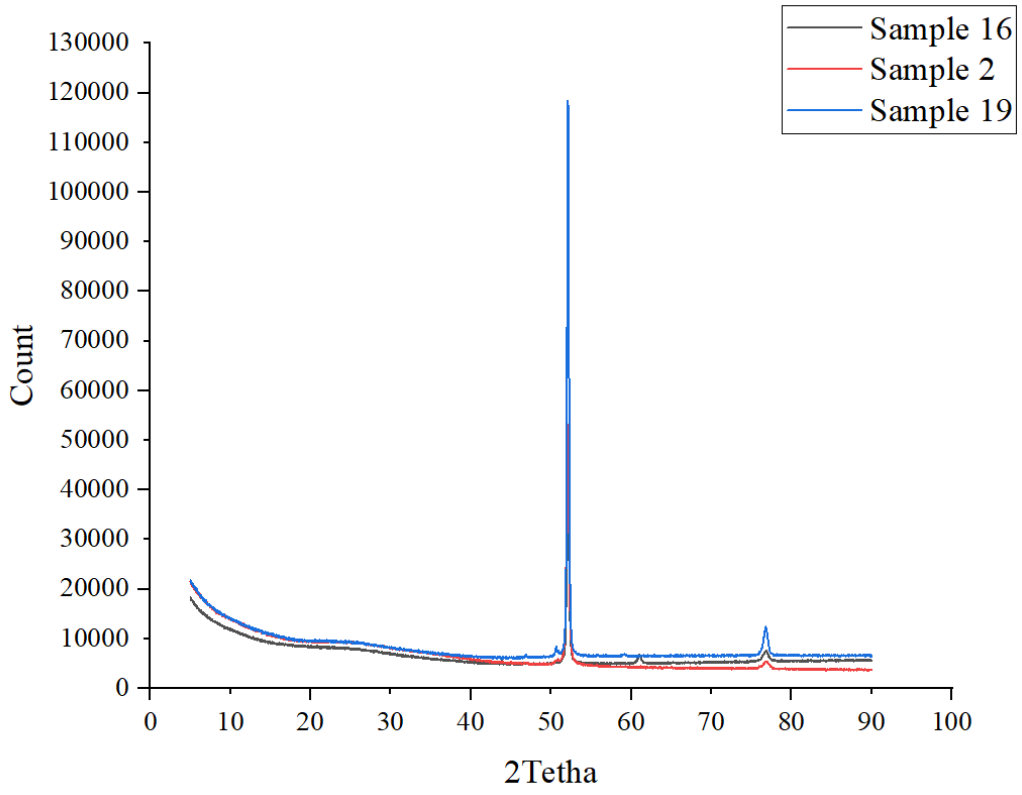

Figure 3.17: XRD patterns of 16, 2 (optimized), and 19 2507 SDSS samples.

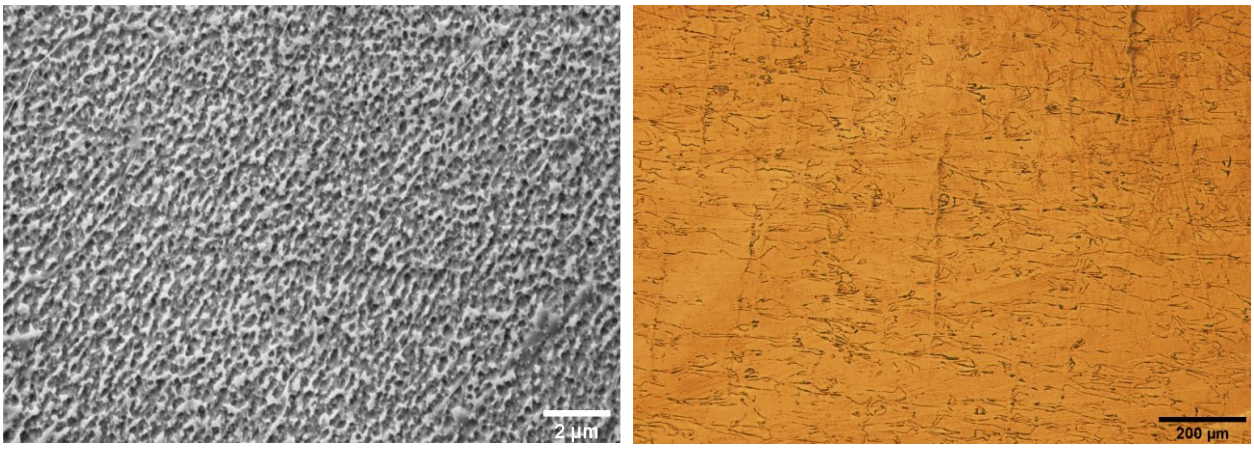

(a) (b)

Figure 3.18: Microstructure evolution of the 2507 SDSS specimens at optimum energy density; (a) SEM image, (b) OM image.

3.3.4. Tensile strength analysis

The printed tensile samples using the optimized printing parameters are shown in Figure 3.19, and the resulting yield strength, ultimate tensile strength (UTS), and elongation tensile properties are reported in Table 3.9. Sample 1 exhibited the highest yield and ultimate tensile strength of 1254.50 MPa and 1403.10 MPa, respectively, followed by sample 2 with a yield and ultimate tensile strength of 1131.70 MPa and 1366.70 MPa, respectively. However, sample 3 exhibited the lowest tensile properties with a yield and ultimate strength of 960.10 MPa and 1000.30 MPa, respectively. This behavior can be attributed as mentioned before to the position of each sample from the shielding gas. As shown in Figure 3.19, sample 3 is positioned farthest from the shielding gas, leading to an insufficient shielding gas flow rate which adversely affects the sample density (i.e., causing reduced mechanical results).

Table 3.10 compares the average 2507 SDSS tensile properties of the printed three samples to the DIN EN 10088-3 standard. The LPBF samples showed higher UTS of 1256.7 ± 181.9 MPa, and lower elongation of 10.7 ± 1.7 %. This behavior can be attributed to the higher ferritic microstructure of 89.3 %. Kunz et al. [92] reported a similar mechanical behavior of LPBF printed samples with UTS and elongation of 1031 MPa and 14 %, respectively. They attributed this

behavior to the resulting high ferritic microstructure of LPBF printed samples. Moreover, their heat-treated samples showed an increase in the austenite formation leading to a reduction in tensile strength and an increase in elongation (i.e., meeting the minimum requirements of the DIN EN 10088-3 standard).

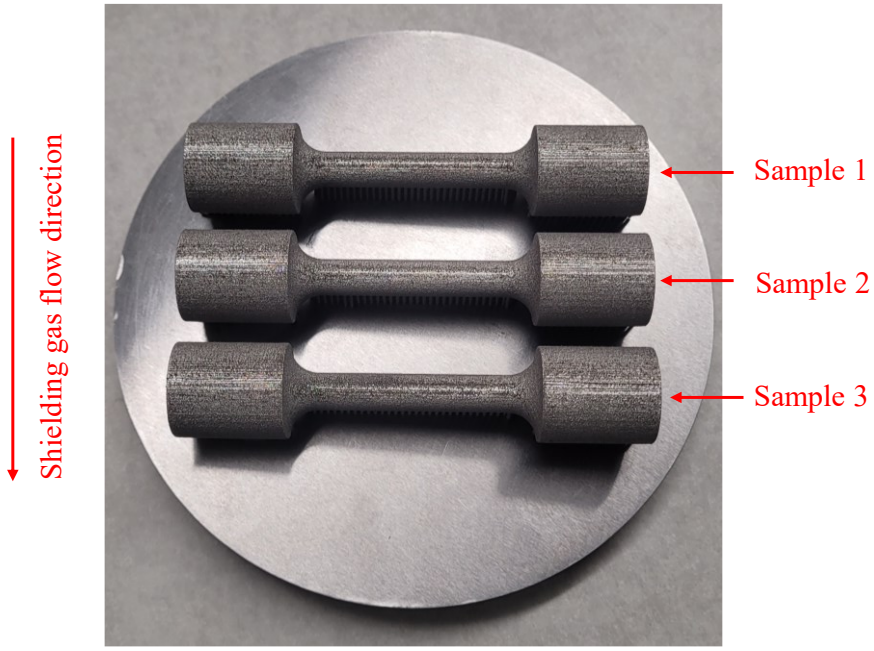

Figure 3.19: Printed tensile samples.

Table 3.9: Tensile test results of LPBF printed samples using the optimized parameters.

Sample	1	2	3
Yield strength (MPa)	1254.50	1131.70	960.10
Ultimate tensile strength (MPa)	1403.10	1366.70	1000.30
Elongation (%)	10.2	13.0	6.0

Table 3.10: 2507 SDSS tensile properties for LPBF samples and DIN EN 10088-3 standard.

Material	Condition	Number of samples	Yield strength (MPa)	UTS (MPa)	Elongation (%)
2507 SDSS	DIN EN 10088-3 standard	-	>500	700-900	>25
	LPBF	3	1115.4 ± 120.7	1256.7 ± 181.9	10.7 ± 1.7

Chapter 4: Conclusions and future work

4.1. Conclusions

The present work provides preliminary knowledge essential for heat transfer analysis of the proposed novel cellular-walled pipe heat sink system fabricated via LPBF process. The selection of the cellular structure type for enhanced heat transfer performance is investigated as well as providing a detailed analysis of its dimensional behaviors. Parameters such as wall thickness, surface area to volume ratio, pore size, and porosity were investigated at varying cellular structure cell sizes and porosities. A detailed design of experiment was conducted to explore the selected cellular structure dimensional trends, CAD to manufactured deviations, and the minimum wall thickness and pore size that can successfully be printed (i.e., LPBF printing limitations). The following is a summary of chapter (2) key findings:

- Previous studies showed that the Primitive TPMS lattice structure exhibited the highest heat transfer improvement compared to other lattice structures. As a result, it was selected for the proposed cellular-walled pipe heat sink system.

- Increasing the PTPMS lattice cell size from 2.9 to 10 mm showed an increase in the lattice wall thickness and pore size but a decrease in the SA:Vol ratio, which is attributed to the reduction in the number of cells within the lattice. However, increasing the lattice porosity from 45 to 90% resulted in a decrease in the lattice wall thickness with an increase in both the SA:Vol ratio and pore size. This behavior is attributed to the reduction in volume fraction with increasing the lattice porosity.

- The lattice shrinkage rate is observed to be increasing with increasing the lattice cell size and decreasing with increasing the lattice porosity. This is attributed to the behavior of the lattice

volume fraction in both cases. Increasing the lattice cell size from 2.9 to 10 mm showed an increase in the average shrinkage from 0.19 to 0.63 mm, respectively, whereas increasing the lattice porosity from 45 to 90% showed an average shrinkage decrease from 0.82 to 0.18 mm, respectively.

- The printed lattices at varying cell sizes and porosities showed lower manufactured wall thicknesses and higher SA:Vol ratios than CAD, which is attributed to shrinkage. Moreover, larger manufactured pore sizes and porosities than CAD were observed in both studies as well.

- Increasing the lattice cell size showed an increase in the CAD to manufactured deviations (i.e., lower dimensional accuracy) for the lattice wall thickness, pore size, and porosity. However, it is observed that the CAD to manufactured SA:Vol ratio deviation decreases with increasing the cell size.

- The design of significantly small lattice cell sizes should be avoided, as at small cell sizes, the average wall thickness becomes too thin (i.e., less than 0.175mm), causing high thermal gradients, which results in the formation of inner gaps that can poorly influence the lattice dimensional accuracy.

- Increasing the lattice porosity showed a decrease in the wall thickness CAD to manufactured deviation. Although other parameters: namely, SA:Vol ratio, pore size, and porosity seem to follow a similar trend, where increasing the lattice shows higher deviations at lower porosities; However, after a certain porosity threshold, the CAD to manufactured deviations are observed to be decreasing.

- The design of highly porous samples should be avoided as increasing the lattice porosity to extreme levels results in significantly fine lattice wall thicknesses (i.e., less than 0.175 mm) which causes the formation of gaps.

- The minimum lattice average wall thickness that can be successfully printed using the ORLAS Coherent 250W with the identified process parameters seen in Table (2.2) is 0.152 mm.

- The Min. pore size that can be successfully printed using the ORLAS Coherent 250W with the process parameters seen in Table (2.2) is found to be 0.317 mm.

Furthermore, a detailed printing parameter optimization study for 2507 super duplex stainless steel powder material is investigated. The LPBF printing parameters, namely: laser power, scan speed, and hatch distance, were optimized to print highly dense 2507 super duplex stainless steel samples. A detailed design of experiment using the RSM was conducted to investigate the various pore formation types along a wide energy density range (22.22 – 428.87 J/mm^3), analyze the influence of each process parameter and their interactions on the resulting porosity, and find an optimal parameter set capable of producing highly dense printed parts. Moreover, an investigation was conducted on the microstructure and tensile properties of printed samples using the selected optimized parameter set. The following is a summary of chapter (3) key findings:

- Being the most prevalent pore types associated with the printing process parameters; the lack-of-fusion, gas or metallurgical, and keyhole pore regimes were identified for 2507 SDSS at energy density ranges from 22.22 J/mm^3 to 68.24 J/mm^3, 68.24 J/mm^3 to 126.67 J/mm^3, and 126.67 J/mm^3 to 428.87 J/mm^3, respectively, with corresponding porosity ranges from 45.60% to 4.61%, 0.33% to 0.04%, and 0.15% to 1.56%.

- A sharp decrease in the lack-of-fusion porosity is observed at low energy densities, where increasing the energy density from 22.22 J/mm^3 to 68.24 J/mm^3 resulted in a porosity decrease from 45.60% to 0.33%. Conversely, a gradual increase in the keyhole porosity from 0.15% to 1.56% is observed at higher energy densities from 126.67 J/mm^3 to 428.87 J/mm^3, respectively.

- The sample's position from the shielding gas and coater sweep directions can influence the resulting sample porosity. Positioning the samples far from both directions can adversely influence the sample's density. However, the position influence seems to be more significant from the shielding gas than the coater sweep.

- The lack-of-fusion pores are relatively larger in size than the gas/metallurgical and keyhole pores, with mean ferret diameters of 0.26 mm, 0.05 mm, and 0.09 mm, respectively. Moreover, regarding the pore shape, the lack-of-fusion pores were observed to be irregular, with a mean aspect ratio of 0.33. Although the gas/metallurgical and keyhole pores showed roundish shapes; However, the gas/metallurgical pores were observed to be more spherical than keyhole pores, with respective mean aspect ratios of 0.65 and 0.57.

- A quadratic regression model between the input factors and the resulting porosity has been developed using the RSM. Model adequacy and accuracy checking has been conducted, which indicated that the model satisfies the residual normality and constant variance assumptions with an RMSE and MAE of 4.735% and 3.917%, respectively.

- The ANOVA analysis results showed that the linear terms of laser power, scan speed, and hatch distance were statistically significant, with P-values of 0.001, 0.001, and 0.004, respectively. However, the input factor non-linear effects were only observed to be significant

for the laser power with a P-value of 0.003. Moreover, the factor interaction influence on the porosity was only observed to be significant for speed and hatch factors, with a P-value of 0.011.

- The influence of each input parameter on the porosity was investigated using 3D surface and contour plots. Regarding power vs. speed plots, it was observed that low laser powers coupled with high scan speeds resulted in a high porosity profile. Although a reduction in the porosity is observed with increasing the laser power while decreasing the scan speed; however, extremely high laser powers coupled with low scan speeds were observed to increase the porosity due to the formation of keyhole pores at higher energy densities.

- The power vs. hatch plots showed that high porosities are present when having a combination of low laser power and high hatch distance. Moreover, it was observed that higher hatch distances should be avoided to prevent insufficient laser overlap leading to poor melting of the powder.

- The speed vs. hatch plots indicated that higher porosities are seen when having higher scan speeds coupled with high hatch distances. Although decreasing the scan speed and hatch distance results in a reduction in the porosity; However, setting extremely low scan speeds and hatching distances is observed to increase the porosity, which is attributed to the resulting high energy densities.

- The optimized parameters for laser power, scan speed, and hatch distance were 217.4 W, 1735.7 mm/s, and 51.3 μm, respectively, which were able to print samples with a relative density of 99.961%.

- Using the optimized parameter set, the as-built 2507 SDSS sample had a ferrite phase fraction of 89.3% with a yield and ultimate tensile strength of 1115.4 ± 120.7 MPa and 1256.7 ± 181.9 MPa, respectively.

4.2. Future work

The present work addresses the challenges that need to be investigated before any heat transfer analysis for the proposed cellular-walled pipe heat sink system. The Primitive TPMS lattice structure was selected for its enhanced heat transfer performance and a detailed assessment of its dimensional behavior is explored. Moreover, a detailed LPBF printing parameter optimization study for 2507 SDSS material is investigated to ensure the manufacturability of cellular-walled pipes using such material. Based on the thesis findings, the following research directions can be explored by future researchers:

- A detailed thermal conductivity analysis can be performed based on the same Primitive TPMS cell size and porosity studies seen in chapter (2). The Primitive TPMS lattice samples at varying cell sizes and porosities, using 17-4 PH stainless steel as the printing material, are already printed and available. However, printing these Primitive TPMS samples using 2507 SDSS are not yet available. Hence, the optimized printing parameters for 2507 SDSS seen in chapter (3) can be utilized to print these samples. Following the acquisition of Primitive TPMS samples manufactured with both stainless steel materials, the cell size and porosity variation influence on the lattice conductive heat transfer performance can be analyzed numerically and experimentally. The lattice dimensional data provided in chapter (2) can be utilized to explain the various thermal conductivity trends as well as provide explanations for different numerical and experimental conductive heat transfer performances at the same lattice cell size and porosity.

- Following the conductive heat transfer analysis, a detailed convective heat transfer analysis can be performed both numerically and experimentally. Using the already manufactured Primitive TPMS lattices, the cell size and porosity variation influence on the lattice convective heat transfer performance can be investigated. Once again, the dimensional data provided in chapter (2) can be utilized to explain the resulting convective heat transfer performance or any convective heat transfer deviations between numerical and experimental results at the same cell size and porosity.

- After establishing a solid understanding of conductive and convective heat transfer performance for the Primitive TPMS lattice structure, a lattice grading approach can be utilized. The grading approach can either vary the lattice porosity or the lattice cell size in a certain direction for one lattice sample. Performing a heat transfer analysis for such lattices and comparing their heat transfer performance with non-graded lattices could bring new possibilities to better enhance the lattice heat transfer performance.

- Finally, the Primitive TPMS walled pipe can be manufactured for enhanced heat transfer performance based on the heat transfer analysis results. Experimental heat transfer analysis can be conducted for both a solid pipe and our proposed cellular-walled pipe. The experimental analysis can be based on passing a hot fluid through the pipe and measuring the fluid temperature at the start and end of both pipes. The results should determine if our proposed cellular-walled pipe with a circulating coolant provides higher heat dissipation than the traditional solid pipe or not.

Bibliography

[1] W.E. Frazier, Metal Additive Manufacturing: A Review, J. Mater. Eng. Perform. 23 (2014) 1917–1928. https://doi.org/10.1007/s11665-014-0958-z.

[2] Y.-H. Lee, K.-J. Kang, A wire-woven cellular metal: Part-I, optimal design for applications as sandwich core, Mater. Des. 30 (2009) 4434–4443. https://doi.org/10.1016/j.matdes.2009.03.017.

[3] A.-J. Wang, R.S. Kumar, D.L. McDowell, Mechanical Behavior of Extruded Prismatic Cellular Metals, Mech. Adv. Mater. Struct. 12 (2005) 185–200. https://doi.org/10.1080/15376490590928534.

[4] V.S. Deshpande, N.A. Fleck, M.F. Ashby, Effective properties of the octet-truss lattice material, J. Mech. Phys. Solids. 49 (2001) 1747–1769. https://doi.org/10.1016/S0022-5096(01)00010-2.

[5] A. Carofalo, M. De Giorgi, A. Morabito, Geometric modelling of metallic foams, Eng. Comput. 30 (2013) 924–935. https://doi.org/10.1108/EC-06-2011-0070.

[6] F.J. Alamos, J. Schiltz, K. Kozlovsky, R. Attardo, C. Tomonto, T. Pelletiers, S.R. Schmid, Effect of powder reuse on mechanical properties of Ti-6Al-4V produced through selective laser melting, Int. J. Refract. Met. Hard Mater. 91 (2020) 105273. https://doi.org/10.1016/j.ijrmhm.2020.105273.

[7] F.J. Alamos, J. Schiltz, R. Attardo, B. Aboud Gatrell, C. Tomonto, J. Budzinski, J. McGuffin-Cawley, T. Pelletiers, S.R. Schmid, Effect of powder reuse on orthopedic metals produced through selective laser sintering, Manuf. Lett. 31 (2022) 40–44. https://doi.org/10.1016/j.mfglet.2021.06.002.

[8] L. Cordova, T. Bor, M. de Smit, S. Carmignato, M. Campos, T. Tinga, Effects of powder reuse on the microstructure and mechanical behaviour of Al–Mg–Sc–Zr alloy processed by laser powder bed fusion (LPBF), Addit. Manuf. 36 (2020) 101625. https://doi.org/10.1016/j.addma.2020.101625.

[9] P. Colombo, H.P. Degischer, Highly porous metals and ceramics, Mater. Sci. Technol. 26 (2010) 1145–1158. https://doi.org/10.1179/026708310X12756557336157.

[10] M.F. Ashby, A.G. Evans, N.A. Fleck, L.J. Gibson, J.W. Hutchinson, H.N.G. Wadley, Metal Foams: A Design Guide, 2000.

[11] K.-J. Kang, A wire-woven cellular metal of ultrahigh strength, Acta Mater. 57 (2009) 1865–1874. https://doi.org/10.1016/j.actamat.2008.12.027.

[12] P. Colombo, In Praise of Pores, Science (80-.). 322 (2008) 381–383. https://doi.org/10.1126/science.1162962.

[13] D. Ruan, G. Lu, F.. Chen, E. Siores, Compressive behaviour of aluminium foams at low and medium strain rates, Compos. Struct. 57 (2002) 331–336. https://doi.org/10.1016/S0263-8223(02)00100-9.

[14] A.G. Leach, The thermal conductivity of foams. I. Models for heat conduction, J. Phys. D. Appl. Phys. 26 (1993) 733–739. https://doi.org/10.1088/0022-3727/26/5/003.

[15] A. Thompson, I. Maskery, R.K. Leach, X-ray computed tomography for additive manufacturing: a review, Meas. Sci. Technol. 27 (2016) 072001. https://doi.org/10.1088/0957-0233/27/7/072001.

[16] J.-P. Kruth, G. Levy, F. Klocke, T.H.C. Childs, Consolidation phenomena in laser and powder-bed based layered manufacturing, CIRP Ann. 56 (2007) 730–759. https://doi.org/10.1016/j.cirp.2007.10.004.

[17] B. Zhang, H. Liao, C. Coddet, Effects of processing parameters on properties of selective laser melting Mg–9%Al powder mixture, Mater. Des. 34 (2012) 753–758. https://doi.org/10.1016/j.matdes.2011.06.061.

[18] D. Wang, Y. Yang, Z. Yi, X. Su, Research on the fabricating quality optimization of the overhanging surface in SLM process, Int. J. Adv. Manuf. Technol. 65 (2013) 1471–1484.

https://doi.org/10.1007/s00170-012-4271-4.

[19] X. Su, Y. Yang, D. Xiao, Z. Luo, An investigation into direct fabrication of fine-structured components by selective laser melting, Int. J. Adv. Manuf. Technol. 64 (2013) 1231–1238. https://doi.org/10.1007/s00170-012-4081-8.

[20] P. Muller, P. Mognol, J.-Y. Hascoet, Modeling and control of a direct laser powder deposition process for Functionally Graded Materials (FGM) parts manufacturing, J. Mater. Process. Technol. 213 (2013) 685–692. https://doi.org/10.1016/j.jmatprotec.2012.11.020.

[21] T.J. Lu, F. Xu, T. Wen, Thermo-Fluid Behaviour of Periodic Cellular Metals, Springer Berlin Heidelberg, Berlin, Heidelberg, 2013. https://doi.org/10.1007/978-3-642-33524-2.

[22] M. Mazur, M. Leary, M. McMillan, S. Sun, D. Shidid, M. Brandt, Mechanical properties of Ti6Al4V and AlSi12Mg lattice structures manufactured by Selective Laser Melting (SLM), in: Laser Addit. Manuf., Elsevier, 2017: pp. 119–161. https://doi.org/10.1016/B978-0-08-100433-3.00005-1.

[23] O. Rahman, K.Z. Uddin, J. Muthulingam, G. Youssef, C. Shen, B. Koohbor, Density-Graded Cellular Solids: Mechanics, Fabrication, and Applications, Adv. Eng. Mater. 24 (2022) 2100646. https://doi.org/10.1002/adem.202100646.

[24] C. Pan, Y. Han, J. Lu, Design and Optimization of Lattice Structures: A Review, Appl. Sci. 10 (2020) 6374. https://doi.org/10.3390/app10186374.

[25] N. Baobaid, M.I. Ali, K.A. Khan, R.K. Abu Al-Rub, Fluid flow and heat transfer of porous TPMS architected heat sinks in free convection environment, Case Stud. Therm. Eng. 33 (2022) 101944. https://doi.org/10.1016/j.csite.2022.101944.

[26] A.G. Evans, J.W. Hutchinson, N.A. Fleck, M.F. Ashby, H.N.G. Wadley, The topological design of multifunctional cellular metals, Prog. Mater. Sci. 46 (2001) 309–327.

https://doi.org/10.1016/S0079-6425(00)00016-5.

[27] O. Cansizoglu, O. Harrysson, D. Cormier, H. West, T. Mahale, Properties of Ti–6Al–4V non-stochastic lattice structures fabricated via electron beam melting, Mater. Sci. Eng. A. 492 (2008) 468–474. https://doi.org/10.1016/j.msea.2008.04.002.

[28] S. Gu, T.J. Lu, A.G. Evans, On the design of two-dimensional cellular metals for combined heat dissipation and structural load capacity, Int. J. Heat Mass Transf. 44 (2001) 2163–2175. https://doi.org/10.1016/S0017-9310(00)00234-9.

[29] M. Wong, S. Tsopanos, C.J. Sutcliffe, I. Owen, Selective laser melting of heat transfer devices, Rapid Prototyp. J. 13 (2007) 291–297. https://doi.org/10.1108/13552540710824797.

[30] M. Wong, I. Owen, C.J. Sutcliffe, A. Puri, Convective heat transfer and pressure losses across novel heat sinks fabricated by Selective Laser Melting, Int. J. Heat Mass Transf. 52 (2009) 281–288. https://doi.org/10.1016/j.ijheatmasstransfer.2008.06.002.

[31] S. Catchpole-Smith, R.R.J. Sélo, A.W. Davis, I.A. Ashcroft, C.J. Tuck, A. Clare, Thermal conductivity of TPMS lattice structures manufactured via laser powder bed fusion, Addit. Manuf. 30 (2019) 100846. https://doi.org/10.1016/j.addma.2019.100846.

[32] O. Al-Ketan, R. Rowshan, R.K. Abu Al-Rub, Topology-mechanical property relationship of 3D printed strut, skeletal, and sheet based periodic metallic cellular materials, Addit. Manuf. 19 (2018) 167–183. https://doi.org/10.1016/j.addma.2017.12.006.

[33] G. Savio, S. Rosso, R. Meneghello, G. Concheri, Geometric Modeling of Cellular Materials for Additive Manufacturing in Biomedical Field: A Review, Appl. Bionics Biomech. 2018 (2018) 1–14. https://doi.org/10.1155/2018/1654782.

[34] D.J. Yoo, Porous scaffold design using the distance field and triply periodic minimal surface models, Biomaterials. 32 (2011) 7741–7754. https://doi.org/10.1016/j.biomaterials.2011.07.019.

[35] Z.A. Qureshi, S. Addin Burhan Al-Omari, E. Elnajjar, O. Al-Ketan, R.A. Al-Rub, On the effect of porosity and functional grading of 3D printable triply periodic minimal surface (TPMS) based architected lattices embedded with a phase change material, Int. J. Heat Mass Transf. 183 (2022) 122111. https://doi.org/10.1016/j.ijheatmasstransfer.2021.122111.

[36] Z.A. Qureshi, S.A.B. Al Omari, E. Elnajjar, F. Mahmoud, O. Al-Ketan, R.A. Al-Rub, Thermal characterization of 3D-Printed lattices based on triply periodic minimal surfaces embedded with organic phase change material, Case Stud. Therm. Eng. 27 (2021) 101315. https://doi.org/10.1016/j.csite.2021.101315.

[37] C. Yan, L. Hao, A. Hussein, P. Young, D. Raymont, Advanced lightweight 316L stainless steel cellular lattice structures fabricated via selective laser melting, Mater. Des. 55 (2014) 533–541. https://doi.org/10.1016/j.matdes.2013.10.027.

[38] S.L. Sing, W.Y. Yeong, F.E. Wiria, B.Y. Tay, Characterization of Titanium Lattice Structures Fabricated by Selective Laser Melting Using an Adapted Compressive Test Method, Exp. Mech. 56 (2016) 735–748. https://doi.org/10.1007/s11340-015-0117-y.

[39] J. Weidmann, A. Großmann, C. Mittelstedt, Laser powder bed fusion manufacturing of aluminum honeycomb structures: Theory and testing, Int. J. Mech. Sci. 180 (2020) 105639. https://doi.org/10.1016/j.ijmecsci.2020.105639.

[40] A. Großmann, J. Felger, T. Frölich, J. Gosmann, C. Mittelstedt, Melt pool controlled laser powder bed fusion for customised low-density lattice structures, Mater. Des. 181 (2019) 108054. https://doi.org/10.1016/j.matdes.2019.108054.

[41] W. van Grunsven, E. Hernandez-Nava, G. Reilly, R. Goodall, Fabrication and Mechanical Characterisation of Titanium Lattices with Graded Porosity, Metals (Basel). 4 (2014) 401–409. https://doi.org/10.3390/met4030401.

[42] C. López-García, E. García-López, H.R. Siller, J.A. Sandoval-Robles, C.A. Rodriguez, A dimensional assessment of small features and lattice structures manufactured by laser powder bed fusion, Prog. Addit. Manuf. 7 (2022) 751–763. https://doi.org/10.1007/s40964-022-00263-0.

[43] S. Cheruvathur, E.A. Lass, C.E. Campbell, Additive Manufacturing of 17-4 PH Stainless Steel: Post-processing Heat Treatment to Achieve Uniform Reproducible Microstructure, JOM. 68 (2016) 930–942. https://doi.org/10.1007/s11837-015-1754-4.

[44] W.J. Sames, F.A. List, S. Pannala, R.R. Dehoff, S.S. Babu, The metallurgy and processing science of metal additive manufacturing, Int. Mater. Rev. 61 (2016) 315–360. https://doi.org/10.1080/09506608.2015.1116649.

[45] J.H. Tan, W.L.E. Wong, K.W. Dalgarno, An overview of powder granulometry on feedstock and part performance in the selective laser melting process, Addit. Manuf. 18 (2017) 228–255. https://doi.org/10.1016/j.addma.2017.10.011.

[46] N. Kladovasilakis, P. Charalampous, I. Kostavelis, D. Tzetzis, D. Tzovaras, Impact of metal additive manufacturing parameters on the powder bed fusion and direct energy deposition processes: a comprehensive review, Prog. Addit. Manuf. 6 (2021) 349–365. https://doi.org/10.1007/s40964-021-00180-8.

[47] C. Yan, L. Hao, L. Yang, A.Y. Hussein, P.G. Young, Z. Li, Y. Li, Metal alloys uniform TPMS structures, in: Triply Period. Minimal Surf. Lattices Addit. Manuf. by Sel. Laser Melting, Elsevier, 2021: pp. 39–130. https://doi.org/10.1016/B978-0-12-824438-8.00003-0.

[48] H. Zaharin, A. Abdul Rani, F. Azam, T. Ginta, N. Sallih, A. Ahmad, N. Yunus, T. Zulkifli, Effect of Unit Cell Type and Pore Size on Porosity and Mechanical Behavior of Additively Manufactured Ti6Al4V Scaffolds, Materials (Basel). 11 (2018) 2402. https://doi.org/10.3390/ma11122402.

[49] A. du Plessis, I. Yadroitsev, I. Yadroitsava, S.G. Le Roux, X-Ray Microcomputed Tomography in Additive Manufacturing: A Review of the Current Technology and Applications, 3D Print. Addit. Manuf. 5 (2018) 227–247. https://doi.org/10.1089/3dp.2018.0060.

[50] H.-J. Yang, P.-J. Hwang, S.-H. Lee, A study on shrinkage compensation of the SLS process by using the Taguchi method, Int. J. Mach. Tools Manuf. 42 (2002) 1203–1212. https://doi.org/10.1016/S0890-6955(02)00070-6.

[51] N. Raghunath, P.M. Pandey, Improving accuracy through shrinkage modelling by using Taguchi method in selective laser sintering, Int. J. Mach. Tools Manuf. 47 (2007) 985–995. https://doi.org/10.1016/j.ijmachtools.2006.07.001.

[52] K. Senthilkumaran, P.M. Pandey, P.V.M. Rao, Influence of building strategies on the accuracy of parts in selective laser sintering, Mater. Des. 30 (2009) 2946–2954. https://doi.org/10.1016/j.matdes.2009.01.009.

[53] Y. Liu, Y. Yang, D. Wang, Investigation into the shrinkage in Z-direction of components manufactured by selective laser melting (SLM), Int. J. Adv. Manuf. Technol. 90 (2017) 2913–2923. https://doi.org/10.1007/s00170-016-9596-y.

[54] V. Chahal, R.M. Taylor, A review of geometric sensitivities in laser metal 3D printing, Virtual Phys. Prototyp. 15 (2020) 227–241. https://doi.org/10.1080/17452759.2019.1709255.

[55] M.X. Gan, C.H. Wong, Practical support structures for selective laser melting, J. Mater. Process. Technol. 238 (2016) 474–484. https://doi.org/10.1016/j.jmatprotec.2016.08.006.

[56] C. Yan, L. Hao, L. Yang, A.Y. Hussein, P.G. Young, Z. Li, Y. Li, Design of TPMS structures, in: Triply Period. Minimal Surf. Lattices Addit. Manuf. by Sel. Laser Melting, Elsevier, 2021: pp. 27–38. https://doi.org/10.1016/B978-0-12-824438-8.00002-9.

[57] M. Benedetti, A. du Plessis, R.O. Ritchie, M. Dallago, S.M.J. Razavi, F. Berto, Architected

cellular materials: A review on their mechanical properties towards fatigue-tolerant design and fabrication, Mater. Sci. Eng. R Reports. 144 (2021). https://doi.org/10.1016/J.MSER.2021.100606.

[58] T. DebRoy, H.L. Wei, J.S. Zuback, T. Mukherjee, J.W. Elmer, J.O. Milewski, A.M. Beese, A. Wilson-Heid, A. De, W. Zhang, Additive manufacturing of metallic components – Process, structure and properties, Prog. Mater. Sci. 92 (2018) 112–224. https://doi.org/10.1016/j.pmatsci.2017.10.001.

[59] D.D. Gu, W. Meiners, K. Wissenbach, R. Poprawe, Laser additive manufacturing of metallic components: materials, processes and mechanisms, Int. Mater. Rev. 57 (2012) 133–164. https://doi.org/10.1179/1743280411Y.0000000014.

[60] D. Herzog, V. Seyda, E. Wycisk, C. Emmelmann, Additive manufacturing of metals, Acta Mater. 117 (2016) 371–392. https://doi.org/10.1016/j.actamat.2016.07.019.

[61] D. Bourell, J.P. Kruth, M. Leu, G. Levy, D. Rosen, A.M. Beese, A. Clare, Materials for additive manufacturing, CIRP Ann. 66 (2017) 659–681. https://doi.org/10.1016/j.cirp.2017.05.009.

[62] M. Schmidt, M. Merklein, D. Bourell, D. Dimitrov, T. Hausotte, K. Wegener, L. Overmeyer, F. Vollertsen, G.N. Levy, Laser based additive manufacturing in industry and academia, CIRP Ann. 66 (2017) 561–583. https://doi.org/10.1016/j.cirp.2017.05.011.

[63] S. Afazov, W.A.D. Denmark, B. Lazaro Toralles, A. Holloway, A. Yaghi, Distortion prediction and compensation in selective laser melting, Addit. Manuf. 17 (2017) 15–22. https://doi.org/10.1016/j.addma.2017.07.005.

[64] C.Y. Yap, C.K. Chua, Z.L. Dong, Z.H. Liu, D.Q. Zhang, L.E. Loh, S.L. Sing, Review of selective laser melting: Materials and applications, Appl. Phys. Rev. 2 (2015) 041101. https://doi.org/10.1063/1.4935926.

[65] M. Taheri Andani, R. Dehghani, M.R. Karamooz-Ravari, R. Mirzaeifar, J. Ni, A study on the

effect of energy input on spatter particles creation during selective laser melting process, Addit. Manuf. 20 (2018) 33–43. https://doi.org/10.1016/j.addma.2017.12.009.

[66] J.A. Slotwinski, E.J. Garboczi, P.E. Stutzman, C.F. Ferraris, S.S. Watson, M.A. Peltz, Characterization of Metal Powders Used for Additive Manufacturing, J. Res. Natl. Inst. Stand. Technol. 119 (2014) 460. https://doi.org/10.6028/jres.119.018.

[67] S. Qu, J. Ding, X. Song, Achieving Triply Periodic Minimal Surface Thin-Walled Structures by Micro Laser Powder Bed Fusion Process, Micromachines. 12 (2021) 705. https://doi.org/10.3390/mi12060705.

[68] K. Kempen, Expanding the materials palette for Selective Laser Melting of metals, 2015. https://lirias.kuleuven.be/1673720?limo=0 (accessed August 10, 2022).

[69] B. Zhang, Y. Li, Q. Bai, Defect Formation Mechanisms in Selective Laser Melting: A Review, Chinese J. Mech. Eng. 30 (2017) 515–527. https://doi.org/10.1007/s10033-017-0121-5.

[70] H. Gong, K. Rafi, H. Gu, T. Starr, B. Stucker, Analysis of defect generation in Ti–6Al–4V parts made using powder bed fusion additive manufacturing processes, Addit. Manuf. 1–4 (2014) 87–98. https://doi.org/10.1016/j.addma.2014.08.002.

[71] J. Liu, P. Wen, Metal vaporization and its influence during laser powder bed fusion process, Mater. Des. 215 (2022) 110505. https://doi.org/10.1016/j.matdes.2022.110505.

[72] M. Tang, P.C. Pistorius, J.L. Beuth, Prediction of lack-of-fusion porosity for powder bed fusion, Addit. Manuf. 14 (2017) 39–48. https://doi.org/10.1016/j.addma.2016.12.001.

[73] R. Cunningham, S.P. Narra, T. Ozturk, J. Beuth, A.D. Rollett, Evaluating the Effect of Processing Parameters on Porosity in Electron Beam Melted Ti-6Al-4V via Synchrotron X-ray Microtomography, JOM. 68 (2016) 765–771. https://doi.org/10.1007/s11837-015-1802-0.

[74] R. Cunningham, S.P. Narra, C. Montgomery, J. Beuth, A.D. Rollett, Synchrotron-Based X-ray

Microtomography Characterization of the Effect of Processing Variables on Porosity Formation in Laser Power-Bed Additive Manufacturing of Ti-6Al-4V, JOM. 69 (2017) 479–484. https://doi.org/10.1007/s11837-016-2234-1.

[75] C. Zhao, K. Fezzaa, R.W. Cunningham, H. Wen, F. De Carlo, L. Chen, A.D. Rollett, T. Sun, Real-time monitoring of laser powder bed fusion process using high-speed X-ray imaging and diffraction, Sci. Reports 2017 71. 7 (2017) 1–11. https://doi.org/10.1038/s41598-017-03761-2.

[76] C.L.A. Leung, S. Marussi, R.C. Atwood, M. Towrie, P.J. Withers, P.D. Lee, In situ X-ray imaging of defect and molten pool dynamics in laser additive manufacturing, Nat. Commun. 9 (2018) 1355. https://doi.org/10.1038/s41467-018-03734-7.

[77] R. Cunningham, C. Zhao, N. Parab, C. Kantzos, J. Pauza, K. Fezzaa, T. Sun, A.D. Rollett, Keyhole threshold and morphology in laser melting revealed by ultrahigh-speed x-ray imaging, Science (80-.). 363 (2019) 849–852. https://doi.org/10.1126/science.aav4687.

[78] A. du Plessis, Effects of process parameters on porosity in laser powder bed fusion revealed by X-ray tomography, Addit. Manuf. 30 (2019) 100871. https://doi.org/10.1016/j.addma.2019.100871.

[79] T. Becker, Selective Laser Melting Produced Ti-6Al-4V: Post-Process Heat Treatments to Achieve Superior Tensile Properties, Materials (Basel). 11 (2018) 146. https://doi.org/10.3390/ma11010146.

[80] J. Suryawanshi, K.G. Prashanth, S. Scudino, J. Eckert, O. Prakash, U. Ramamurty, Simultaneous enhancements of strength and toughness in an Al-12Si alloy synthesized using selective laser melting, Acta Mater. 115 (2016) 285–294. https://doi.org/10.1016/j.actamat.2016.06.009.

[81] A. Iturrioz, E. Gil, M.M. Petite, F. Garciandia, A.M. Mancisidor, M. San Sebastian, Selective laser melting of AlSi10Mg alloy: influence of heat treatment condition on mechanical properties and microstructure, Weld. World. 62 (2018) 885–892. https://doi.org/10.1007/s40194-018-0592-8.

[82] A.B. Spierings, K. Dawson, K. Kern, F. Palm, K. Wegener, SLM-processed Sc- and Zr- modified Al-Mg alloy: Mechanical properties and microstructural effects of heat treatment, Mater. Sci. Eng. A. 701 (2017) 264–273. https://doi.org/10.1016/j.msea.2017.06.089.

[83] A. Takaichi, Suyalatu, T. Nakamoto, N. Joko, N. Nomura, Y. Tsutsumi, S. Migita, H. Doi, S. Kurosu, A. Chiba, N. Wakabayashi, Y. Igarashi, T. Hanawa, Microstructures and mechanical properties of Co–29Cr–6Mo alloy fabricated by selective laser melting process for dental applications, J. Mech. Behav. Biomed. Mater. 21 (2013) 67–76. https://doi.org/10.1016/j.jmbbm.2013.01.021.

[84] D. Tomus, P.A. Rometsch, M. Heilmaier, X. Wu, Effect of minor alloying elements on crack-formation characteristics of Hastelloy-X manufactured by selective laser melting, Addit. Manuf. 16 (2017) 65–72. https://doi.org/10.1016/j.addma.2017.05.006.

[85] D. Deng, R.L. Peng, H. Brodin, J. Moverare, Microstructure and mechanical properties of Inconel 718 produced by selective laser melting: Sample orientation dependence and effects of post heat treatments, Mater. Sci. Eng. A. 713 (2018) 294–306. https://doi.org/10.1016/j.msea.2017.12.043.

[86] H. Choo, K.-L. Sham, J. Bohling, A. Ngo, X. Xiao, Y. Ren, P.J. Depond, M.J. Matthews, E. Garlea, Effect of laser power on defect, texture, and microstructure of a laser powder bed fusion processed 316L stainless steel, Mater. Des. 164 (2019) 107534. https://doi.org/10.1016/j.matdes.2018.12.006.

[87] K.-T. Yang, M.-K. Kim, D. Kim, J. Suhr, Investigation of laser powder bed fusion manufacturing and post-processing for surface quality of as-built 17-4PH stainless steel, Surf. Coatings Technol. 422 (2021) 127492. https://doi.org/10.1016/j.surfcoat.2021.127492.

[88] Z. Zhang, H. Zhang, J. Hu, X. Qi, Y. Bian, A. Shen, P. Xu, Y. Zhao, Microstructure evolution and mechanical properties of briefly heat-treated SAF 2507 super duplex stainless steel welds, Constr. Build. Mater. 168 (2018) 338–345. https://doi.org/10.1016/j.conbuildmat.2018.02.143.

[89] M. Martins, L.C. Casteletti, Heat treatment temperature influence on ASTM A890 GR 6A super duplex stainless steel microstructure, Mater. Charact. 55 (2005) 225–233. https://doi.org/10.1016/j.matchar.2005.05.008.

[90] K. Davidson, S. Singamneni, Selective Laser Melting of Duplex Stainless Steel Powders: An Investigation, Mater. Manuf. Process. 31 (2016) 1543–1555. https://doi.org/10.1080/10426914.2015.1090605.

[91] K. Saeidi, L. Kevetkova, F. Lofaj, Z. Shen, Novel ferritic stainless steel formed by laser melting from duplex stainless steel powder with advanced mechanical properties and high ductility, Mater. Sci. Eng. A. 665 (2016) 59–65. https://doi.org/10.1016/j.msea.2016.04.027.

[92] J. Kunz, A. Boontanom, S. Herzog, P. Suwanpinij, A. Kaletsch, C. Broeckmann, Influence of hot isostatic pressing post-treatment on the microstructure and mechanical behavior of standard and super duplex stainless steel produced by laser powder bed fusion, Mater. Sci. Eng. A. 794 (2020) 139806. https://doi.org/10.1016/j.msea.2020.139806.

[93] G. Wang, L. Huang, Z. Liu, Z. Qin, W. He, F. Liu, C. Chen, Y. Nie, Process optimization and mechanical properties of oxide dispersion strengthened nickel-based superalloy by selective laser melting, Mater. Des. 188 (2020) 108418. https://doi.org/10.1016/j.matdes.2019.108418.

[94] M. Terner, T. Ricordel, J.-H. Cho, J.-S. Lee, The Response Surface Methodology for Optimizing the Process Parameters of Selective Laser Melting, J. Weld. Join. 37 (2019) 27–39. https://doi.org/10.5781/JWJ.2019.37.1.4.

[95] Y. Deng, Z. Mao, N. Yang, X. Niu, X. Lu, Collaborative Optimization of Density and Surface Roughness of 316L Stainless Steel in Selective Laser Melting, Materials (Basel). 13 (2020) 1601. https://doi.org/10.3390/ma13071601.

[96] J.H. Tan, W.L.E. Wong, K.W. Dalgarno, An overview of powder granulometry on feedstock and

part performance in the selective laser melting process, Addit. Manuf. 18 (2017) 228–255. https://doi.org/10.1016/j.addma.2017.10.011.

[97] D.C. Montgomery, Design and Analysis of Experiments Eighth Edition. Arizona State University, 2013.

[98] H.C. Hyer, C.M. Petrie, Effect of powder layer thickness on the microstructural development of additively manufactured SS316, J. Manuf. Process. 76 (2022) 666–674. https://doi.org/10.1016/j.jmapro.2022.02.047.

[99] B. Ferrar, L. Mullen, E. Jones, R. Stamp, C.J. Sutcliffe, Gas flow effects on selective laser melting (SLM) manufacturing performance, J. Mater. Process. Technol. 212 (2012) 355–364. https://doi.org/10.1016/j.jmatprotec.2011.09.020.

[100] V.A. Hosseini, S. Wessman, K. Hurtig, L. Karlsson, Nitrogen loss and effects on microstructure in multipass TIG welding of a super duplex stainless steel, Mater. Des. 98 (2016) 88–97. https://doi.org/10.1016/j.matdes.2016.03.011.

[101] N. Haghdadi, M. Laleh, H. Chen, Z. Chen, C. Ledermueller, X. Liao, S. Ringer, S. Primig, On the pitting corrosion of 2205 duplex stainless steel produced by laser powder bed fusion additive manufacturing in the as-built and post-processed conditions, Mater. Des. 212 (2021) 110260. https://doi.org/10.1016/j.matdes.2021.110260.

[102] G.N. Nigon, O. Burkan Isgor, S. Pasebani, The effect of annealing on the selective laser melting of 2205 duplex stainless steel: Microstructure, grain orientation, and manufacturing challenges, Opt. Laser Technol. 134 (2021) 106643. https://doi.org/10.1016/j.optlastec.2020.106643.